Photovoltaic Properties and Size-pH Phase Stability of Iron Disulfide from Density-Functional Theory

by

Ruoshi Sun

B.S., Materials Science and Engineering, University of Illinois at Urbana-Champaign (2008)
B.S., Mathematics, University of Illinois at Urbana-Champaign (2008)

Submitted to the Department of Materials Science and Engineering
in partial fulfillment of the requirements for the degree of

Doctor of Philosophy in Materials Science and Engineering

at the

MASSACHUSETTS INSTITUTE OF TECHNOLOGY

September 2013

Author .....
Department of Materials Science and Engineering
July 26, 2013

Certified by .....
Gerbrand Ceder
R. P. Simmons Professor of Materials Science and Engineering
Thesis Supervisor

Accepted by .....
Gerbrand Ceder
Chairman, Department Committee on Graduate Students

Photovoltaic Properties and Size-pH Phase Stability of Iron Disulfide from Density-Functional Theory

by

Ruoshi Sun

Submitted to the Department of Materials Science and Engineering
on July 26, 2013, in partial fulfillment of the
requirements for the degree of
Doctor of Philosophy in Materials Science and Engineering

Abstract

Despite its exceptional optical absorptivity, suitable band gap, and earth abundance, the low open-circuit voltage of pyrite FeS_2 has remained the biggest challenge preventing its use in photovoltaic devices. Two widely-accepted causes are: (i) Fermi level pinning caused by intrinsic surface states that appear as gap states; (ii) presence of the polymorph marcasite. Based on density-functional theory (DFT) calculations, (i) the intrinsic (100) surface states are not gap states but located at the conduction band edge; (ii) epitaxial growth of marcasite on pyrite is thermodynamically favorable, but its band gap (from Kohn-Sham and Δ-sol method) is not less than pyrite. It is unlikely that the photovoltaic performance of pyrite is undermined by intrinsic surface states or marcasite.

The stoichiometry and the ubiquitous observation of unintentional p-type conductivity of pyrite thin films are investigated via DFT defect computations. Native defects occur in low concentrations due to high formation energies, implying that pyrite is intrinsically stoichiometric. The p-type conductivity can be caused by O_S defects under oxidizing conditions.

Band gap engineering of pyrite is studied by alloying with non-rare-earth isovalent elements via DFT computations. We identify six MS_2 candidates that have larger band gaps than pyrite. Band gap enhancement of pyrite is observed only in the Ru and Os alloyed systems, but their incorporation into pyrite may be severely limited. All other candidate alloys exhibit large gap bowing effects due to size and/or electronegativity mismatch.

The effects of particle size and pH on the relative phase stability of pyrite and marcasite polymorphs are explored. The size effect is incorporated through volume scaling of Wulff shapes. The pH effect is modeled by generalized, charged surface energies as a result of ion adsorption from the aqueous environment. Based on joint density-functional theory calculations, pyrite is unstable in highly acidic conditions due to a negative H^+-adsorbed (110) surface energy, but stabilized for pH $\gtrsim$ 2. Directions for future work are briefly discussed.

Thesis Supervisor: Gerbrand Ceder
Title: R. P. Simmons Professor of Materials Science and Engineering

To my wife and our parents

Acknowledgments

I walked around this complex plane
And gazed along the forbidden lane
The poles of singularities
The residues of pain
Yet integrating into a love
That forever shall remain

April 16, 2013
In memory of an incident that occurred 2 km away while I was writing this thesis.

* * *

The work presented in this thesis was supported by the Eni-MIT Energy fellowship and Solar Frontiers, the Chesonis Family Foundation under the Solar Revolution Project, the U.S. Department of Energy under contract numbers DE-FG02-96ER45571 and DE-FG02-05ER46253, and the National Science Foundation under grant number OCI-1147503 and through TeraGrid resources provided by Texas Advanced Computing Center under grant number TG-DMR970008S.

I thank my thesis advisor, Professor Gerbrand Ceder, for sharing with me his enthusiasm and visions in research that made this thesis possible, for his constructive feedback that nourished me, and for being an exemplary scientist whom I can look up to.

I thank my thesis committee, Professors Tonio Buonassisi and Jeffrey C. Grossman, for their complementary perspectives and expertise in experiment and theory.

I thank all members of the Ceder group, especially Kathy Simmons for all her kind help, Dr. Maria Chan for the guidance when I first joined the group, and my officemates, ShinYoung Kang, Rahul Malik, Yabi Wu, and Lusann Yang, for the cheerful atmosphere and celebrations.

I thank Professors Duane D. Johnson and Jim Zuo for the undergraduate research experience. As I look back, their encouragement and inspiration were invaluable. I acknowledge helpful discussions with Dr. Kristin Persson's group at Lawrence Berkeley National Laboratory, Professor Dane Morgan's group at the University of Wisconsin–Madison, and Ravishankar Sundararaman from Cornell University regarding joint density-functional theory and compilation of JDFTx.

I thank Dr. Elena Ruehr, Dr. Charles Shadle, Pamela Wood, Professor Keeril Makan, and Heng-Jin Park for the wonderful classes in music theory, composition, singing, and piano performance.

I am grateful to my family and all my friends for their love and support, especially to my wife, who has always been a source of motivation and joy.

S. D. G.

Contents

List of Figures **13**

List of Tables **15**

1 Introduction **17**
1.1 Pyrite FeS_2 for photovoltaic applications . . . 18
1.2 Thermodynamic effects of particle size and pH on the relative stability of polymorphs . . . 18
1.3 Overview of this thesis . . . 19

2 Electronic structure and relative stability of pyrite and marcasite **21**
2.1 Introduction . . . 21
2.2 Background . . . 22
2.2.1 Pyrite crystal structure . . . 22
2.2.2 Similarity of pyrite and marcasite crystal structures . . . 23
2.2.3 Proposed causes for low OCV of pyrite . . . 23
2.3 Details of first-principles computations . . . 26
2.3.1 Calculation method for surface and interfacial energies . . . 27
2.4 Intrinsic pyrite (100) surface . . . 28
2.4.1 Surface energies . . . 28
2.4.2 Surface states . . . 31
2.5 Pyrite and marcasite . . . 33
2.5.1 Volume dependence of the relative stability of pyrite and marcasite . . . 33
2.5.2 Model for epitaxial growth of marcasite on pyrite . . . 34
2.5.3 Possibility of marcasite epitaxial growth on pyrite . . . 34
2.5.4 Difference in bulk band gaps . . . 40
2.5.5 Absence of interfacial states within band gap . . . 40
2.6 Discussion . . . 43
2.7 Conclusions . . . 45

3 Intrinsic stoichiometry and oxygen-induced p-type conductivity of pyrite **47**
3.1 Introduction . . . 47
3.2 Methods . . . 48

3.2.1 First-principles computations . . . 48
3.2.2 Defect modeling . . . 48
3.3 Results . . . 52
3.3.1 Native defects . . . 52
3.3.2 Oxygen as an acceptor . . . 54
3.4 Discussion . . . 55
3.5 Conclusions . . . 60

4 Feasibility of pyrite band gap engineering 63
4.1 Introduction . . . 63
4.2 Methods . . . 64
4.2.1 Computational details . . . 64
4.2.2 Analysis framework . . . 65
4.2.3 Screening procedure . . . 66
4.3 Results . . . 66
4.3.1 Elements that form pyrite structure with S: Zn, Ru, Os . . . 66
4.3.2 Elements that do not form pyrite structures with S . . . 67
4.4 Discussion . . . 70
4.5 Conclusions . . . 77

5 Size-pH effects on the relative stability of FeS_2 polymorphs 79
5.1 Introduction . . . 79
5.2 Size dependence . . . 80
5.2.1 Theoretical framework . . . 80
5.2.2 Computational details . . . 81
5.2.3 Results . . . 81
5.3 pH dependence for charge-neutral particles . . . 84
5.3.1 Theoretical framework . . . 84
5.3.2 Computational details . . . 85
5.3.3 Results . . . 85
5.4 Charged particles . . . 86
5.4.1 The electrochemical potential $\overline{\mu}$ . . . 89
5.4.2 The electrochemical surface energy $\overline{\gamma}$ . . . 89
5.4.3 A theorem on $\overline{\gamma}$ . . . 90
5.5 Computational method . . . 93
5.5.1 Joint density functional theory . . . 93
5.5.2 Computational details . . . 95
5.6 Results . . . 95
5.6.1 Bulk and pristine surface calculations . . . 95
5.6.2 Charged surface calculations . . . 96
5.7 Discussion . . . 97
5.8 Future work . . . 100
5.8.1 Nonlinear PCM . . . 100

5.8.2 Partial charge transfer and partial coverage 102
5.9 Conclusions 102

6 Concluding remarks **103**

Bibliography **105**

Epilogue **115**

List of Figures

2-1 Unit cell of pyrite FeS_2. 22
2-2 Unit cell of marcasite FeS_2. 23
2-3 The unique, non-polar pyrite (100) surface. 25
2-4 Schematic of the ligand field model developed by Bronold *et al.* [12]. 26
2-5 Side view of pyrite (110) surface. 29
2-6 Side view of pyrite (111) surface. 29
2-7 Side view of pyrite (210) surface. 30
2-8 Wulff shape of pyrite within GGA-PBE. 30
2-9 GGA-PBE DOS of pyrite (a) bulk; (b) (001) surface. 31
2-10 PBE+U DOS of pyrite (a) bulk; (b) (001) surface. 32
2-11 Relative stability of pyrite and marcasite as a function of applied pressure within GGA-PBE. 35
2-12 Schematic of marcasite overgrowth on pyrite. 35
2-13 Structures of the pyrite (001)-marcasite (101) interface for $\theta = 270°$ and (a) $N = 3$; (b) $N = 4$. 37
2-14 The pyrite(001)–marcasite(101) interfacial energy, γ_{pm}, within GGA-PBE. . 39
2-15 Total energy (per formula unit) of pyrite (100)-marcasite (101)-vacuum supercell as a function of the number of epitaxial layers of marcasite, N. 39
2-16 PBE band structure of (a) pyrite and (b) marcasite. 41
2-17 DOS of bulk marcasite within GGA-PBE. 41
2-18 DOS of the lowest energy pyrite(001)-marcasite(101) interface (corner-sharing, $\theta = 270°$) within GGA-PBE. 42
2-19 DOS of pyrite (100) with Cl-adsorbates. 44
2-20 Voltage ratio ($v = qV_{oc}/E_g$) as a function of $x_g = E_g/kT_s \approx 1.93E_g$, where $T_s = 6000$ K is the temperature of the sun, predicted by Shockley-Queisser theory [1]. 45

3-1 Defect formation energy as a function of E_F at the Fe-rich limit, where $E_F^{\text{eq}} = 0.567$ eV. 54
3-2 Defect formation energy as a function of E_F at the S-rich limit, where $E_F^{\text{eq}} = 0.421$ eV. 55
3-3 Equilibrium Fermi level as a function of $\Delta\mu_{\text{O}}$ under $T_{\text{syn}} = 800$ K (solid circles) and $T_{\text{syn}} = 300$ K (open triangles). 56

3-4 Oxygen impurity concentration [c_O defined in Eq. (3.17) 56
3-5 Defect formation energy as a function of E_F at the Fe-rich limit and $\Delta\mu_O$ = 0.6 eV, where $E_F^{eq} = 0.458$ eV. 57
3-6 Charge density difference (rendered by VESTA [24]) between a supercell with an O_S^0 defect and the perfect FeS_2 host, viewed in the (111) plane. 59

4-1 PBE lattice constant of $Fe_xM_{1-x}S_2$ as a function of x. 67
4-2 Bulk modulus of $Fe_xM_{1-x}S_2$ as a function of x. 68
4-3 Band gap of $Fe_xM_{1-x}S_2$ as a function of x. 68
4-4 Mixing enthalpy of $Fe_xM_{1-x}S_2$ as a function of x. 70
4-5 Band gap bowing of $Fe_xM_{1-x}S_2$, where M=Be, Mg, Ca, Sr, Cd, Ba. 72
4-6 Mixing enthalpy of $Fe_xM_{1-x}S_2$, where M=Be, Mg, Ca, Sr, Cd, Ba. 72
4-7 Interaction parameter (Ω) as a function of (a) difference in electronegativity [99] ($\Delta\chi$); and (b) difference in Shannon ionic radius [98] (Δr). 75
4-8 Band structure of (a) ZnS_2; (b) RuS_2; and (c) OsS_2. 76

5-1 Wulff shapes of pyrite (left) and marcasite (right) obtained from pristine surface energies. 82
5-2 Relative stability of pyrite and marcasite as a function of particle size. 83
5-3 Surface energy versus pH diagram of pyrite. 86
5-4 Surface energy versus pH diagram of marcasite. 87
5-5 Wulff shape of pyrite (top) and marcasite (bottom). The pH is 1, 4, 7, 10, and 13 from left to right. 88
5-6 Size-pH phase diagram for FeS_2 polymorphs pyrite and marcasite. 88
5-7 Schematic of the differences between F, Ξ, n, and μ, and their relationship to $\gamma_{i^{0/\pm}}$, σ, and ϕ. 92
5-8 Pyrite (100), (110), (111), and (210) surface energy $\overline{\gamma}$ versus pH. 97
5-9 Marcasite (100), (010), (001), (110), (101), and (011) surface energy $\overline{\gamma}$ versus pH. 99
5-10 Fluid shape at the pyrite (100)/liquid interface. 100

List of Tables

2.1 Slab and vacuum size used to obtain pyrite surface energies. 27
2.2 Relaxed surface energies (in J/m^2) of pyrite FeS_2. 29
2.3 Lattice constants and relative stability of pyrite and marcasite. 34
2.4 Bulk energies (in meV/FU) of pyrite (p) and marcasite (m) referenced to the strain-free marcasite total energy. 38
2.5 Band gap (in eV) and k-points at VB and CB edges. 42

3.1 Defect formation energies and concentrations of O_S under Fe-rich environment and $\Delta\mu_O = 0.6$ eV. 57

4.1 Lattice constants (a_0 as calculated within PBE; in Å), bulk modulus (B in GPa), pressure derivative of the bulk modulus (B'), and Δ-sol fundamental gap (E_g in eV) of $Fe_xM_{1-x}S_2$. 69
4.2 Elastic constants (in GPa) and critical temperatures [T_c and T_c^* obtained from Eqs. (4.4) and (4.5), respectively; in K] of $Fe_{0.5}M_{0.5}S_2$. 69
4.3 Δ-sol fundamental gaps for elements that do not form the pyrite structure with S (E_g in eV). 71
4.4 Lattice constant (a_0 in Å), bulk modulus (B in GPa), pressure derivative of the bulk modulus (B'), and band gap (E_g in eV) of $Fe_xM_{1-x}S_2$ for candidates M that do not form the pyrite structure with S. 71
4.5 Shannon ionic radius [98] (r) and electronegativity [99] (χ) of M, and band gap bowing parameter (b_g) and interaction parameter (Ω) of $(Fe, M)S_2$. . . . 74

5.1 Pyrite and marcasite low-index pristine surface energies. 82
5.2 Comparison of lattice constants (in Å), pristine surface energies (in J/m^2), and relative stability (in meV/FU) of pyrite and marcasite between VASP and JDFTx computations. 96
5.3 Pyrite and marcasite surface energies (in J/m^2) with adsorbates H^+, H_2O, OH^-, and O^{2-}. 98
5.4 Pyrite and marcasite surface solvation energies (in J/m^2) with adsorbates H^+, H_2O, OH^-, and O^{2-}. 101

Chapter 1

Introduction

We waste our lights in vain.

William Shakespeare

A photovoltaic (PV) material is one that can convert light energy into electric energy. Given the solar spectrum, a PV material must be a semiconductor with a band gap around 1–2 eV, since much of the absorbed energy is wasted due to thermal relaxation in a small-gap material, and only a small fraction of the solar spectrum is absorbed by a high-gap material. A mathematical consideration of the detailed balance between absorption and loss processes has led to the well-known Shockley-Queisser limit, where a maximum efficiency of over 30% can, in principle, be obtained for a single-junction material with a 1.4-eV band gap [1]. Although silicon has a somewhat suboptimal band gap (1.1 eV) and low absorption coefficient (10^3 cm^{-1}), it has remained the most favored commercial PV material due to its abundance, the capability of manufacturing stable and high-purity single crystals on a large scale (via Czochralski or float-zone methods), and the ease of doping [2].

After decades of device optimization, nowadays commercial Si solar panels have reached efficiencies around 20%. However, for photovoltaics to become competitive compared to fossil fuels, the manufacturing cost still needs to be reduced significantly and efficiency should be maximized. In response to this demand, the rationale of PV research can be divided into two classes, namely, continued optimization of Si and discovery of new materials. The former is driven by the motivation of improving the absorption properties of Si, and has led to such innovations as texturized surfaces and black Si, whereas the latter has led to the design of "second generation" thin film photovoltaics [e.g., $CuInGaSe_2$ (CIGS) and CdTe] and "third generation" concepts such as hot carrier cells, intermediate band cells, and multijunction cells [3].

Motivated by the requirement of scalability and the search for a new material with potentially better properties than Si, this thesis will focus on the study of pyrite FeS_2, the most abundant sulfide mineral on earth [4].

A second theme of this thesis arises as an attempt to understand the effect of aqueous environment on the phase stability of a material with competing polymorphs during synthesis. The ability to control the synthesis of the desired phase is of crucial importance in

the manufacturing industry. We will use the FeS_2 polymorphs, pyrite and marcasite, as our model system.

1.1 Pyrite FeS_2 for photovoltaic applications

In many aspects, pyrite is a promising PV material due to its earth-abundance [4], non-toxic elements, suitable band gap (0.95 eV) [5], and, most importantly, its excellent optical absorptivity [6]. Although an indirect gap material, its optical absorption coefficient within the visible light spectrum is on the order of 10^5 cm^{-1} [5], outperforming silicon by two orders of magnitude and even direct gap materials such as GaAs. In a recent cost analysis for large-scale PV applications, pyrite is ranked number one among all practical or promising thin-film solar cell materials [7]. However, experiments in the mid-1980s and 1990s show a persistently low open-circuit voltage (OCV) of around 200 mV, which is the primary factor that reduces the efficiency of pyrite photoelectrochemical cells to 2% [5]. Thus, it is important to understand what limits the OCV and how it can be enhanced.

To assess and understand the PV properties of pyrite, we shall investigate the roles of secondary phases (in particular the polymorph marcasite), intrinsic and extrinsic defects, and band gap engineering via cation alloying.

1.2 Thermodynamic effects of particle size and pH on the relative stability of polymorphs

The relative stability of polymorphs under different environments can often be explained through the effects of the relevant thermodynamic forces. The effect of particle size is well understood in terms of surface energies and surface-to-bulk ratios [8],

$$G = g_b V + \gamma A, \tag{1.1}$$

where g_b is the bulk Gibbs free energy density, γ is the surface energy, A is the surface area, and V is the volume of the particle. For instance, the polymorphs of TiO_2, ranked in decreasing order of stability as well as surface energy, are rutile, brookite, and anatase, which explains the observation that while rutile is the stable phase in the bulk limit, brookite and anatase are favorable at the nanoscale [8].

Due to the difficulty of the problem, a rigorous and quantitative treatment of γ in aqueous environments with varying pH has not been achieved. It is obvious that, in the liquid region, a brute force approach of simulating proton and hydroxyl concentrations spanning 14 orders of magnitude is not computationally feasible. Likewise, in the solid region, computing total free energies of single-crystal particles across different length scales is also impossible from first principles. The solid-liquid interface adds yet another layer of complexity to the picture. Therefore, as a first approximation, vastly simplifying assumptions must be made, which will be explicitly stated, in order to improve our understanding of the role of the relevant

thermodynamic forces in this problem.

We shall address how the combined effects of particle size and pH may alter the stable and metastable phases using pyrite and marcasite FeS_2 as a model system, where the metastable phase marcasite is known to be stabilized in acidic solutions [9–11].

1.3 Overview of this thesis

The remainder of the thesis is organized as follows. In Chapters 2, 3, and 4, the PV properties of pyrite are investigated. Specifically, we will examine the roles of intrinsic surface states and marcasite in Chapter 2. The role of intrinsic defects and oxygen impurities are studied in Chapter 3, to address whether pyrite is stoichiometric when pure and the cause for its *p*-type conductivity. In Chapter 4, we shall look at the feasibility of band gap engineering in pyrite to see whether its band gap can be enhanced via cation alloying. The general question of how particle size and pH of the aqueous environment during synthesis affects the relative stability of polymorphs will then be addressed in Chapter 5, where we shall use the FeS_2 polymorphs as a model system. Concluding remarks are finally given in Chapter 6.

Chapter 2

Electronic structure and relative stability of pyrite and marcasite

Doubt is not a pleasant condition, but certainty is absurd.

VOLTAIRE

2.1 Introduction

As mentioned in Chapter 1, its low open-circuit voltage (OCV) has prevented the use of pyrite as a commercially viable device for PV applications. There have been many proposals in the literature regarding the cause of the low OCV in pyrite. They can be classified into three main categories: (i) Intrinsic surface states. Bronold and co-workers have suggested that intrinsic {100} surface states appear as gap states, thereby pinning the Fermi level [12, 13, 5, 14, 15]. (ii) Presence of marcasite. Wadia and co-workers have suggested that trace amounts of marcasite, a polymorph of pyrite with a significantly lower band gap, would deteriorate the photovoltaic performance of pyrite [16, 17]. (iii) Defects. Various research groups have suggested that electronic states can be introduced into the band gap due to intrinsic defects such as bulk sulfur vacancies [18, 19] and surface sulfur vacancies [20]. Abd El Halim *et al.* have also suggested the possibility of line defects and extrinsic point defects [21]. Oertel *et al.* have attributed the poor performance to the limitation of carrier transport by trap states at grain boundaries [22]. In this study, we mainly focus on the possible role of surface states (i) and marcasite formation (ii). Our results question these explanations for the low OCV. The effect of defects (iii) shall be considered in Chapter 3.

In Sec. 2.2, we will first examine the pyrite and marcasite crystal structures, their similarities, and the possibility of marcasite epitaxial growth on pyrite, followed by more detailed discussions on the different proposed causes for the low OCV of pyrite. First-principles computational details will be presented in Section 2.3. In Sec. 2.4, we will discuss surface energies and electronic structure calculations of pyrite, as they are related to the intrinsic

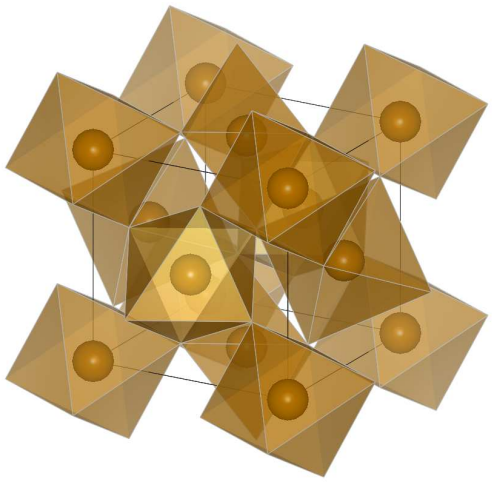

Figure 2-1: Unit cell of pyrite FeS_2. The spheres at fcc sites are Fe atoms. Each Fe atom sits in a slightly distorted octahedral environment of S atoms, which are located at the octahedral vertices.

surface-state hypothesis (i). In Sec. 2.5, the thermodynamic epitaxial growth condition of marcasite on pyrite, and the electronic structures of the bulk phases and the pyrite-marcasite interface will be analyzed to investigate the marcasite hypothesis (ii).

2.2 Background

2.2.1 Pyrite crystal structure

The formula unit of pyrite is FeS_2, where the oxidation states of Fe and S are +II and −I, respectively [23]. The structure belongs to the space group $Pa\bar{3}$. The conventional unit cell is shown in Fig. 2-1. (All figures of unit cells and surfaces are generated by VESTA [24].) Fe atoms are located at face-centered cubic (fcc) sites, whereas S atoms form distorted octahedra around Fe. The positions of all the S atoms can be described by a single Wyckoff parameter, u. These positions are: $\pm(u,u,u), \pm(\frac{1}{2}+u,u,\frac{1}{2}-u), \pm(u,\frac{1}{2}-u,\frac{1}{2}+u)$, and $\pm(\frac{1}{2}-u,\frac{1}{2}+u,u)$. Each S atom is tetrahedrally coordinated by three Fe atoms and one S atom, with which the S_2 dimer is formed [4]. The centers of the S_2 dimers form an fcc sublattice that interpenetrates the Fe sublattice. Thus, the pyrite structure can be viewed as a slight modification of the NaCl structure, such that each Cl site is occupied by $\langle 111\rangle$-oriented S_2 dumbbells.

It is well-known from crystal field theory that the energies of transition-metal d orbitals are non-degenerate within an octahedral environment [25]. Specifically for FeS_2, the triply degenerate d_{xy}, d_{yz}, and d_{xz} states, collectively known as t_{2g}, dominate the valence band (VB), whereas the doubly degenerate d_{z^2} and $d_{x^2-y^2}$ states, collectively known as e_g, dominate the conduction band (CB). Both pyrite and marcasite are low spin (LS) semiconductors because their t_{2g} levels are fully occupied by the six Fe d electrons [26]. The ligand field theory of various materials that have the pyrite or marcasite crystal structure is discussed in Ref. [26].

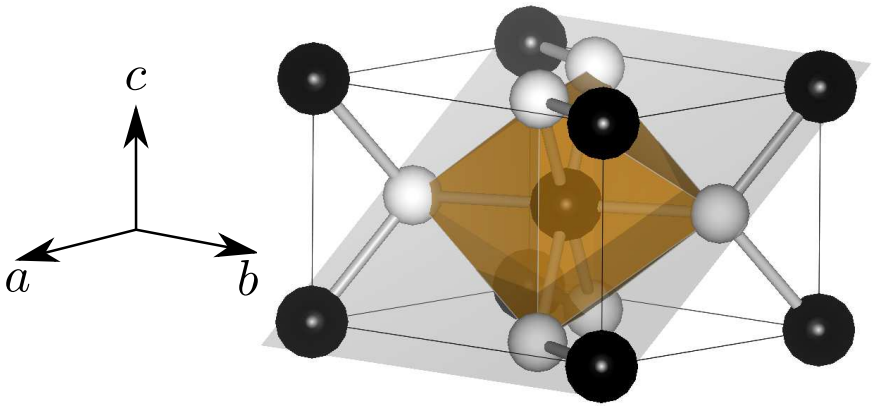

Figure 2-2: Unit cell of marcasite FeS_2. Black (white) spheres represent Fe (S) atoms. The (101) plane is highlighted in grey. The octahedra is edge-shared by the S atoms on the (001) faces.

2.2.2 Similarity of pyrite and marcasite crystal structures

Marcasite forms an orthorhombic *Pnnm* with unit cell shown in Fig. 2-2. Note the octahedral environment around the body-centered Fe atom. By repeating the unit cell, one can see that the octahedra in marcasite are edge-shared, whereas those in pyrite are corner-shared (Fig. 2-1). Experimentally, the lattice constant of pyrite is $a = 5.416$ Å [4]; the lattice constants of marcasite are $a = 4.443$ Å, $b = 5.425$ Å, $c = 3.387$ Å [27]. Note that the b-constant and the [101] length ($\sqrt{a^2 + c^2} = 5.587$ Å) of marcasite are similar to the pyrite lattice constant, with lattice mismatches of 0.2% and 3%, respectively. The structural relationship between the different octahedra linkages in pyrite and marcasite is discussed in Ref. [28]. The pyrite-marcasite structural transformation can be described by a rotation of Fe–S chains in alternating layers of the (101) marcasite plane, as discussed in Ref. [29]. Indeed, due to their structural similarities, intergrowth/epitaxial growth of marcasite in/on pyrite has been widely observed [30–32, 16]. The thermodynamic conditions for such growth behavior will be discussed in later sections.

2.2.3 Proposed causes for low OCV of pyrite

Intrinsic surface states

Figure 2-3 shows the (001) surface of pyrite. Of the three possible terminations, only one is non-polar. [S–Fe–S] patterns repeat along the surface normal direction in Fig. 2-3(a). Polar surfaces are created from the terminations that yield [S–S–Fe] or [Fe–S–S] as the three layers nearest to the surface. In the non-polar surface, ending as [S–Fe–S], the coordination number of a surface Fe atom is 5, being 1 lower than that of a bulk Fe atom. The local coordination of S around Fe is reduced from octahedral to square pyramidal, as illustrated in Fig. 2-3(b).

The ligand field model developed by Bronold *et al.* to describe the local electronic structure is shown schematically in Fig. 2-4 [12]. Bronold *et al.* estimate the octahedral splitting energy 10 Dq to be 2 eV based on the centers of mass of the CB and VB density of states

(DOS), in the electronic structure calculation by Folkerts *et al.* [33]. Using the splitting energies of the square pyramidal configuration ($d_{x^2-y^2}$ at 9.14 Dq; d_{z^2}, d_{xy} at $\pm$0.86 Dq; d_{xz}, d_{yz} at -4.57 Dq) calculated by Krishnamurthy and Schaap [25], they claim that the d_{z^2} and d_{xy} states are split off from the e_g and t_{2g} states in the CB and VB, respectively, thereby introducing two gap states a_1 and b_2 [12]. It should be pointed out that the splitting energies are greatly influenced by the choice of a free parameter ρ [25]. Without justification, Bronold *et al.* implicitly assume $\rho = 2$ in their model. For this particular choice of ρ, gap states are centered at 4 Dq (0.8 eV) above the center of mass of the t_{2g} states in the VB and separated from each other by 1.7 Dq (0.35 eV). They suggest that the Fermi level is pinned by these states, hence reducing the OCV. As the Bronold model is not free of parameters, we will examine the claims of gap states by direct *ab initio* electronic structure calculations.

Presence of marcasite

Phase purity is a critical issue in photovoltaic devices, especially if secondary phases have a lower band gap than the host material, or if they introduce interfacial states within the band gap that may lead to Fermi level pinning. For instance, due to its metallic character, trace amounts of the Fe-deficient pyrrhotite phase ($Fe_{1-x}S$) are detrimental to the photovoltaic performance of pyrite [32]. Thomas *et al.* have shown that there exists a critical S partial pressure above which growth of pyrrhotite can be avoided [32]. Since pyrrhotite is not commonly reported to intergrow with pyrite, and the means to prevent its growth have been developed, the pyrrhotite phase will not be examined in this study.

Another cause for the low OCV of pyrite is attributed to the presence of its polymorph, marcasite [16]. Intergrowth of these two phases has been widely reported (see, e.g., Refs. [31, 32, 16]). In addition, epitaxial overgrowth of marcasite (101) on pyrite (001) has been observed from natural samples [30]. While there has been no study on the mechanism of how marcasite may affect the photovoltaic performance of pyrite, it has been speculated that the lower gap of marcasite plays a role. There is only one published experimental value of the band gap of marcasite (0.34 eV), which is much lower than that of pyrite. This value is obtained using resistivity measurements with the assumption that the carrier mobility is dominated by lattice scattering [34]. As far as the authors are aware, there are no other reports on the gap of marcasite and its value has never been verified via a more reliable and direct method such as optical measurements. Intuitively, one may reason that marcasite should have a lower gap than pyrite, because marcasite has lower symmetry compared to pyrite, and hence enhanced crystal-field splitting [35]. Nonetheless, there is no direct, unambiguous evidence that marcasite has a lower gap than pyrite.

To model the pyrite-marcasite system, one should first understand their relative stability. From calorimetric measurements, pyrite is the ground-state phase within 5–700 K, and the marcasite-to-pyrite phase transformation is found to be exothermic [27]. Computationally, Spagnoli *et al.* find that the relative phase stability depends on the exchange-correlation functional: while marcasite is the ground state within the local density approximation (LDA) and the generalized gradient approximation (GGA) within the Perdew-Burke-Ernzerhof formulation (PBE), pyrite is more stable within recently developed GGA functionals such as

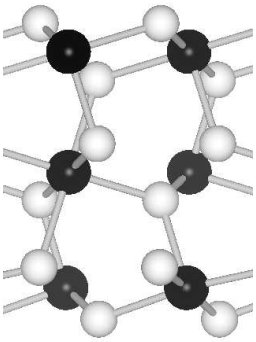

(a)

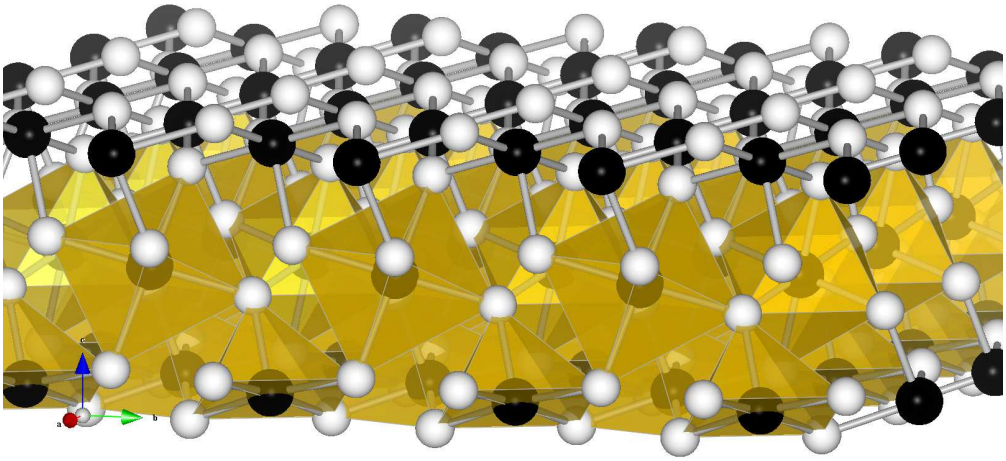

(b)

Figure 2-3: (a) Side view of the unique, non-polar pyrite (100) surface. Looking along the surface normal direction (upwards), the atomic layers have the repetitive pattern [S–Fe–S]. Other possible terminations result in repeating layers of [S–S–Fe] or [Fe–S–S]. In both cases, polar surfaces result. Hence, this S-terminated surface is the only possible non-polar (100) surface. In (b), note the octahedral environment around bulk Fe atoms, and the square pyramidal environment around surface Fe atoms. Black (white) spheres are Fe (S) atoms.

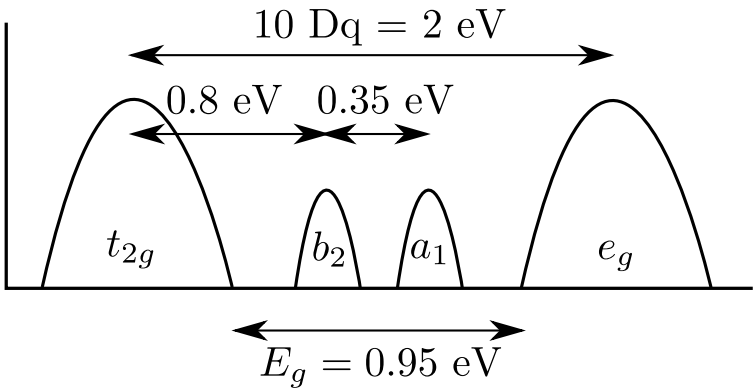

Figure 2-4: Schematic of the ligand field model developed by Bronold *et al.* [12]. The CB and VB are dominated by e_g and t_{2g} states, respectively. As a result of symmetry reduction, a_1 and b_2 states, which correspond to d_{z^2} and d_{xy} states, are introduced within the band gap.

AM05, Wu-Cohen, and PBEsol [17]. There has been no prior computational work on the thermodynamic stability of epitaxial growth of marcasite on pyrite. Whether interfacial states are introduced into the pyrite band gap by marcasite is also unknown. All of the above issues will be addressed in this work.

2.3 Details of first-principles computations

Density-functional theory (DFT) [36,37] calculations with projector augmented wave (PAW) potentials [38, 39] were performed using the plane-wave code Vienna Ab-initio Simulation Package (VASP) [40–43]. We used both the local-density approximation (LDA) [44] and the generalized gradient approximation (GGA) to the exchange-correlation functional. Two formulations of GGA, namely, Perdew-Burke-Ernzerhof (PBE) [45, 46] and AM05 [47, 48], were adopted. The spin states of pyrite and marcasite are determined from spin-polarized DFT calculations [49, 50]. For cases in which the Hubbard U correction within the Liechtenstein scheme [51] was applied to GGA calculations, we chose the parameters $U = 3$ eV and $J = 1$ eV that correctly predict the high spin state of Fe under negative pressure, as discussed in Ref. [52].

The plane wave energy cutoff was 350 eV for all calculations. Within each self-consistency cycle, the total energy was converged to within 10^{-6} eV. Forces in ionic relaxations were converged to within 0.01 eV/Å. Convergence tests with respect to energy cutoff, Monkhorst-Pack [53] k-point density, supercell size, and vacuum size were performed such that surface and interfacial energies were converged to within 0.01 J/m^2. For bulk reference energies, we used a k-mesh of $8 \times 8 \times 8$ for pyrite (12-atom unit cell) and $8 \times 6 \times 10$ for marcasite (6-atom unit cell). Kohn-Sham gaps were computed using a Γ-centered k-mesh of $16 \times 16 \times 16$ for pyrite and $16 \times 12 \times 20$ for marcasite. Band structures were obtained from subsequent non-self-consistent calculations with 15 k-points per high-symmetry line. For surface and interfacial calculations, we used a k-mesh of $4 \times 4 \times 1$. Surface terminations were chosen

Table 2.1: Slab and vacuum size used to obtain pyrite surface energies. Here we define a unit cell as the smallest orthorhombic cell whose basal plane is the desired surface. The number of repetitions of such a cell along the z direction is denoted by N. This should not be confused with the definition of the number of [S–Fe–S] layers in Sec. 2.5.

Surface	N	Vacuum size (Å)
(100)	2	6
(110)	2	8
(111)	1	6
(210)	1	8

to generate non-polar supercells, avoiding dipole effects under periodic boundary conditions (see Ref. [54] for details). Details of the approach used to obtain surface and interfacial energies converged with respect to slab and vacuum sizes are given in the next subsection. At convergence, the (100), (110), (111), and (210) pyrite slabs contained 24, 48, 72, and 60 atoms, respectively. Supercells of the pyrite-marcasite interface contained 36 ($N = 3$) to 120 ($N = 10$) atoms. (See Sec. 2.5.3 for the definition of N.)

2.3.1 Calculation method for surface and interfacial energies

Surface energies were calculated from the equation

$$\gamma = \lim_{N\to\infty} \frac{E^N_{\text{slab}} - NE_{\text{bulk}}}{2A}, \tag{2.1}$$

where E^N_{slab} and E_{bulk} are the total energies of the slab and bulk, respectively, N is the supercell size, $A = ||\mathbf{T}_1 \times \mathbf{T}_2||$ is the cross-sectional area of the supercell ($\mathbf{T}_i$ is the translation vector along the i direction, where $i = 1, 2, 3$ corresponds to x, y, z), and the factor of 2 accounts for the presence of 2 surfaces under periodic boundary conditions. Surface energies were relaxed and converged to within 0.01 J/m^2 with respect to the number of layers and vacuum size (Table 2.1).

The interfacial energy between two phases α and β can be calculated from

$$\gamma_{\alpha\beta} = \lim_{N_\alpha, N_\beta\to\infty} \frac{E^{N_\alpha+N_\beta}_{\text{int}} - N_\alpha E^\alpha_{\text{bulk}} - N_\beta E^\beta_{\text{bulk}}}{2A}, \tag{2.2}$$

where N denotes the number of layers for each phase. However, due to different cell shapes and k-point densities, it may be inaccurate to use the bulk energies obtained from unit cell calculations as reference energies for the supercells. Instead, one can obtain the average bulk reference energy, E_b, by fitting the total energy of the interface supercell versus the number of layers with a straight line, in the fashion developed by Fiorentini and Methfessel [55].

Note that when $N = N_\alpha = N_\beta$,

$$E_{\text{int}}^{2N} \approx 2\gamma_{\alpha\beta}A + NE_{\text{bulk}}. \tag{2.3}$$

The bulk reference energy E_{bulk} must be fitted separately for each θ and parity of N. Substituting the fitted E_{bulk} into Eq. (2.2), γ can be obtained as a function of N.

We use the Fiorentini-Methfessel method [55] to obtain the interfacial energy between marcasite and pyrite. The marcasite (101) cell is strained such that $a' \equiv \sqrt{a_m^2 + c_m^2} = a_p$, $b_m = a_p$, and $c/a = 1$, as discussed in the main text. By inserting a vacuum layer to this cell, the marcasite (101) surface energy is calculated to be 0.72 J/m^2. The corresponding strain energies within GGA-PBE are given in Table 2.4. The strain energies are on the order of 100 meV/FU, much higher than the relative stability energy between the two phases, which is on the order of 10 meV/FU, from Table 2.3.

2.4 Intrinsic pyrite (100) surface

We divide our results into two parts. In this section (2.4), we present the surface energies of pyrite (2.4.1) and electronic densities of states (DOS) for the dominant surface (2.4.2). We compare our first-principles calculations with the ligand field calculations of Bronold *et al.* [12]. In Sec. 2.5, we first show how the bulk, surface, interfacial, and strain energies of pyrite and marcasite are used in an energy model to predict whether epitaxial growth of marcasite on pyrite is thermodynamically favorable (Secs. 2.5.2 and 2.5.3). We then examine the electronic structure at the pyrite-marcasite interface to verify whether marcasite can undermine the OCV of pyrite (Secs. 2.5.4 and 2.5.5).

2.4.1 Surface energies

The most commonly observed surfaces of pyrite are {100}, {110}, {111}, and {210} [4]. Figures 2-3, 2-5, 2-6, and 2-7 show the corresponding structures. A detailed description of the structures of these surfaces can be found in Refs. [56–58]. The surface energies are calculated via Eq. (2.1). For all functionals used, the {100} surface has the lowest energy, as shown in Table 2.2. Our PBE surface energies agree well with another first-principles investigation by Hung *et al.*, who used the same exchange-correlation functional [56, 57]. We observe that the surface energies are lowest in PBE, followed by AM05, and largest in LDA. However, the relative magnitudes are consistent across functionals. The Wulff shape, i.e., the equilibrium shape of a single crystal, of pyrite is shown in Fig. 2-8. Besides the dominant {100} surface, only {111} facets are observed. Hence, the minimum-energy structure of pyrite is the cubo-octahedral structure. Since the relative surface energies are similar for different functionals, the predicted Wulff shape is independent of the functional used, despite significant functional dependence of the surface energies themselves.

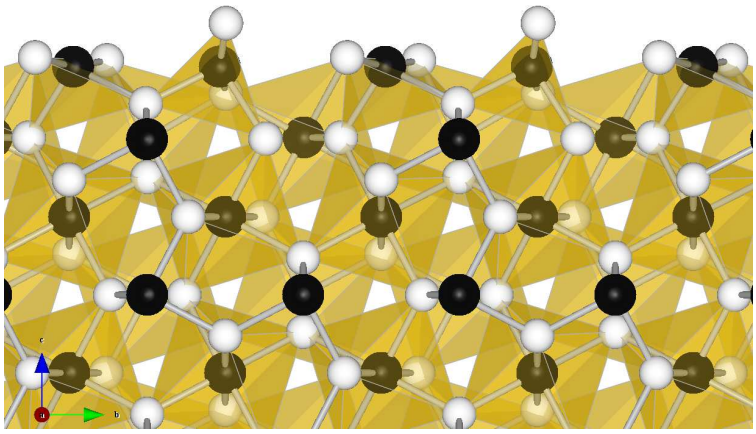

Figure 2-5: Side view of pyrite (110) surface. Black (white) spheres are Fe (S) atoms. The surface is non-polar and S-terminated.

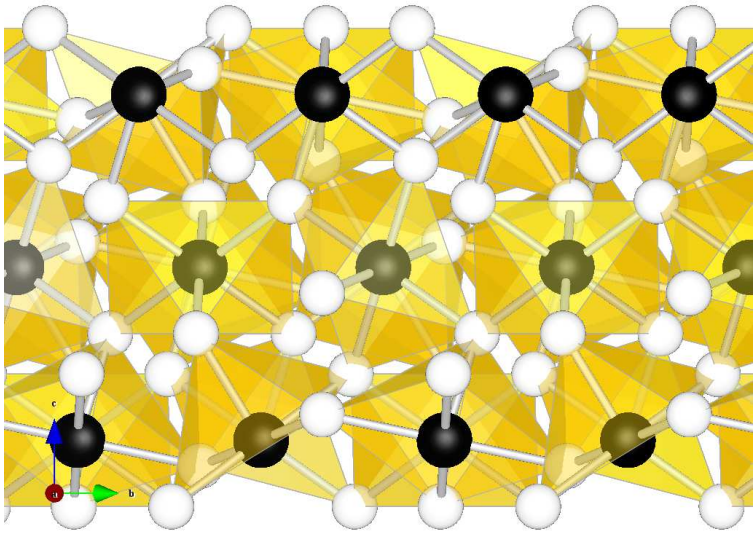

Figure 2-6: Side view of pyrite (111) surface. Black (white) spheres are Fe (S) atoms. The surface is non-polar and S-terminated.

Table 2.2: Relaxed surface energies (in J/m^2) of pyrite FeS_2. PBE results are compared with Refs. [56, 57], where PBE was used. AM05 energies for (111) and (210) surfaces are not available due to convergence issues.

Surface	LDA	AM05	PBE	Hung *et al.* [56, 57]
(100)	1.58	1.26	1.04	1.06
(110)	2.38	2.02	1.72	1.68
(111)	2.01	-	1.43	1.40
(210)	2.13	-	1.49	1.50

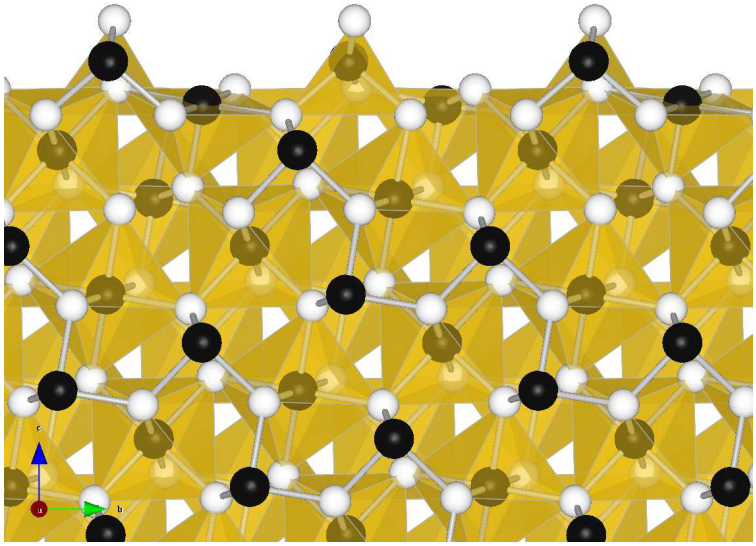

Figure 2-7: Side view of pyrite (210) surface. Black (white) spheres are Fe (S) atoms. The surface is non-polar and S-terminated.

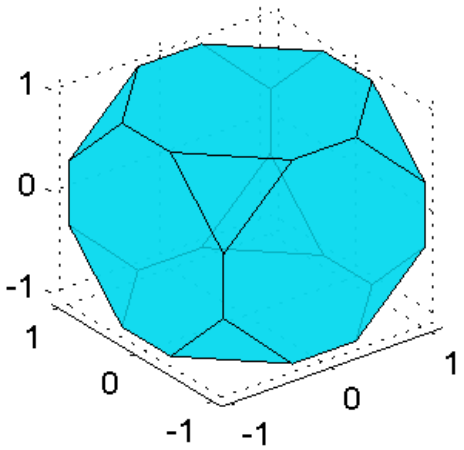

Figure 2-8: Wulff shape of pyrite within GGA-PBE. Surface energies are taken from Table 2.2. The dominant surface is {100}. {111} facets are also observed. The equilibrium shape is cubo-octahedral.

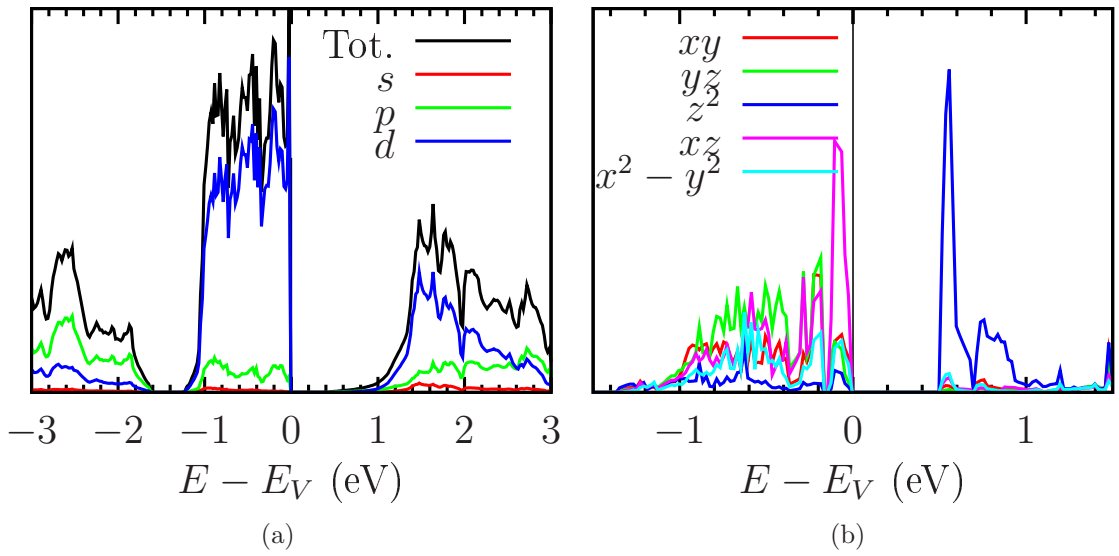

Figure 2-9: GGA-PBE DOS of pyrite (a) bulk; (b) (001) surface. In (a), both the total DOS and *s*-*p*-*d* decomposed DOS are shown. The CB and VB are dominated by Fe *d* states. We have verified that these *d* states within the CB and VB are e_g and t_{2g}, respectively. Due to the presence of a S *p* state, the CB tail extends to 0.4 eV above the VB edge. In (b), the DOS of *d*-orbitals are shown to identify the character of intrinsic surface states. The intrinsic surface state appears at the CB edge, not within the band gap, and is characterized to be of d_{z^2} character. However, ligand field splitting in the VB is not observed and d_{xy} surface states are not found, contrary to the prediction of Bronold and co-workers [12].

2.4.2 Surface states

As {100} is the dominant surface, we investigate the surface states of this facet. To obtain the exact character of the surface states, the coordinate frame is rotated into the Fe–S bonds prior to projection onto partial *d* states [59]. The DOS of bulk pyrite and the (100) surface are compared in Fig. 2-9. For bulk pyrite, the Kohn-Sham gap is 0.40 eV within PBE. The tail in the CB is due to an S *p* state. The VB and CB are dominated by t_{2g} and e_g states, respectively (not shown), agreeing with ligand field theory [26]. For the (100) surface, we only observe a pronounced d_{z^2} state that is pulled down from the conduction-band manifold of e_g states, but not inside the gap. The d_{xy} gap state predicted by Bronold *et al.* [12] is not seen. We have also performed the same calculation within LDA and AM05. However, gap states are not found.

Hubbard U correction

One may question whether the intrinsic surface states would become gap states if the band gap were more accurately calculated, since the Kohn-Sham (KS) gap severely underestimates the band gap. Hence, it may be desirable to apply a Hubbard U correction, which has been shown to be successful in transition-metal electronic structure calculations. (See, e.g.,

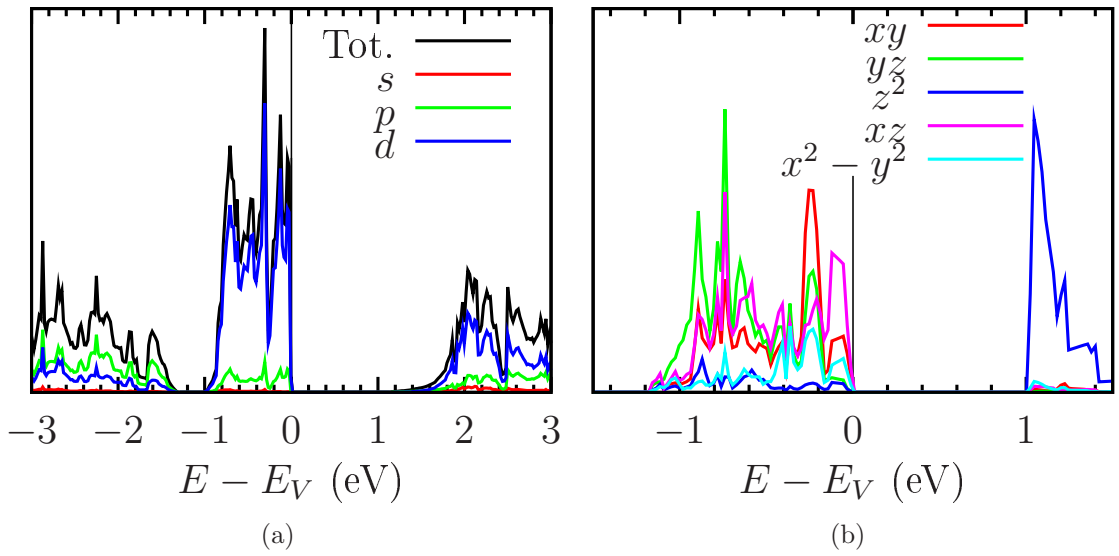

Figure 2-10: PBE+U DOS of pyrite (a) bulk; (b) (001) surface. In (a), both the total DOS and the s-p-d decomposed DOS are shown. The PBE+U gap of bulk pyrite is 1.03 eV. In (b), the DOS of d-orbitals are shown to identify the character of intrinsic surface states. Similar to Fig. 2-9(b), a d_{z^2} surface state is found at the CB edge. Gap states are not observed.

Refs. [60] and [61].) However, as the surface states and CB states are of d character, we expect that the same qualitative results should be obtained within GGA+U. To verify, we perform PBE+U calculations, following Persson *et al.* for the choice of U and J. The effective $U = 2$ eV is chosen to correctly predict a pressure-induced spin transition [52]. Fe^{2+} in pyrite has a d^6 electronic configuration; pyrite is both expected and observed to be low spin (LS) [26]. We verify that the LS configuration is the ground state within both PBE and PBE+U. By applying the Hubbard U correction to pyrite in the LS configuration, the KS gap is increased to 1 eV, which happens to coincide with the experimental band gap. We emphasize that the U value is not fitted to the band gap.

Since the conduction band is dominated by d states, we expect it to shift upward with respect to the VB edge. Moreover, as the intrinsic surface states at the conduction band minimum (CBM) are also d states, they should move along with the CB. We verify that these intrinsic surface states are not gap states within PBE+U. As shown in Fig. 2-10, intrinsic surface states and the CB are shifted by the same amount, as compared to PBE. The d_{z^2} surface states are still located at the CB edge, and no gap states are found.

From the above discussion, we observe several discrepancies between first-principles calculations and the Bronold model [12]. First, the Bronold model predicts two types of intrinsic surface states; however, only the d_{z^2} surface state is observed within DFT. Within the VB, the predicted d_{xy} state is not observed to move toward the band edge. The fact that the t_{2g} states remain fairly degenerate at the symmetry-broken surface suggests that applying the parameters from the simplified model of Krishnamurthy and Schaap [25] is inadequate to capture the physics of the electronic structural properties of the pyrite (100) surface. Second,

the Bronold model predicts that these surface states are gap states, leading to Fermi level pinning and undermining the photovoltaic performance of pyrite; however, the surface states are not found within the band gap, regardless of the exchange functional used and whether or not we apply the Hubbard U correction. Therefore, we conclude that intrinsic surface states are unlikely to be the cause of the low OCV in pyrite.

2.5 Pyrite and marcasite

2.5.1 Volume dependence of the relative stability of pyrite and marcasite

From total energy calculations of the bulk phases, we find that the thermodynamic ground state is marcasite in PBE and PBE+U, but pyrite in LDA and AM05. As shown in Table 2.3, pyrite is 21.6 meV/FU less stable than marcasite within GGA-PBE, but 8 meV/FU more stable within LDA and AM05. These results agree with the relative stability reported by Spagnoli *et al.* [17], except for the LDA calculation. They report that marcasite is the ground state within LDA, with a relative energy difference of 31 meV/FU [17]. However, we find that pyrite is the ground state within LDA. To verify whether the prediction of the relative phase stability is simply a volume issue, we plot in Fig. 2-11 the PBE energy difference between pyrite and marcasite as a function of pressure. For pressures larger than 2.8 GPa, pyrite is favored. At this critical pressure, the conventional cell volumes of pyrite and marcasite are expected to be about 155 and 80 Å^3, respectively, which are higher than the equilibrium volumes within LDA and AM05. Upon further increase in pressure until $P = 4$ GPa, the volumes are reduced and the energy difference (-8.6 meV/FU) coincides with the $P = 0$ calculations within LDA and AM05. Hence, prediction of the relative stability can be corrected by decreasing the volume, either by artificially applying a pressure within PBE, or using LDA/GGA-AM05.

We remark that the lattice constant calculated within GGA-PBE is underestimated compared to experiment, which is unusual. Extrapolation of the experimental lattice constant of pyrite using its thermal expansion coefficient [62] yields about 5.41 Å at 0 K, which is still 0.2% larger than the PBE lattice constant at zero pressure, and 2% larger than the LDA lattice constant. Thus, there is a trade-off between the prediction of relative stability and equilibrium volume. In particular, while the AM05+U ($U_{\text{eff}} = 2$ eV) lattice constants and band gap (Table 2.5) show better agreement with the experimental values, the ground-state phase is predicted to be marcasite. All LDA, PBE, and AM05 calculations presented in the main text are performed at the equilibrium lattice constant corresponding to the functional being used.

Our work shows that qualitative trends in the electronic structure are independent of the functionals considered, and that either LDA, AM05, or HSE06 can be used to predict the correct bulk ground state phase. At the pyrite-marcasite interface, the DOS plots and interfacial energies are consistent across functionals. The functional dependence of properties that have not been studied in this work (e.g., phonon) is unknown. We have made an effort

Table 2.3: Lattice constants and relative stability of pyrite and marcasite. Within LDA and AM05, pyrite is the ground state, in agreement with experiment [27]. Within GGA-PBE, marcasite is the ground state. However, as pressure is increased, the volumes of the two phases decrease, and pyrite becomes more energetically favorable relative to marcasite. Within HSE06, pyrite is 5.2 meV/FU more stable than marcasite at the experimental lattice constants.

		Pyrite		Marcasite				
	P (GPa)	a (Å)	V (Å^3)	a (Å)	b (Å)	c (Å)	V (Å^3)	$E_p - E_m$ (meV/FU)
Experiment[a]		5.416	158.9	4.443	5.425	3.387	81.64	−43.4
LDA	0	5.2875	147.82	4.3374	5.2974	3.3201	76.284	−8.4
AM05	0	5.3171	150.33	4.3615	5.3283	3.3415	77.653	−8.8
AM05+U	0	5.3325	151.32	4.3599	5.3323	3.3491	77.859	7.1
PBE	0	5.4029	157.72	4.4382	5.4094	3.3884	81.350	21.6
	2	5.3806	155.77	4.4164	5.3882	3.3753	80.321	6.3
	4	5.3605	154.03	4.3954	5.3682	3.3624	79.338	−8.6
	6	5.3406	152.32	4.3778	5.3491	3.3499	78.446	−23.1
	8	5.3212	150.67	4.3598	5.3309	3.3378	77.575	−37.3
	10	5.3048	149.29	4.3431	5.3139	3.3265	76.772	−51.1
PBE+U	0	5.4239	159.56	4.4373	5.4209	3.4068	81.949	24.9

[a] Lattice constants are taken from Ref. [4] (pyrite) and Ref. [27] (marcasite). Enthalpies of formation at 298.15 K are taken from Ref. [27].

to illustrate that while relative stability and volume depend on the functional, the electronic properties pertaining to the photovoltaic performance of pyrite do not.

2.5.2 Model for epitaxial growth of marcasite on pyrite

Epitaxial growth of marcasite (101) on pyrite (001) is shown schematically in Fig. 2-12. The condition for marcasite growth on pyrite to be energetically favorable is

$$A(\gamma_{pm} + \gamma_{mv} - \gamma_{pv}) + N\Delta g < 0, \tag{2.4}$$

where γ is the surface or interfacial energy between marcasite (101) (m), pyrite (001) (p), and/or vacuum (v), N is the number of layers of marcasite (number of S–Fe–S stacking motifs along the z direction), Δg is the magnitude of the free-energy difference per layer, and A is the cross-sectional area. From this energy balance equation, the critical N can be calculated for a given set of surface and interfacial energies.

2.5.3 Possibility of marcasite epitaxial growth on pyrite

Different pyrite (100)–marcasite (101) interfaces can be created depending on the orientation angle θ and the parity of the number of layers. (We use the Fiorentini-Methfessel method [55]

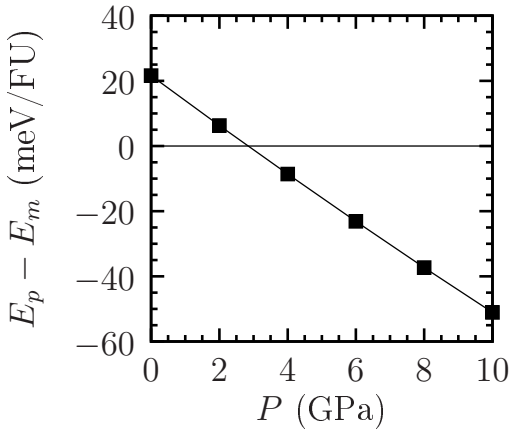

Figure 2-11: Relative stability of pyrite and marcasite as a function of applied pressure within GGA-PBE. The cross-over occurs at 2.8 GPa. To reach the same relative stability predicted by LDA and AM05 ($E_p - E_m = -8.6$ meV/FU), a pressure of 4 GPa is needed.

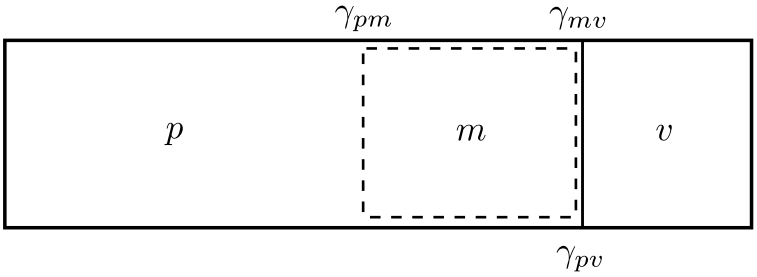

Figure 2-12: Schematic of marcasite overgrowth on pyrite. Pyrite, marcasite, and vacuum are labeled as p, m, and v, respectively. By growing marcasite (enclosed in dashed region), the top bulk layers of pyrite are replaced, resulting in a difference in bulk energy Δg. Moreover, the pyrite (001) surface energy γ_{pv} is replaced with the marcasite (101) surface energy γ_{mv} plus an interfacial energy between the two phases γ_{pm}.

extended for interfacial energies as presented in Sec. 2.3.1.) We match the two phases such that $[101]_m \parallel [100]_p$, and perform integer multiples of 90° rotations of the marcasite phase relative to the pyrite phase about the normal to the interface (which will henceforth be referred to as the z direction), to generate four supercells. We denote the rotation angle as θ. From Fig. 2-3, we see that the pyrite unit cell consists of six monolayers, which can be subdivided into two distinct groups of S–Fe–S layers. The number of S–Fe–S layers along the z direction shall be denoted as N. The six monolayers in a marcasite (101) cell can also be subdivided into two S–Fe–S layers, but they are identical by translational symmetry because the marcasite (101) cell has twice the volume of the marcasite unit cell. Therefore, different pyrite-marcasite interfaces result from N even or odd, for a fixed θ. Figure 2-13 illustrates how the parity of N can generate different pyrite-marcasite interfaces under periodic boundary conditions. In Fig. 2-13(a), octahedra are edge-shared across both interfaces within the supercell. Thus we denote the total interfacial energy by $\gamma_{pm} = 2\gamma_e$, where the subscript e stands for "edge." In Fig. 2-13(b), octahedra are corner-shared at one interface and edge-shared at the other. The total interfacial energy is $\gamma_{pm} = \gamma_e + \gamma_c$, where the subscript c stands for "corner." Calculations are performed for $N = 3, 4, \ldots, 10$.

Figure 2-14 shows that the interfacial energy is indeed dependent on θ and the parity of N. The 0° and 180° configurations are the same, so the energies are exactly identical. Also, notice that the interfacial energy for the 0° and 180° configurations is constant with respect to the parity of N, unlike the 90° and 270° scenarios. The lowest-energy configuration is achieved when N is even and $\theta = 270°$, due to the presence of corner-shared octahedra across the interface. Based on the converged interfacial energies for N even and odd, we obtain that $2\gamma_e = 1.12$ J/m^2 and $\gamma_e + \gamma_c = -0.48$ J/m^2, where γ_e and γ_c are the edge-shared and corner-shared interfacial energies, respectively. By solving these equations we get $\gamma_e = 0.56$ J/m^2 and $\gamma_c = -1.04$ J/m^2.

We remark that the negative interfacial energy is not an artifact, but is due to the strain energy as a result of imposing interfacial coherency. In the energy-balance equation [Eq. (2.4)], the strain energy is included in the Δg term instead:

$$\Delta g = g_m - g_p = [g_m(\epsilon = \epsilon_{\text{ep}}) - g_m(\epsilon = 0)] + [g_m(\epsilon = 0) - g_p]\,. \tag{2.5}$$

Here the energy difference in the first set of brackets is the strain energy for marcasite epitaxial growth on pyrite; ϵ is the strain in the marcasite phase, and ϵ_{ep} represents the epitaxial strain conditions: (i) $a' \equiv \sqrt{a_m^2 + c_m^2} = a_p$, where subscripts m and p denote the marcasite and pyrite phases, respectively; (ii) $b_m = a_p$; (iii) shearing along $[\bar{1}01]$ such that [101] becomes normal to the (101) plane, which is necessary to satisfy periodic boundary conditions. Conditions (i) and (ii) impose lattice mismatches of 3% and 0.1%, respectively, within PBE. (For lattice constants in other functionals, see Sec. 2.5.1.) The third condition is equivalent to setting the c/a ratio to 1, since the angle between the (101) plane and the [101] direction is equal to $\cos^{-1}\frac{(c/a)^2-1}{(c/a)^2+1}$. The energy difference in the second set of brackets is the relative phase stability between pyrite and marcasite. In Sec. 2.5.1, we show that the ground-state phase is functional- and volume-dependent.

Total energies of pyrite and strained marcasite referenced to the strain-free marcasite

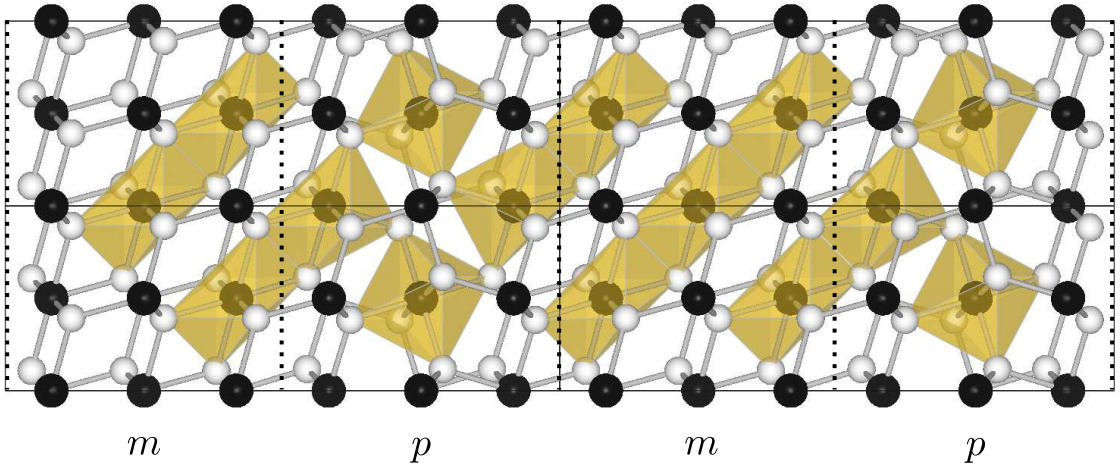

(a)

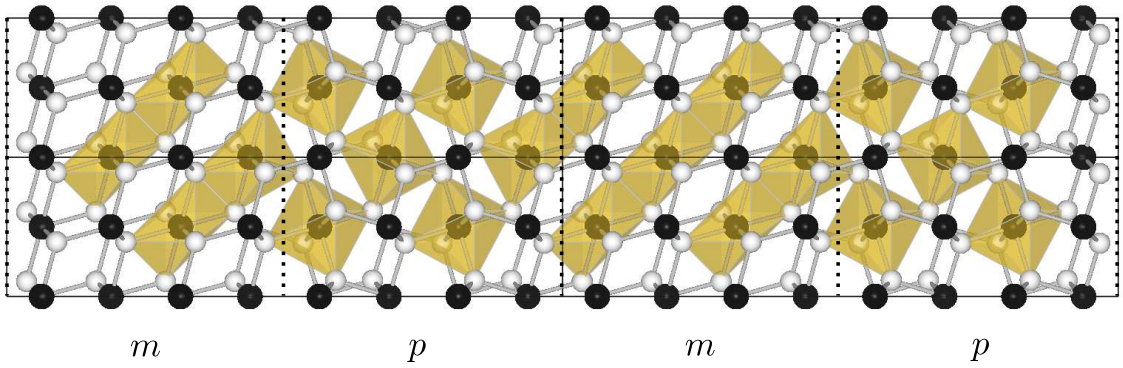

(b)

Figure 2-13: Structures of the pyrite (001)-marcasite (101) interface for $\theta = 270°$ and (a) $N = 3$; (b) $N = 4$. Black (white) spheres are Fe (S) atoms. Pyrite and marcasite phases are labeled by p and m, respectively, where the interfaces are marked by vertical dotted lines. For clarity, the supercell (enclosed in black rectangle) is repeated along the [010] (downward) and [001] (rightward) directions, and octahedra are drawn for Fe atoms in the inner-most layer only. Note the octahedra are edge-sharing in bulk marcasite but corner-sharing in bulk pyrite. At the interface, the octahedra are edge-sharing when N is odd (a), but can be corner-sharing when N is even [from left to right, the second dotted line in (b)], showing that different interfacial energies may result depending on the parity of N. Consecutive 90° rotations of one phase with respect to the other about the rightward axis can create more variations (not shown). It is verified that the corner-sharing type interface with $\theta = 270°$ is the most energetically favorable.

Table 2.4: Bulk energies (in meV/FU) of pyrite (p) and marcasite (m) referenced to the strain-free marcasite total energy. Strain energies of marcasite are calculated under epitaxial and periodic boundary conditions, as discussed in the main text.

Phase	Strain	LDA	PBE	PBE+U	AM05
p	0	−8.4	21.6	26.7	−8.8
m	0	0	0	0	0
m	ϵ_{ep}	898.3	859.8	865.6	896.7

phase are shown in Table 2.4. The magnitude of the difference in the first set of brackets in Eq. (2.5) (marcasite strain energy) is much larger than that in the second set (relative phase stability), for all functionals used. Although different functionals give different predictions for the ground-state phase [sign of $g_m(\epsilon = 0) - g_p$], the strain energy required for epitaxial growth is one order of magnitude higher than the strain-free bulk energy difference [$O(100)$ compared to $O(10)$ meV/FU]. Substituting the PBE bulk, surface, and interfacial energies into Eq. (2.4), we find that the thermodynamic condition for marcasite epitaxial growth is $N < 1.5$, which means that the critical N is only 1 for the corner-sharing-type interface. We also find the same result using other functionals, as the marcasite strain energy is much more significant than the bulk energy difference between strain-free marcasite and pyrite. It is emphasized that the parity of N determines whether the corner-sharing-type interface is present in the supercell under periodic boundary conditions. It does not mean that marcasite can only grow by an even or odd number of layers.

Since the critical N is so small, we cross-validate our prediction via direct computation of pyrite-marcasite-vacuum supercells, as depicted schematically in Fig. 2-12. As the pyrite-marcasite system is separated from its periodic image by a layer of vacuum in the z-direction, there is only one pyrite-marcasite interface here. Calculations are performed for $N = 1, 2, 4, 6, 8$ layers of marcasite on top of pyrite, where the interface is of the corner-sharing type and $\theta = 270°$ (lowest energy configuration). The total energy (per formula unit) is shown in Fig. 2-15. In this direct approach, we find a critical N of 2. The discrepancy between the predicted value of one layer may be attributed to additional ionic relaxation within the marcasite layer to reduce the strain energy, thereby (marginally) enhancing growth. With the qualitative consistency between the two approaches, we have shown that epitaxial growth of marcasite on pyrite is thermodynamically favorable, but only limited to a few layers, as further growth becomes energetically unfavorable.

Although a trace amount of marcasite is predicted to be present, and is indeed observed experimentally [32, 16], whether it really affects the photovoltaic performance of pyrite is a separate issue. Electronic structure calculations of the two phases are presented in the following subsection.

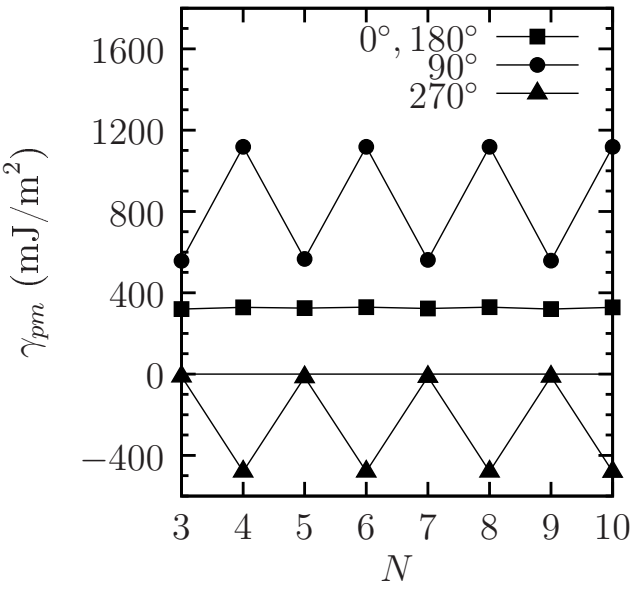

Figure 2-14: The pyrite(001)–marcasite(101) interfacial energy, γ_{pm}, within GGA-PBE. The interfacial energy depends on the relative orientation between the two phases and the parity of N.

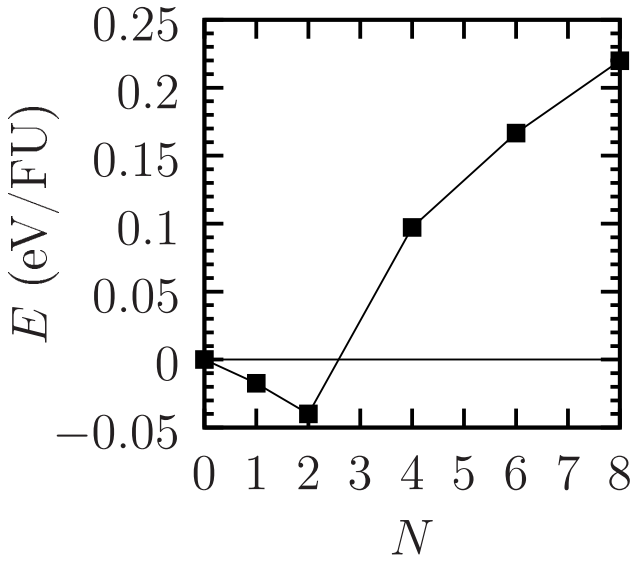

Figure 2-15: Total energy (per formula unit) of pyrite (100)-marcasite (101)-vacuum supercell as a function of the number of epitaxial layers of marcasite, N. The total energies are referenced to a clean pyrite (100) surface ($N = 0$). The global minimum is obtained when $N = 2$.

2.5.4 Difference in bulk band gaps

Whether the presence of marcasite affects the OCV of pyrite depends on (i) the band gaps of the two phases, and (ii) the position of interfacial states. Here we discuss the issue of band gaps (i). Interfacial states (ii) are discussed in Sec. 2.5.5. The PBE band structures of pyrite and marcasite are compared in Fig. 2-16. The band gaps and critical k-points are listed in Table 2.5. For pyrite, the CB edge is located at the Γ point. The VB between 0 and -1.5 eV is very flat, indicating that the states are highly localized, as seen in the DOS in Fig. 2-9. The VB edge is located along the high symmetry Δ line, which connects Γ and X'. However, we note that the direct transition at Γ is only 0.08 eV larger than the indirect gap, in agreement with the experimental difference (1.03 eV for direct transition versus 0.95 eV for indirect transition) [5]. For marcasite, the CB edge is located at (0,0.5,0.5), while the VB edge occurs along the Σ line. Comparing the lowest conduction bands of pyrite and marcasite at the Γ point, the sharp minimum in pyrite is not seen in marcasite. Based on the DOS (Fig. 2-9), the character of the band in pyrite is a S p state, whose presence leads to the CB tail. Such a state is not found in marcasite (Fig. 2-17). Across all functionals that are used (Table 2.5), the Kohn-Sham gap of marcasite is at least comparable to that of pyrite, and significantly higher than the estimate for the experimental gap of 0.34 eV [34].

It is well known that first-principles Kohn-Sham (KS) gap in local and semi-local functionals severely underestimates the band gap. Therefore, we have also calculated the band gaps using two other approaches that have been reported to be more accurate. The hybrid functional Heyd-Scuseria-Ernzerhof (HSE06) [63–66], which has been shown to produce accurate band gaps for solids, gives 2.8 (2.7) eV for pyrite (marcasite). The Δ-sol method, a recently developed total-energy method based on dielectric screening [67], gives 1.3 (1.2) eV for pyrite (marcasite). In both methods, the pyrite and marcasite gaps are almost the same. In the Δ-sol method, the marcasite gap is predicted to be almost 0.9 eV larger than the experimental value [34], although the pyrite gap is only slightly (0.3 eV) larger than the experimental value [5].

2.5.5 Absence of interfacial states within band gap

Apart from the band-gap issue, we also examine the DOS at the pyrite-marcasite interface constructed from the lowest-energy configuration (corner-sharing interface, $\theta = 270°$) to see if interfacial states are present that can pin the Fermi level. The DOS of the $N = 10$ and $\theta = 270°$ pyrite-marcasite interface is shown in Fig. 2-18. Two important observations are made. First, the band gap of the pyrite-marcasite supercell is the minimum of the pyrite and marcasite bulk band gaps. It is not smaller than the pyrite gap. Second, no interfacial states are seen within the band gap. From these results, we conclude that, although marcasite is present at trace amounts under thermodynamic conditions, its electronic structure does not undermine the photovoltaic performance of pyrite.

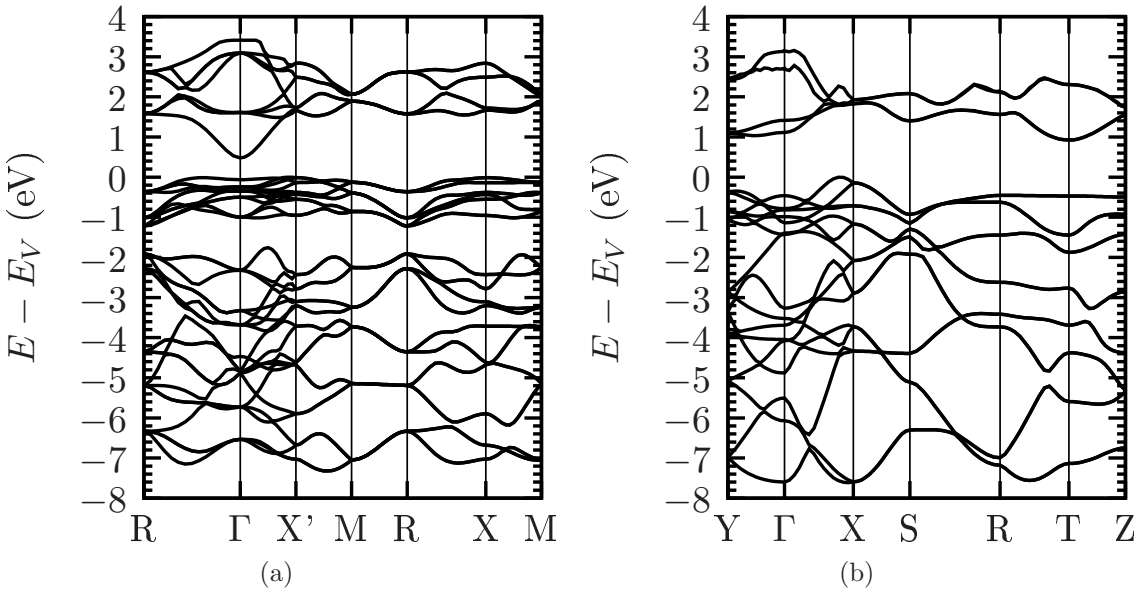

Figure 2-16: PBE band structure of (a) pyrite and (b) marcasite. Both of them are indirect gap materials. High symmetry points correspond to those in Ref. [35]. The LDA and AM05 band structures look very similar and are not shown.

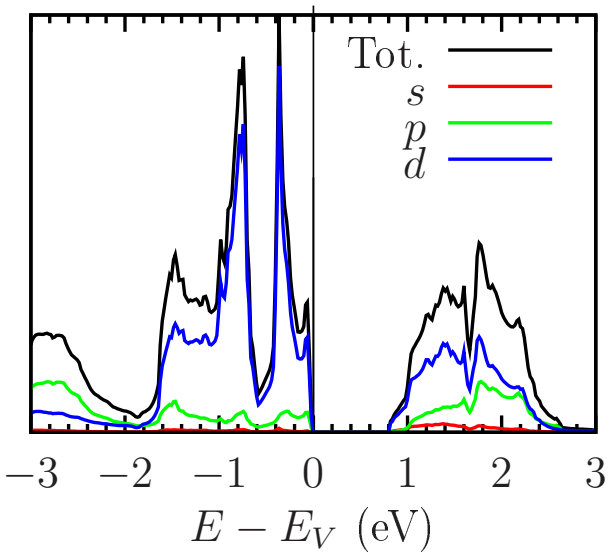

Figure 2-17: DOS of bulk marcasite within GGA-PBE. Contrary to pyrite, there are no pronounced tail states at the CB in marcasite.

Table 2.5: Band gap (in eV) and k-points at VB and CB edges. HSE06 and Δ-sol gaps are obtained at the experimental lattice constants.

	Pyrite			Marcasite		
	E_g	VB	CB	E_g	VB	CB
LDA	0.22	$(0.4375, 0, 0)$	$(0, 0, 0)$	0.88	$(0.375, 0, 0)$	$(0, 0.5, 0.5)$
PBE	0.40	$(0.4375, 0, 0)$	$(0, 0, 0)$	0.81	$(0.4375, 0, 0)$	$(0, 0.5, 0.5)$
PBE+U	1.03	$(0.4375, 0, 0)$	$(0, 0, 0)$	1.18	$(0.4375, 0, 0)$	$(0, 0.5, 0.5)$
AM05	0.29	$(0.4375, 0, 0)$	$(0, 0, 0)$	0.88	$(0.375, 0, 0)$	$(0, 0.5, 0.5)$
AM05+U	0.72	$(0.4375, 0, 0)$	$(0, 0, 0)$	1.18	$(0.375, 0, 0)$	$(0, 0.5, 0.5)$
HSE06	2.76	$(0.5, 0.5, 0)$	$(0, 0, 0)$	2.72	$(0.5, 0, 0)$	$(0, 0.5, 0)$
Δ-sol	1.3	-	-	1.2	-	-
Experiment	0.95[a]	-	-	0.34[b]	-	-

[a] Reference [5].
[b] Reference [34].

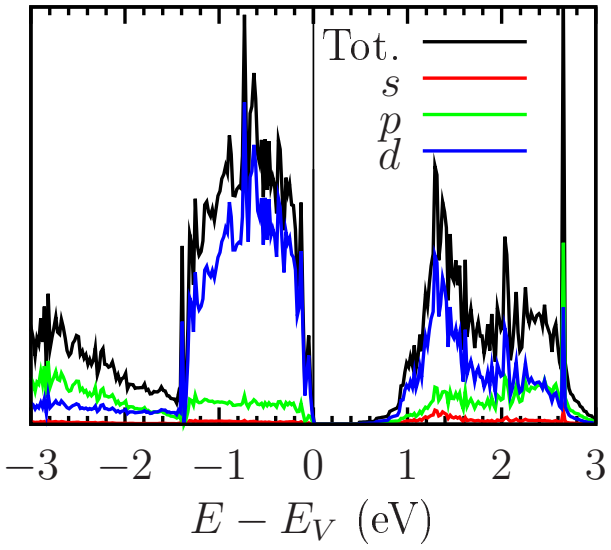

Figure 2-18: DOS of the lowest energy pyrite(001)-marcasite(101) interface (corner-sharing, $\theta = 270°$) within GGA-PBE. By comparing to Fig. 2-9, two key observations are made: (i) the band gap is not reduced; (ii) gap states are not found.

2.6 Discussion

As mentioned in Sec. 2.2.3, the ligand field model of Bronold *et al.* involves an unknown parameter ρ. For Bronold's choice of $\rho = 2$, two gap states are predicted within the gap. However, for $\rho = 1$, the splitting energy between a_1 (d_{z^2}) and b_2 (d_{xy}) states becomes 5.14 Dq [25], or 1.03 eV, which is larger than the experimental band gap of pyrite. This implies that whether the intrinsic surface states are gap states or not depends on the choice of ρ. Our first-principles calculations reveal that the surface states are located near the band edge or deep within the band, with a splitting energy around 1.2 eV within PBE+U [Fig. 2-10(b)], resembling more closely the $\rho = 1$ scenario than the $\rho = 2$ scenario. Hence, the conclusion made by Bronold *et al.* [12] regarding gap states may be unfounded as it is based on an uncontrolled assumption for ρ.

The absence of gap states in the (100) surface of pyrite is confirmed by another first-principles study conducted by Cai and Philpott [15]. Although two other first-principles studies have observed gap states [20,14], their results do not validate the Bronold model. (i) In the study by Oertzen *et al.* [20], the origin of gap states is not due to *intrinsic* surface states, but is due to an additional half monolayer of S atoms on the otherwise properly terminated surface. (ii) In the study by Qiu *et al.* [14], only one type of Fe d gap states is observed, contrary to the prediction of two types of gap states of d_{z^2} and d_{xy} characters by Bronold *et al.* [12]. It should be pointed out that the position of the d_{z^2} surface state is susceptible to errors in the exchange-correlation functional. Although its relative position with respect to the VB has a wide range, being from 0.2 eV in LDA to 1 eV in PBE+U, we find that it remains within the CB across all functionals. Since the Hubbard U model is designed to correct for localized d and f states [68], the fact that the localized d_{z^2} intrinsic surface state is contained above the CBM within PBE+U, as well as the uncorrected LDA, gives strong evidence that it is not a gap state.

Regardless of the apparent discrepancy among first-principles calculations in the literature, surface states may not be relevant under experimental conditions, as the pyrite surface is passivated by adsorbates from the electrolyte. Indeed, the DOS of a passivated pyrite (100) surface shows the depletion of antibonding surface states. This surface passivation effect has been observed by calculations using a monolayer of H-, F-, and Cl-adsorbates on pyrite (100). For example, the PBE DOS of a Cl-adsorbed (100) surface is shown in Fig. 2-19. Compared to the DOS of the clean pyrite (100) surface [Fig. 2-9(b)], the intrinsic surface states at the bottom of the CB are no longer observed. Our results suggest that intrinsic surface states can be passivated. Experimentally, pyrite is often immersed in an aqueous halide (especially the iodide redox couple) in a photoelectrochemical cell, and surface passivation may occur spontaneously [5]. Thus, whether intrinsic surface states are gap states may not pertain to the photovoltaic performance of pyrite at the device level.

From the energy model of marcasite epitaxial growth on pyrite [Eq. (2.4)], with first-principles total energies as input, we find that marcasite growth on pyrite is thermodynamically limited to one layer. This result is validated by direct computation of pyrite-marcasite-vacuum supercells, from which an additional layer of growth is stabilized by further ionic relaxation in the marcasite phase. Qualitatively, our prediction of a few layers of marcasite

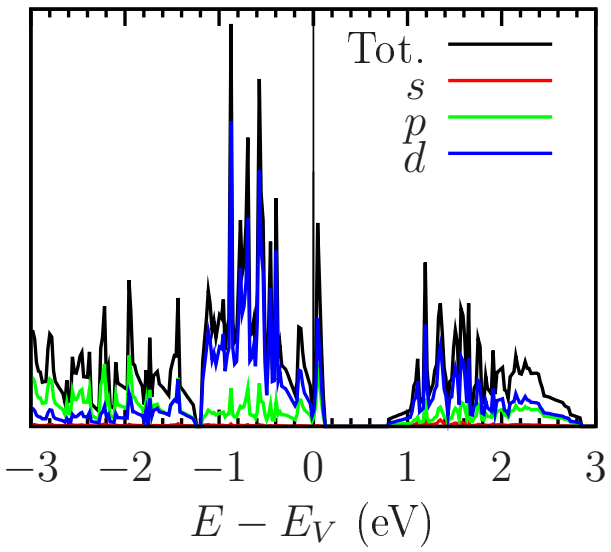

Figure 2-19: DOS of pyrite (100) with Cl-adsorbates. The intrinsic surface state at the CB edge in Fig. 2-9(b) is depleted due to surface passivation.

growth is verified by the experimental observation of a trace amount of marcasite after 46 hours of XRD measuring time for 100 nm samples, but undetectable for thicker samples [32]. As our interfacial energy is well converged, the critical N is independent of the thickness of the pyrite substrate at the scale of the experimental sample. The volume percentage of marcasite in thin 100 nm samples is merely a fraction of 1%. Since our model predicts that the same amount of marcasite should form on the pyrite surface, the volume fraction of marcasite is smaller in thicker pyrite samples, eventually dropping below the threshold for detection.

Although marcasite growth is thermodynamically favorable, the critical question is whether marcasite affects the OCV of pyrite at all. Based on our calculation results, the marcasite Kohn-Sham gap is not smaller than the pyrite gap in any of the functionals that we used. Even though KS gaps of local and semilocal functionals are known to severely underestimate band gaps, the marcasite KS gaps obtained from different functionals are all larger than the reported experimental value, which leads us to suspect that the extraction of the marcasite gap from resistivity measurement [34] may not be an accurate determination of the band gap. As far as the authors are aware, the 0.34 eV marcasite gap is the only value reported and cited in the literature. If the marcasite gap is not smaller, but larger than the pyrite gap, as our result suggests, then its presence does not explain the low OCV of pyrite, contrary to the claim of Wadia *et al.* [16]. We call for a more reliable experimental investigation (e.g., optical measurements) on the marcasite band gap. Moreover, from our interfacial calculations, the gap of pyrite is not reduced in the pyrite-marcasite system, and no gap states are found from the DOS (Fig. 2-18). However, we do not rule out the possibility of the formation of low-energy defect states at the interface. As we have not considered the role of native bulk, interfacial, or extrinsic defects in this study, further investigation is required to understand

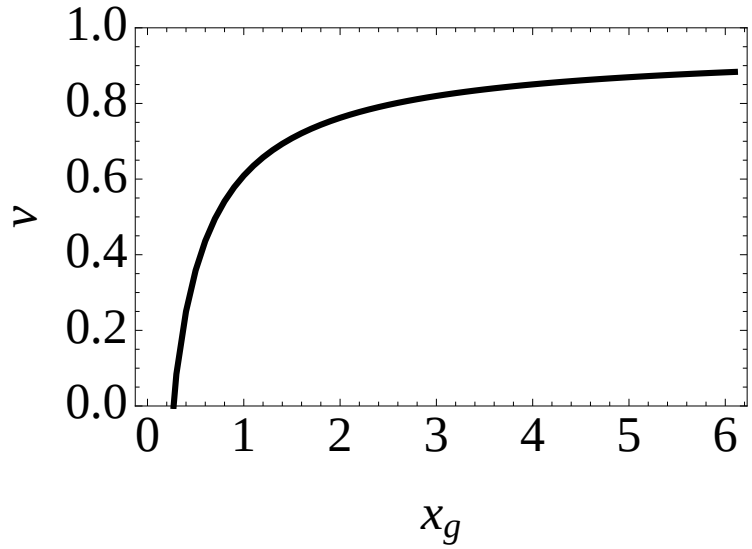

Figure 2-20: Voltage ratio ($v = qV_{oc}/E_g$) as a function of $x_g = E_g/kT_s \approx 1.93E_g$, where $T_s = 6000$ K is the temperature of the sun, predicted by Shockley-Queisser theory [1].

the cause of the low OCV of pyrite.

The theoretical limit in the OCV of any semiconductor can be calculated from the Shockley-Queisser equations [1]. The voltage ratio, defined as $v = qV_{oc}/E_g$, can be expressed analytically as a function of E_g. We plot $v(E_g)$ in Fig. 2-20. For pyrite, then, the theoretical OCV is 0.71 eV, which is more than three times the maximum experimental value of 0.2 eV [5]. In this study, we have established that the low OCV of pyrite cannot be explained by bulk or intrinsic surface properties. Moreover, the formation of marcasite is limited and gap states are not observed from electronic structure calculations of the pyrite-marcasite interface. The low OCV is likely to be caused by effects that we have not yet considered, e.g., defects.

From our band structure calculation, another important issue that may have been overlooked is the low hole mobility of pyrite. Based on the curvature of the DFT band edge [Fig. 2-16(a)], pyrite is predicted to have very heavy holes. The flatness of the VB has previously been reported. For example, the pyrite band structure calculated by linear combination of atomic orbitals (LCAO) can be found in Ref. [35]; a DFT calculation is presented in Ref. [20]. Our first-principles prediction that pyrite has low hole mobility is confirmed experimentally by Oertel *et al.*, who reported $\mu_p < 0.1$ cm^2/(V s) [22]. In light of the strained silicon technology (see, e.g., Ref. [69] and references therein), one possible way to enhance the carrier mobility is to intentionally impose strain on pyrite thin films.

2.7 Conclusions

Using first-principles computations, we have shown that two of the widely accepted reasons for the low open-circuit voltage (OCV) of pyrite photovoltaic devices are questionable. Al-

though Bronold *et al.* have correctly predicted that broken symmetry on the pyrite surface causes intrinsic surface states [12], the character and position are not reproduced within DFT. Firstly, their predicted d_{xy} state is not observed to move out of the VB, and ligand field splitting of the VB is not seen. Secondly, no gap states are found. The only surface-induced state is the d_{z^2} state located at the CB edge, but the d_{xy} state remains within the VB.

Next, we have examined the claim that marcasite reduces the OCV of pyrite. To investigate the thermodynamic condition for the epitaxial growth of marcasite on pyrite, we have derived a parameter-free energy-balance equation [Eq. (2.4)] that involves the bulk, surface, interfacial, and strain energies of the two phases as input. Although a few layers of marcasite growth are predicted to be thermodynamically favorable, by examining the DOS at the pyrite-marcasite interface, no gap states are found. The marcasite gap is at least comparable to the pyrite gap, and significantly greater than the experimental marcasite gap, within all functionals used, suggesting that the experimental resistivity measurement of the marcasite gap [34] may need to be verified by more careful and reliable studies.

Although the direct cause of the low OCV of pyrite photovoltaic devices has not yet been established, we believe that the effects of intrinsic surface states and marcasite are at best secondary. The following chapter will be focused on native and extrinsic defects.

Chapter 3

Intrinsic stoichiometry and oxygen-induced p-type conductivity of pyrite

This is the very perfection of a man, to find out his own imperfections.

St. Augustine

3.1 Introduction

Ever since the first investigation of pyrite FeS_2 as a photovoltaic device [70], a number of challenges have arisen. In this chapter, we focus on the following two open questions that pertain to native defects and extrinsic impurities. (i) Is pyrite off-stoichiometric or is it a line compound? According to the work of Birkholz *et al.*, pyrite samples are sulfur deficient up to 13 at. % [18]. They have suggested that gap states are introduced by sulfur vacancies, though no experimental or theoretical evidence exists to back up this proposal. By reviewing the literature, Ellmer and Höpfner have argued that the compositional variation of pyrite should be within 1 at. %, and that the 13 at. % S-deficiency reported by Birkholz *et al.* is likely to be a measurement error [71]. (ii) Why are synthetic thin films ubiquitously p-type, regardless of the deposition methods and synthesis conditions, although no intentional doping is performed? (See Ref. [22] and references therein, as well as Refs. [72] and [73].) These issues are important if pyrite is ever seriously to be considered as a photovoltaic material.

It is well known that defects can greatly affect the electronic properties of semiconductor devices [74]. Although experiments have alluded to the presence of bulk defects in pyrite [19], and computational [75] and combined experimental-computational [76] work have investigated pyrite surface defects, there has been no systematic study of the role of bulk defects within pyrite in the literature. We address the stoichiometry (i) and unintentional p-type

conductivity (ii) of pyrite via first-principles computation and modeling of native and extrinsic defects. Fe and S vacancies, interstitials, and antisites constitute the native defects. For extrinsic defects, we focus on oxygen interstitial (O_i) and oxygen-on-sulfur substitution (O_S), because oxygen has the highest impurity concentration [$O(10^{19})$ cm^{-3}] in both natural and synthetic samples [5].

In Sec. 3.2 we present the input parameters used in our computations as well as a brief review of defect modeling. In Sec. 3.3 results for native and oxygen defects are presented, followed by a discussion in Sec. 3.4. We demonstrate that pyrite is unlikely to be off-stoichiometric due to the high formation energies of its native defects, and that the p-type conductivity can be attributed to the high concentration of oxygen incorporation on sulfur sites.

3.2 Methods

3.2.1 First-principles computations

Density-functional theory (DFT) [36, 37] calculations within the Perdew-Burke-Ernzerhof (PBE) [45, 46] generalized gradient approximation (GGA) were performed using the plane-wave code Vienna Ab-initio Simulation Package (VASP) [40–43] with projector augmented waves (PAW) potentials [38, 39]. Total energies were converged to within 10^{-7} eV. Charge neutral point defect formation energies were converged for a supercell size of $2 \times 2 \times 2$ with 95–97 atoms. Charged defect total energies were also obtained from $2 \times 2 \times 2$ supercells. All defective supercells were fully relaxed under constant volume with $3 \times 3 \times 3$ Γ-centered Monkhorst-Pack [53] k-points. Forces were converged to within 10^{-4} eV/Å.

3.2.2 Defect modeling

Definitions

We adopt the notation of Persson *et al.* [77] regarding defect computations. Definitions and methodology are briefly summarized as follows. The formation energy of a defect D in charge state q is

$$\begin{aligned}\Delta H_{D,q}(E_F, \mu_\alpha) &= E_{D,q} - E_0 - \sum_\alpha n_\alpha(\mu_\alpha^0 + \Delta\mu_\alpha) + q(E_v + E_F) \\ &= \Delta H_{D,q}^0(\mu_\alpha) + qE_F, \end{aligned} \tag{3.1}$$

where E_0 is the total energy of the perfect host, α is the atomic species of the defect, μ_α^0 is the reference chemical potential, n_α is the number of atoms introduced into (positive) or removed from (negative) the host, E_v is the eigenvalue of the valence band maximum (VBM), E_F is the Fermi level referenced to the VBM, and $\Delta H_{D,q}^0$ is the defect formation energy at the VBM. We have neglected entropy contributions other than configurational entropy since they usually do not affect results qualitatively [78].

It is important to note that the E_F in Eq. (3.1) is merely an energy variable bounded by the position of the band edges. The charge transition level between charge states q and q' of a defect D occurs when their formation energies are the same:

$$\epsilon_{D,q/q'} = \frac{E_{D,q} - E_{D,q'}}{q' - q} - E_v. \tag{3.2}$$

The E_F in Eq. (3.1) is replaced with $\epsilon_{D,q/q'}$ in the derivation.

The concentration of a defect in charge state q is given by

$$c_{D,q}(E_F, \mu_\alpha, T) = N_{\text{site}} \exp\left[-\frac{\Delta H_{D,q}(E_F, \mu_\alpha)}{kT}\right], \tag{3.3}$$

where N_{site} is the concentration of possible defect sites, which is determined by the multiplicity of the defect's Wyckoff position. The total concentration of a certain defect D is obtained by a summation over all the charge states:

$$c_D = \sum_q c_{D,q}. \tag{3.4}$$

The total charge of the system (Q) is the sum of the defect charge concentration (Q_D) and the free carrier concentrations (Q_i):

$$\begin{aligned} Q(E_F) &= \sum_D \sum_q q c_{D,q}(E_F, \mu_\alpha, T) - n + p \\ &= \sum_D \sum_q q N_{\text{site}} \exp\left[-\frac{\Delta H_{D,q}(E_F, \mu_\alpha)}{kT}\right] \\ &\quad - \int_{E_c}^{\infty} f(E; E_F, T) g(E)\, dE + \int_{-\infty}^{E_v} [1 - f(E; E_F, T)] g(E)\, dE, \end{aligned} \tag{3.5}$$

where $g(E)$ is the density of states (DOS) of the host, and $Q_i = p - n$ is the hole concentration (p) in the valence band (VB) minus the electron concentration (n) in the conduction band (CB).

The expected charge state q^* of a defect $\mathrm{X_Y}$ is defined as the difference in valence between X and Y. For example, the expected charge states of $\mathrm{Fe_S}$ and $\mathrm{V_S}$ are $3+$ and $1-$, respectively. Based on the sign of its expected charge state, a defect can be classified as a donor ($q^* > 0$) or an acceptor ($q^* < 0$).

Self-consistent solution for Fermi level and defect concentrations

The thermodynamic Fermi level is the E_F at which charge neutrality is satisfied, i.e., when $Q = 0$ in Eq. (3.5). In solving for the defect concentrations and Fermi level we assume that defects are equilibrated at the synthesis temperature (T_{syn}) and are not modified at room temperature (T_{eq}) due to low diffusion of defects and slow mass exchange with the

environment. Only their charge states can re-equilibrate at room temperature. Procedural details are as follows.

(i) Impose charge neutrality at $T_{\rm syn}$, i.e.,

$$Q_D(E_F^{\rm syn}, T_{\rm syn}) + Q_i(E_F^{\rm syn}, T_{\rm syn}) = 0. \tag{3.6}$$

Solving for $E_F^{\rm syn}$, the concentration of each defect $c_{D,q}$ is found from Eq. (3.3), and the total concentration of each defect c_D is obtained via Eq. (3.4).

(ii) We assume that the total concentration of each defect D is frozen during re-equilibration at $T_{\rm eq}$, i.e.,

$$c_D = c_D(E_F^{\rm syn}, T_{\rm syn}) = c_D(E_F^{\rm eq}, T_{\rm eq}). \tag{3.7}$$

Note that individual $c_{D,q}$'s are not fixed since charge transitions can occur even at room temperature.

(iii) Assume charge transition within a defect type D occurs according to Boltzmann statistics. First, observe from Eqs. (3.1) and (3.3) that one can always express the ratio between the concentration of D in charge state q and that in some arbitrary reference charge state q' as

$$\frac{c_{D,q}}{c_{D,q'}} = \exp\frac{\Delta H^0_{D,q'} - \Delta H^0_{D,q}}{kT} \exp\frac{(q'-q)E_F}{kT}. \tag{3.8}$$

We shall denote the prefactor as

$$A_{D,q} = \exp\frac{\Delta H^0_{D,q'} - \Delta H^0_{D,q}}{kT}. \tag{3.9}$$

By the frozen defect assumption (ii) and using Eq. (3.4), we then obtain

$$c_{D,q}(E_F^{\rm eq}, T_{\rm eq}) = c_D \frac{A_{D,q} \exp\dfrac{-qE_F^{\rm eq}}{kT_{\rm eq}}}{\displaystyle\sum_q A_{D,q} \exp\frac{-qE_F^{\rm eq}}{kT_{\rm eq}}} = c_D \frac{\exp\dfrac{-\Delta H_{D,q}(E_F^{\rm eq})}{kT_{\rm eq}}}{\displaystyle\sum_q \exp\frac{-\Delta H_{D,q}(E_F^{\rm eq})}{kT_{\rm eq}}}, \tag{3.10}$$

which is independent of the reference charge state q'. The above construct allows us to apportion the total defect concentration c_D obtained at $T_{\rm syn}$ to the concentrations of its different charge states $c_{D,q}$ at $T_{\rm eq}$.

(iv) For these fixed defect concentrations c_D, charges are re-equilibrated at $T_{\rm eq}$, i.e.,

$$Q_D(E_F^{\rm eq}, T_{\rm eq}) + Q_i(E_F^{\rm eq}, T_{\rm eq}) = 0, \tag{3.11}$$

where

$$Q_D(E_F^{\rm eq}, T_{\rm eq}) = \sum_D c_D \frac{\sum_q q \exp \frac{-\Delta H_{D,q}(E_F^{\rm eq})}{kT_{\rm eq}}}{\sum_q \exp \frac{-\Delta H_{D,q}(E_F^{\rm eq})}{kT_{\rm eq}}}. \tag{3.12}$$

Thus, having solved for $E_F^{\rm eq}$, all defect concentrations are fully determined by Eq. (3.10), while electron and hole concentrations are given by $n(E_F^{\rm eq}, T_{\rm eq})$ and $p(E_F^{\rm eq}, T_{\rm eq})$, respectively. We choose $T_{\rm syn} = 800$ K and $T_{\rm eq} = 300$ K to simulate synthesis conditions [5].

Reference chemical potentials

The energies of defects that change the stoichiometry of FeS_2 are determined by the chemical potentials of Fe and S in the environment. It is common to evaluate the off-stoichiometric defects at the limits of chemical potentials under which the compound is stable. In this work we simply take limits imposed by stability with respect to the elements:

$$\Delta\mu_{\rm Fe} \leq 0, \tag{3.13}$$

$$\Delta\mu_{\rm S} \leq 0. \tag{3.14}$$

Together with the relation of the chemical potentials to the energy of the compounds:

$$\Delta\mu_{\rm Fe} + 2\Delta\mu_{\rm S} = \Delta H_{\rm FeS_2}, \tag{3.15}$$

the Fe-rich/S-poor and S-rich/Fe-poor limits can be defined.

We investigate oxygen incorporation into the material as a function of the oxygen chemical potential referenced to the most reduced iron oxide phase to form from FeS_2, which is Fe_3O_4 based on our computations within GGA. Specifically, we define

$$\mu_{\rm O}^0 = \frac{1}{4}(\mu_{\rm Fe_3O_4} - 3\mu_{\rm Fe}^0) \tag{3.16}$$

and investigate the Fermi level ($E_F^{\rm eq}$) and oxygen defect (O_S, O_i) concentrations as a function of $\Delta\mu_{\rm O} = \mu_{\rm O} - \mu_{\rm O}^0$, where a positive (negative) sign corresponds to more oxidizing (reducing) conditions. The total oxygen impurity concentration is given by

$$c_{\rm O} = \sum_{D\in\{{\rm O}_i,{\rm O}_S\}} \sum_q c_{D,q}. \tag{3.17}$$

Energy corrections

Three post-DFT corrections are applied. (i) To account for spurious image charge interactions when charged defects are calculated in periodic boundary conditions, we apply the

first-order Makov-Payne correction [79],

$$\Delta E_{D,q}^{\mathrm{MP}} = \frac{q^2 \alpha_M}{2\epsilon a_0}, \tag{3.18}$$

where α_M is the Madelung constant, $\epsilon = 20.6$ is the static dielectric constant we obtain within density-functional perturbation theory (DFPT) [80], and a_0 is the GGA lattice constant of pyrite.

(ii) To correct for the underestimated band gap (Kohn-Sham gap $E_g^{\mathrm{KS}} = 0.4$ eV; see Chapter 2) versus experimental gap $E_g^{\mathrm{expt}} = 0.95$ eV [5]), the conduction band minimum (CBM) and valence band maximum (VBM) of the host DOS are rigidly shifted such that $\Delta E_c - \Delta E_v = \Delta E_g = E_g^{\mathrm{expt}} - E_g^{\mathrm{KS}}$. We determine $\Delta E_v = -0.117$ eV and $\Delta E_c = 0.392$ eV using the Δ-sol method, which is based on screening properties of the perfect host [67].

(iii) As a result of (ii), donor (acceptor) levels are assumed to move with the CBM (VBM) and thus need to be corrected by the corresponding shift in the band edge; specifically [77],

$$\Delta E_{D,q}^{g} = \begin{cases} z_e \Delta E_c & \text{if } D \text{ is a donor} \\ -z_h \Delta E_v & \text{if } D \text{ is an acceptor} \end{cases}, \tag{3.19}$$

where z_e (z_h) is the number of donor electrons (acceptor holes) in the CB (VB). In terms of the expected charge state of a defect D (defined in Sec. 3.2.2), $z_e = q^* - q$ and $z_h = q - q^*$. It follows from this procedure that the location of shallow charge transition levels are fixed relative to the appropriate host band edge upon gap correction. (See Ref. [81] for more discussion.) We remark that formation energies of acceptors are adjusted by $q\Delta E_v$ through Eq. (3.1), in addition to the aforementioned correction. The adjustment applies even when an acceptor D is in its expected charge state q^*, where $z_h = 0$ and $\Delta E_{D,q}^{g} = 0$.

3.3 Results

Results on native defects and oxygen incorporation are presented separately. In Sec. 3.3.1, formation energies of native defects at Fe- and S-rich limits are examined to address whether pyrite is stoichiometric. In Sec. 3.3.2, the role of oxygen point defects are investigated to explain the unintentional p-type conductivity of as-deposited pyrite thin films.

3.3.1 Native defects

The defect formation energy at the Fe-rich limit is plotted as a function of E_F in Fig. 3-1. For each defect, the concave lower envelope of the formation energies for each charge state is drawn to show the lowest-energy charge state along its position within the band gap. The slope of $\Delta H_{D,q}$ is the charge state of D, from Eq. (3.1). Charge transition levels occur at the intersections between different q's, as governed by Eq. (3.2). The minimum and maximum energies on the x-axis correspond to the VBM and the CBM, respectively. The band gap is corrected to match the experimental gap 0.95 eV, as mentioned in Sec. 3.2.2. Near the

VB, the lowest-energy defects are Fe_i and V_S, both carrying positive charges. The concept of defect compensation can be illustrated by the following thought experiment. Suppose E_F^{eq} is drawn toward the VB by some extrinsic acceptor X, then p-type doping becomes increasingly difficult as compensating defects (+) become more and more energetically favorable. Whether a doping limitation is present depends on the actual formation energy of the extrinsic acceptor relative to the minimum formation energy of native compensating defects, which is ~ 2.5 eV in this case. If the acceptor formation energy is much less than 2.5 eV, then $c_{X,-}$ becomes the dominating term in Eq. (3.5), and the Fermi level is expected to shift greatly toward the VB to generate a comparable hole concentration p. In that case, no p-doping limitation would be expected. Likewise, near the CB, the lowest-energy defect is V_{Fe}, whose formation energy is 2.2 eV at the CBM. This suggests that a limitation on n-doping should be about equally unlikely as that on p-doping. We return to this point in Sec. 3.4.

Following the procedure delineated in Sec. 3.2.2, a unique solution E_F^{eq} is found within the gap and marked as a vertical line. Here $E_F^{eq} = 0.567$ eV, which is larger than $E_g/2$ due to the asymmetry of the DOS at the band edges. [A flat tail is found at the CBM but not the VBM; there are more states at the VBM than the CBM (see Chapter 2).] The dominant defects are V_S and Fe_S, with concentrations of $O(10^6)$ cm^{-3}. The equilibrium carrier concentrations in the VB and CB are 1.9×10^{12} cm^{-3} for both holes and electrons, respectively, indicating intrinsic behavior. From Eq. (3.5), since $c_{D,q} \ll n, p$ for all D, the charge neutrality criterion simply becomes $n \approx p$, explaining the intrinsic nature of the material. Since defect concentrations are at most $O(10^6)$ cm^{-3}, pyrite is essentially stoichiometric under these chemical conditions.

At the S-rich limit (Fig. 3-2), the lowest-energy defect is V_{Fe}, with a total concentration of 5.4×10^{14} cm^{-3}. The defect formation energy of V_S is about 0.8 eV higher than that in the Fe-rich limit, resulting in negligible concentrations. Compared to V_{Fe}, the formation energies of all other defects in the S-rich limit are at least 1 eV larger; thus, they do not play an important role.

The degree of off-stoichiometry of pyrite, or any compound, can be directly predicted by the equilibrium concentration of its native defects. In principle, the off-stoichiometry should be calculated at the chemical potential reference corresponding to experimental conditions. Although the exact reference is unknown, the defect energetics and hence the physics of the system are bounded between the Fe- and S-rich limits. By inspection of Eq. (3.1), defect formation energies at any allowable chemical potential reference can be obtained by linear interpolation between the two limits. From our results as presented above, the concentration of off-stoichiometric defects is at most on the order of 10^{14} cm^{-3}. Moreover, we believe that reference chemical potentials at experimental conditions should lean toward the Fe-rich limit for the following reasons. (i) The unresolved issue is whether pyrite is S deficient [18,71], which is more likely to occur under Fe-rich conditions than S-rich conditions. (ii) Fe deficiency due to V_{Fe} has not been reported, implying the environment is Fe rich. (iii) A common method employed to synthesize pyrite is the sulfurization of Fe metal [6], which corresponds to the Fe-rich limit. At the Fe-rich limit, defect concentrations are merely

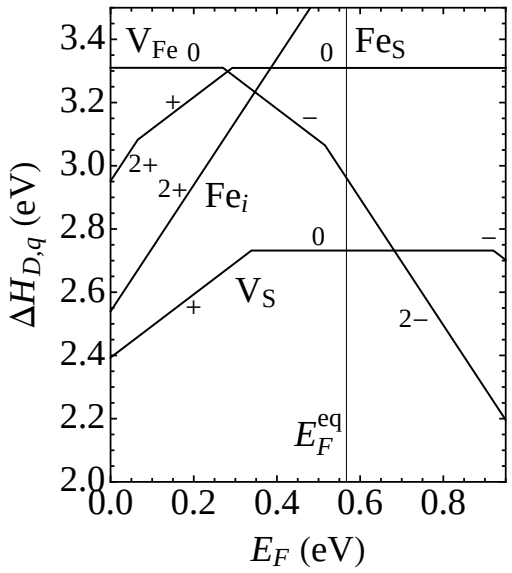

Figure 3-1: Defect formation energy as a function of E_F at the Fe-rich limit, where $E_F^{eq} = 0.567$ eV.

$O(10^6)$ cm^{-3}. Therefore, pyrite should be stoichiometric when pure. Even at the S-rich limit, it would remain essentially stoichiometric, where an Fe deficiency of 10^{-8} per formula unit is predicted.

3.3.2 Oxygen as an acceptor

Oxygen is a common species in the environment and often present in many materials, even if the composition would not indicate so. For example, it forms a detrimental deep state in AlGaN [78] and occurs in high concentrations in both as-deposited Si [82] and FeS_2 [5]. We have investigated the possibility of oxygen incorporation into pyrite under reasonable oxidation conditions by calculating the formation energies of the oxygen-on-sulfur substitutional point defect (O_S) and oxygen interstitial (O_i). Using these energies, and together with the formation energies of native defects as calculated in Sec. 3.3.1, we solve for the Fermi level and defect concentrations by the same procedure in Sec. 3.2.2 across a range of $\Delta\mu_O$ as defined in Sec. 3.2.2. Results at the Fe-rich limit, for reasons discussed at the end of Sec. 3.3.1, are presented. Note that, at the S-rich limit, μ_O^0 can be higher [Eq. (3.16)].

In Fig. 3-3 the Fermi level is plotted as a function of $\Delta\mu_O$. The bottom-most and topmost energies on the y-axis correspond to the VBM and CBM, respectively. Under highly reducing conditions at $T_{syn} = 800$ K, the equilibrium Fermi level remains at the intrinsic level (0.567 eV in Fig. 3-1). At higher oxidation environments and higher temperature the Fermi level moves toward the VB. A Fermi level below (above) the intrinsic 0.567-eV value indicates that the system is p-type (n-type). Clearly, under more oxidizing conditions, pyrite becomes increasingly p-type.

The corresponding total oxygen impurity concentration is shown in Fig. 3-4. The parts-per-billion (ppb) and parts-per-million (ppm) oxygen concentrations correspond to $\Delta\mu_O$'s of

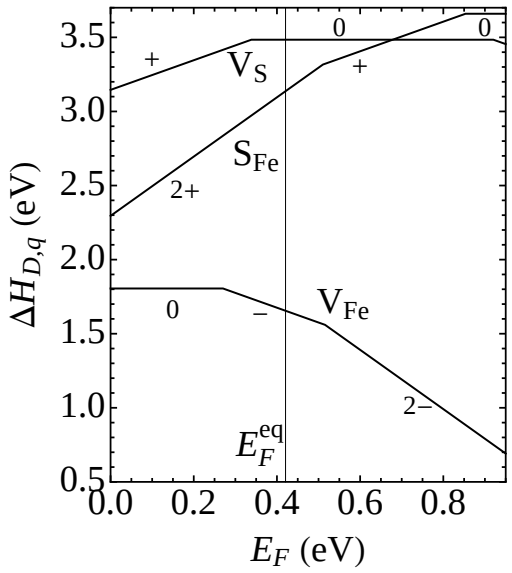

Figure 3-2: Defect formation energy as a function of E_F at the S-rich limit, where $E_F^{\text{eq}} = 0.421$ eV.

about -0.3 and 0.1 eV, respectively. For $\mu_{\text{O}} < -0.5$ eV, oxygen incorporation is negligible compared to native defect concentrations. The exponential increase in c_{O} as a function of $\Delta\mu_{\text{O}}$ is expected by inspection of Eqs. (3.1) and (3.3). For $\Delta\mu_{\text{O}} > 1$ eV, all sulfur atoms in pyrite are essentially substituted by oxygen. We find that the experimental oxygen concentration ($\sim 10^{19}$ cm^{-3}) is reached for $\Delta\mu_{\text{O}} \approx 0.6$ eV. The system is examined in detail at this chemical potential.

In Fig. 3-5 we show the defect formation energies at $\Delta\mu_{\text{O}} = 0.6$ eV. Since the oxygen chemical potential does not enter into the charge transition levels of native defects [Eq. (3.2)], the ΔH lines of native defects are not affected by the presence of oxygen. While O_i is highly unfavorable (formation energy 3.1 eV), O_{S} is the most energetically favorable defect within the system. The Fermi level is pulled down from the intrinsic value 0.567 to 0.458 eV. Although the change in the Fermi level induced by oxygen alters $\Delta H_{D,q}(E_F^{\text{eq}})$ for native defects, their energies are still too high compared with $\Delta H_{\text{O}_{\text{S}}}$ (Table 3.1). Hence, the lowering of the Fermi level is solely caused by O_{S}.

In Figs. 3-3 and 3-4 we also compute the Fermi level and oxygen concentration at $T_{\text{syn}} = 300$ K. The Fermi level is not perturbed until $\Delta\mu_{\text{O}} \approx 0.7$ eV. The onset of the Fermi level drop at both temperatures in Fig. 3-3 corresponds to the same $c_{\text{O}} \approx 10^{15}$ cm^{-3} in Fig. 3-4.

3.4 Discussion

Within the Fe- and S-rich limits, concentrations of native defects are low due to their high formation energies. Intrinsically, pure pyrite is expected to be stoichiometric. Off-stoichiometric experimental samples may be attributed to the presence of other phases with lower S content, e.g., pyrrhotite Fe_{1-x}S. Ellmer and Höpfner [71] have calculated the formation energies

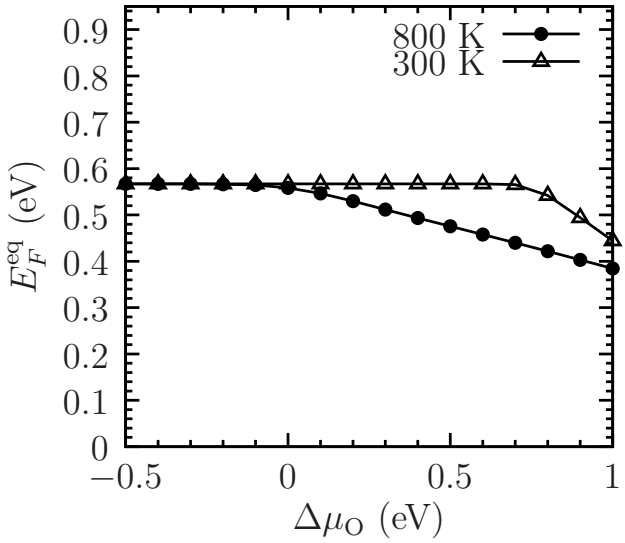

Figure 3-3: Equilibrium Fermi level as a function of $\Delta\mu_{\rm O}$ under $T_{\rm syn} = 800$ K (black circles) and $T_{\rm syn} = 300$ K (open triangles). Pyrite becomes increasingly p-type as the environment becomes more oxidizing.

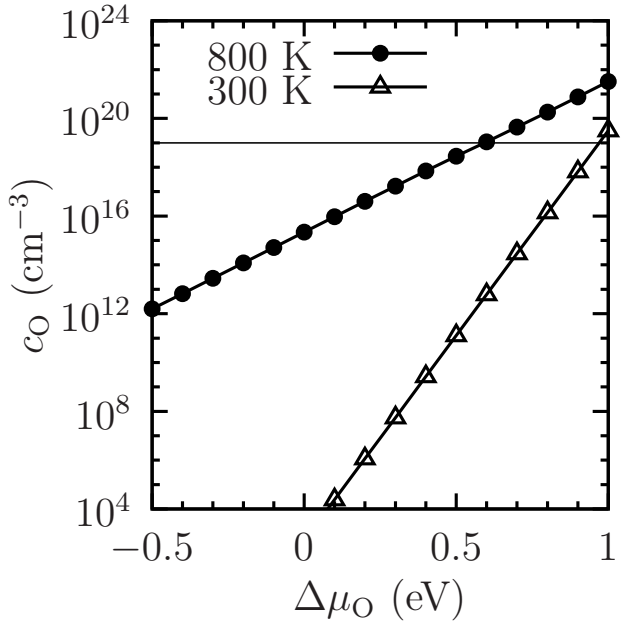

Figure 3-4: a
s a function of $\Delta\mu_{\rm O}$ under $T_{\rm syn} = 800$ K (solid circles) and $T_{\rm syn} = 300$ K (open triangles).]Oxygen impurity concentration ($c_{\rm O}$ defined in Eq. (3.17)) as a function of $\Delta\mu_{\rm O}$ under $T_{\rm syn} = 800$ K (black circles) and $T_{\rm syn} = 300$ K (open triangles). The experimental concentration (10^{19} cm^{-3}) corresponds to $\Delta\mu_{\rm O} = 0.6$ eV. The concentration of oxygen impurities increases exponentially as the environment becomes more oxidizing. For $\Delta\mu_{\rm O} > 1$ eV, essentially all sulfur sites are occupied by oxygen.

Table 3.1: Defect formation energies and concentrations of O_S under Fe-rich environment and $\Delta\mu_O = 0.6$ eV. It can be verified that $\sum_q c_{D,q}(E_F^{eq}) = \sum_q c_{D,q}(E_F^{syn})$, as required by the frozen defect assumption in Sec. 3.2.2. Energies (concentrations) of other defects are too high (low) and are not shown.

q	$\Delta H^0_{D,q}$ (eV)	$\Delta H_{D,q}(E_F^{eq})$ (eV)	$c_{D,q}(E_F^{syn})$ (cm^{-3})	$c_{D,q}(E_F^{eq})$ (cm^{-3})
2+	1.19	2.10	2.82×10^{7}	4.49×10^{-7}
1+	0.78	1.24	8.08×10^{13}	1.54×10^{8}
0	0.59	0.59	9.65×10^{18}	1.10×10^{19}
1−	1.34	0.88	1.39×10^{18}	1.30×10^{14}
2−	2.42	1.51	1.67×10^{15}	4.42×10^{3}

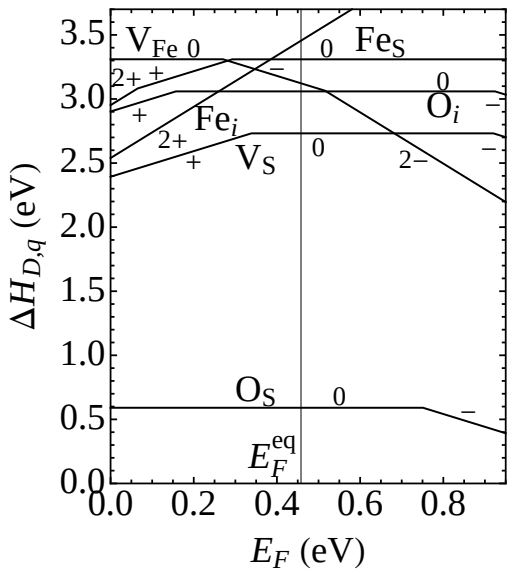

Figure 3-5: Defect formation energy as a function of E_F at the Fe-rich limit and $\Delta\mu_O = 0.6$ eV, where $E_F^{eq} = 0.458$ eV. Formation energy lines of native defects are identical to those in Fig. 3-1.

of S and Fe vacancies using the macroscopic cavity model [83]. Although their energies are systematically lower (1.66 and 2.18 eV, respectively) [71] than our calculations (2.73 and 2.96 eV, respectively), we agree qualitatively that these native defects are energetically unfavorable and do not cause noticeable off-stoichiometry in FeS_2. Our study provides a first-principles basis for the high formation energy of native defects within the material.

From Fig. 3-2 intrinsic p-type conductivity of pyrite is predicted at the S-rich limit. The most energetically favorable defect is V_{Fe}^{-}, with a concentration of 5.2×10^{14} cm^{-3}. The hole concentration is almost the same (5.5×10^{14} cm^{-3}), as expected by Eq. (3.11). However, since the experimental condition is expected to be Fe-rich, as discussed in Sec. 3.3.1, the p-type conductivity should not be attributed to the Fe vacancy. Because oxygen is experimentally measured to have the highest impurity concentration in both synthetic and natural samples [5], we have examined the role of oxygen impurities.

The experimental oxygen impurity concentration, $O(10^{19})$ cm^{-3}, is reached when $\Delta\mu_O = 0.6$ eV. From Table 3.1, the most dominant defects are O_S^0 (1.1×10^{19} cm^{-3}) and O_S^- (1.30×10^{14} cm^{-3}). Since the oxidation state of S is -1 in pyrite [23], O_S is expected to be an acceptor with charge state $q^* = 1-$. The prevalence of the charge-neutral defect is very unusual, which at first sight may suggest the formation of an anomalous peroxysulfide bond $[O–S]^{2-}$. To investigate the nature of O_S^0, we show in Fig. 3-6 the charge density difference between the supercell with a charge-neutral O_S defect and the perfect host, with an isosurface of ± 0.0155 $e/Å^3$. Negative charge is drawn to O from the neighboring S and Fe atoms. Thus, the oxygen defect is stabilized by partial oxidation of its nearest neighbors, and there is no anomalous bond formation. Likewise, we have also examined the charge density difference between supercells with O_S^0 and O_S^- defects (not shown). There is no difference observed around the O_S defect. Instead, negative charge is attracted to each of the neighboring Fe atoms. Hence, the Fe_n–O_S defect complex is essentially an O^{2-} on a S site with charge state variability accommodated on the neighboring Fe atoms. By Table 3.1 and Eq. (3.11), then, an effective hole carrier concentration of 1.1×10^{19} cm^{-3} is predicted. From experimental Hall measurements of pyrite (without intentional doping) conducted by Willeke *et al.*, the hole concentration is 5×10^{18} cm^{-3} [62]. The remarkable agreement in the hole concentration between our calculation and experiment, together with the high oxygen impurity concentration [5], gives strong evidence that the p-type conductivity of pyrite is oxygen-induced.

We draw an analogy between this work and Van de Walle and Neugebauer's work on AlGaN, in which they show that unintentional n-type conductivity is not caused by V_N, as its formation energy is too high, but is caused by oxygen contamination [78]. While the substitutional O atom in AlGaN causes significant lattice relaxation around the impurity [84], it is essentially located at the S site in pyrite. The presence of O_S will undermine device performance by serving as a Shockley-Read-Hall recombination center. Indeed, since the 0 and $1-$ charge states are the most energetically favorable defects within the system, the O_S

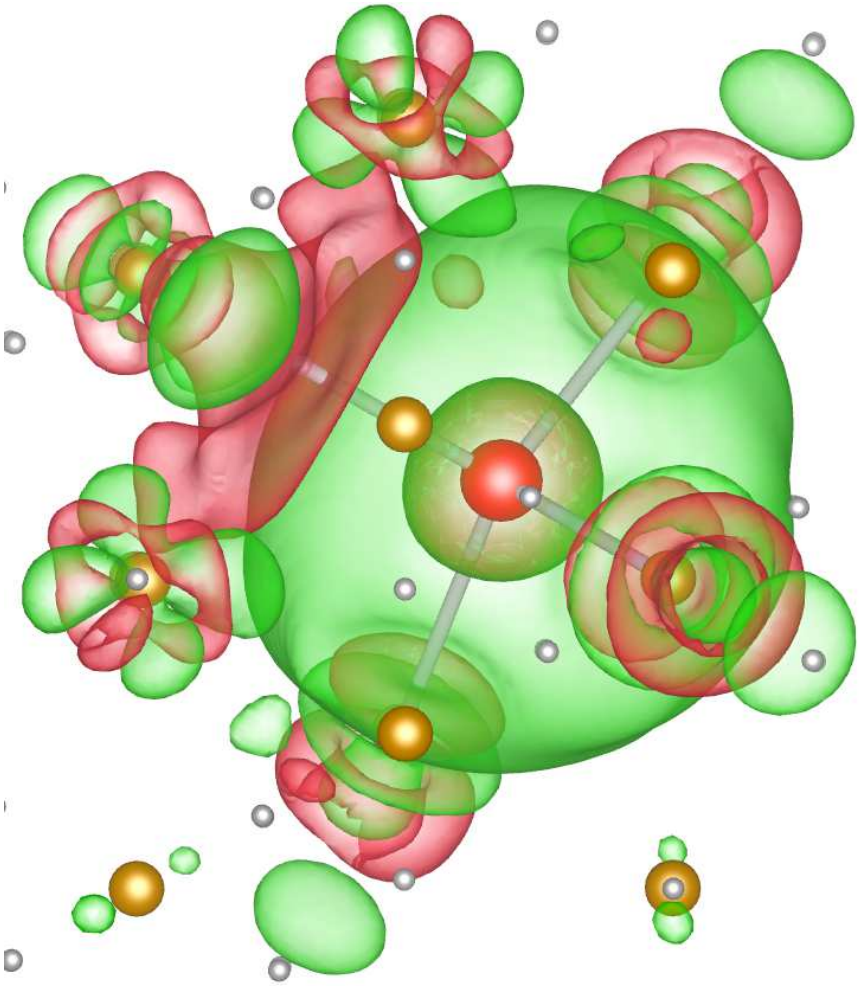

Figure 3-6: Charge density difference (rendered by VESTA [24]) between a supercell with an O_S^0 defect and the perfect FeS_2 host, viewed in the (111) plane. Positive and negative 0.0155 $e/\text{Å}^3$ charge density isosurfaces are drawn in red and green, respectively. The O_S defect (red) is located within a tetrahedral environment of one S (gray) atom and three Fe (brown) atoms. The charge state of O_S is effectively 1− due to charge transfer from its nearest neighbors, as discussed in the text.

defect can trap both mobile electrons and holes:

$$\mathrm{O_S^0} + e^- \rightarrow \mathrm{O_S^-}, \tag{3.20}$$

$$\mathrm{O_S^-} + h^+ \rightarrow \mathrm{O_S^0}. \tag{3.21}$$

In the electron trapping mechanism [Eq. (3.20)], the electron is not trapped by the O atom, but by its partially oxidized nearest neighbors within the Fe_n–$\mathrm{O_S}$ defect complex, as discussed earlier.

It is clear from Figs. 3-3 and 3-4 that oxygen incorporation can be reduced by either lowering the temperature or synthesizing under more reducing environments. For example, to reduce c_O to 1 ppm ($\sim 10^{16}$ cm^{-3}) at $T_\mathrm{syn} = 800$ K, $\Delta\mu_\mathrm{O}$ should be decreased to 0.1 eV. Since

$$\delta\Delta\mu_\mathrm{O} = kT_\mathrm{syn} \ln \frac{p_{\mathrm{O}_2}}{p^0_{\mathrm{O}_2}}, \tag{3.22}$$

the oxygen partial pressure must be reduced by a factor of 1000 with respect to existing experimental conditions. In the case of as-deposited Si, O contamination occurs on the order of 10^{19}–10^{21} cm^{-3}, causing unwanted n-type behavior [82]. Torres *et al.* have shown that even a mere reduction of oxygen incorporation by 2 orders of magnitude improves device performance [82]. We believe that the performance of pyrite photovoltaic devices can be similarly enhanced by lowering the concentration of oxygen impurities.

Returning to the dopability implication in Sec. 3.3.1, we do not expect any n- or p-doping limitations. The formation energies of native defects lie well above 0 in all allowable chemical potential and Fermi level ranges (Figs. 3-1 and 3-2), negating the possibility of Fermi level pinning by native defects. (Fermi level pinning is the position of the Fermi level at which the formation energy of a compensating defect becomes 0 [77].) Indeed, pyrite can be doped n-type by elements such as Co [22, 85] and Ni [85], with carrier concentrations as high as 10^{20} cm^{-3} [22]; intentional p-type doping by P has also been achieved [86]. Since device measurements are made on pyrite photoelectrochemical cells instead of p-n junctions [5], poor performance cannot be attributed to a limited dopability. The more plausible bottleneck is oxygen contamination, which not only behaves as a trap for mobile carriers, but also explains the ubiquitous observation of unintentional p-type conductivity. Future experiments that seek to improve device performance may investigate along these lines.

3.5 Conclusions

On the basis of the first-principles modeling of the point defects in pyrite presented in this work, we find that native defects have high formation energies, and that their equilibrium concentrations are too low for pure pyrite to be off-stoichiometric. The presence of oxygen impurities leads to a drop in the Fermi level toward the VB. This unintentional p-type doping effect is more prominent as the environment becomes more oxidizing. At higher temperatures, the onset of such an effect occurs under more reducing conditions. At the experimental oxygen impurity concentration, we predict a hole concentration of $O(10^{19})$ cm^{-3},

in agreement with experimental Hall measurements [62]. Therefore, the unintentional p-type conductivity of synthetic pyrite thin films can be explained via the presence of O_S, which may act as a Shockely-Read-Hall recombination center. To improve device performance, the current parts-per-thousand oxygen impurity concentration [5] must be significantly reduced.

Chapter 4

Feasibility of pyrite band gap engineering

I have not failed. I've just found 10,000 ways that won't work.

Thomas A. Edison

4.1 Introduction

Being almost 0.5 eV less than the optimum band gap (1.4 eV) within Shockley-Queisser theory [1], the band gap of pyrite FeS_2 ($E_g^{\text{expt}} = 0.95$ eV; see Ref. [5]) is suboptimal for single-junction photovoltaic applications, and it is of interest to understand to what extent this gap can be modified. Following our studies on the bulk, surface, interfacial (Chapter 2), and point defect properties (Chapter 3) of pyrite, we investigate in this chapter whether the long-standing problem of its low open-circuit voltage (OCV) can be mediated by band gap engineering.

It is common practice to tune the electronic properties of semiconductors by alloying [87, 88]. The idea of alloying pyrite with a higher-gap material to enhance the low OCV is first mentioned in the work of Altermatt *et al.*, in which the incorporation of Zn is suggested as a target for future work [89]. Although the band gap of ZnS_2 has not been experimentally determined, it is estimated to be 2.5 eV [35]. Other known isostructural disulfides include MnS_2, CoS_2, NiS_2, CuS_2, RuS_2, and OsS_2. (See Ref. [5] and references therein.) Among these materials, MnS_2 [5], CoS_2, and CuS_2 are metallic [90], and NiS_2 has a smaller band gap than pyrite [5], making them of little interest to increase the band gap of pyrite. This leaves ZnS_2, RuS_2 ($E_g^{\text{expt}} = 1.3$ eV; Ref. [5]), and OsS_2 ($E_g^{\text{expt}} = 2.0$ eV; Ref. [5]) as remaining candidates.

Solid solutions of various isostructural pyrite materials, e.g., $(Fe, Co)S_2$, $(Fe, Ni)S_2$, and $(Fe, Cu)S_2$, have been synthesized [91, 92], though their band gaps have not been evaluated.

Elements that do not form the pyrite crystal structure with S can, in principle, also be used as alloying additions to FeS_2, although in many cases their enthalpy of mixing is large.

In the remaining sections, we first describe the computational techniques in Sec. 4.2.1, the analysis framework in Sec. 4.2.2, and the materials screening procedure in Sec. 4.2.3. Results for alloying pyrite with elements that form (do not form) the pyrite crystal structure are shown in Sec. 4.3.1 (Sec. 4.3.2). In Sec. 4.4, we discuss our findings and show correlations between electronegativity difference, size difference, band gap bowing, and miscibility.

4.2 Methods

4.2.1 Computational details

Density-functional theory (DFT) [36, 37] calculations within the Perdew-Burke-Ernzerhof (PBE) [45, 46] generalized gradient approximation (GGA) were performed using the plane-wave code Vienna Ab-initio Simulation Package (VASP) [40–43] with projector augmented wave (PAW) potentials [38,39]. Total energies were converged to within 10^{-6} and 10^{-4} eV for each self-consistent loop and ionic relaxation step, respectively, using an $8\times8\times8$ Monkhorst-Pack [53] grid of k-points. For each mixture, the calculated equilibrium lattice constant (a_0), the bulk modulus (B), and the pressure derivative of the bulk modulus (B') were obtained by fitting the total energy of the relaxed structure at different volumes to the Murnaghan equation of state (EOS) [93]:

$$E(V) = E(V_0) + \frac{BV}{B'}\left[\frac{(V_0/V)^{B'}}{B'-1}+1\right] - \frac{BV_0}{B'-1}, \tag{4.1}$$

where V_0 is the equilibrium volume.

The band gap was obtained using the Δ-sol method [67] with an $8\times8\times8$ Γ-centered mesh of k-points:

$$E_g = \frac{E(N_0+n)+E(N_0-n)-2E(N_0)}{n}, \tag{4.2}$$

where N_0 is the number of valence electrons in the original $(Fe,M)S_2$ unit cell, $n = N_0/N^*$, $N^* = 72$, and total energies $E(N_0)$ and $E(N_0\pm n)$ were calculated at the experimental lattice constants whenever known, as recommended in Ref. [67]. For mixtures of compounds whose experimental lattice constant is known for both end members in the pyrite structure, the gap of the mixture was calculated at the lattice constant linearly interpolated between the end members. For other mixtures where this information is not available, the calculated lattice constant was used. It is important to note that we do not use DFT band gaps calculated with local and semilocal functionals for screening, since they underestimate the band gap. On the other hand, it has been demonstrated in Ref. [67] that the band gap error in the Δ-sol method is only $O(0.1)$ eV, on par with results from the hybrid functional HSE06 [63, 64], but the computational cost of Δ-sol is similar to a typical DFT calculation, making it the method of choice for high-throughput band gap screening.

We used 12-atom unit cells in all calculations. Band structures were computed as described in Chapter 2.

4.2.2 Analysis framework

We fit the lattice constant, bulk modulus, and band gap of the $Fe_xM_{1-x}S_2$ pseudobinary mixtures with a quadratic function of the concentration x:

$$P(x) = (1-x)P(0) + xP(1) - b_P\ x(1-x), \tag{4.3}$$

where P is the relevant property and b_P is its bowing parameter. The bowing parameters b_a, b_B, and b_g were obtained by fitting the lattice constant, bulk modulus, and band gap of $Fe_xM_{1-x}S_2$, for $x = 0, 0.25, 0.5, 0.75, 1$, respectively. In particular, if $b_a \approx 0$ then the alloy obeys Vegard's rule.

To obtain information on the miscibility of FeS_2 with the MS_2 alloying compound, the critical temperature at the top of the miscibility gap (T_c) was estimated as

$$T_c = \frac{\Omega}{2k_B}, \tag{4.4}$$

where Ω is the regular solution interaction parameter fitted to the calculated energies of mixing. Since the mixing enthalpy in the regular solution model is quadratic in concentration, Ω can also be viewed as the (negative of the) bowing parameter of $\Delta H(x)$.

Solutions can often be created in epitaxial conditions. To investigate this possibility, we used the model of Ipatova *et al.*, who showed that, for a pseudobinary semiconductor film coherently grown on a lattice-matched substrate, the critical temperature for the spinodal instability at $x = 0.5$ is [94]

$$T_c^* = \frac{1}{2R}\left\{\Omega - \frac{(c_{11}-c_{12})(c_{11}+2c_{12})}{2(c_{11}+c_{12})}V_m\left[\frac{a(1)-a(0)}{a(0.5)}\right]^2\right\}, \tag{4.5}$$

where R is the gas constant, V_m is the molar volume, c_{ij}'s are elastic constants at $x = 0.5$ in Voigt notation, and the $a(x)$'s are the lattice constants at the corresponding concentrations. The elastic constants c_{11} and c_{12} in Eq. (4.5) were calculated by applying lattice distortions following Mehl [95]. It can be easily shown that, in cubic systems, the total strain energy associated with the applied strain

$$\epsilon_{ij} = \begin{pmatrix} \delta & 0 & 0 \\ 0 & -\delta & 0 \\ 0 & 0 & \delta^2/(1-\delta^2) \end{pmatrix} \tag{4.6}$$

takes the form

$$\Delta E = (c_{11}-c_{12})V\delta^2 + O(\delta^4), \tag{4.7}$$

where ΔE is the total energy referenced to the unstrained system. Total energies were cal-

culated at $\delta a_0 = 0, 0.2, 0.4, 0.6$ Å. Using the bulk modulus determined from the Murnaghan EOS [Eq. (4.1)] and the fact that $B = (c_{11} + 2c_{12})/3$ within linear elasticity, the elastic constants c_{11} and c_{12} were obtained and substituted into Eq. (4.5) to calculate T_c^*.

4.2.3 Screening procedure

For all known candidate compounds that are isostructural to FeS_2, only those that have a higher experimental gap (Zn, Ru, Os) were studied. Among elements that do not form the pyrite structure with S, we considered all isovalent metals, transition metals, and semiconductor elements up to group IV and period 6 in the periodic table as possible alloying additions. Non-isovalent materials were not considered since disulfides of cations that are not 2+ would not be charge compensated, thus moving the Fermi level into the conduction or valence band of FeS_2. Rare-earths were excluded from the screening procedure as their usage would reduce the potential economic competitiveness of pyrite [7] in large-scale photovoltaic applications. For each possible alloying element M, the band gap of the disulfide MS_2 in the (hypothetical) pyrite crystal structure was calculated using the Δ-sol method as described in Sec. 4.2.1. Materials that have a smaller gap were eliminated. The band gaps and formation energies at $x = 0.25, 0.5, 0.75$ were calculated for the remaining candidates.

A successful alloying material must meet the following criteria: (i) the band gap bowing parameter should be small (or negative) to increase the gap with as little alloying element as possible; (ii) the regular solution interaction parameter should be small to ensure miscibility; and (iii) the material should not be expensive.

4.3 Results

4.3.1 Elements that form pyrite structure with S: Zn, Ru, Os

The Murnaghan EOS is calculated at each composition (not shown) to give the computed lattice constant and bulk modulus. Figure 4-1 shows the lattice constant as a function of composition x. While the lattice parameter mostly obeys Vegard's law, the bulk modulus does not interpolate linearly with composition (Fig. 4-2). The bowing parameter b_B is on the order of 10 GPa.

As stressed in Ref. [67], it is important to calculate the band gap at the experimental lattice parameter rather than the computationally optimized lattice constant. Since the experimental lattice constants at intermediate compositions for these $(Fe, M)S_2$ systems are unknown, they must be interpolated from the end members. Based on the finding that the bowing parameter b_a is negligible [$O(0.01)$ Å; Fig. 4-1], we simply perform a linear interpolation between the experimental lattice constant for intermediate values of x (Table 4.1). The calculated band gaps of $(Fe, M)S_2$ are shown in Fig. 4-3 for M=Zn, Ru, Os. For Zn alloying, there is a considerable amount of band bowing ($b_g = 3.3$ eV), making it ineffective to increase the gap of FeS_2. Ru and Os seem to be favorable alloying additions, as the band gap increases monotonically with the solute concentration.

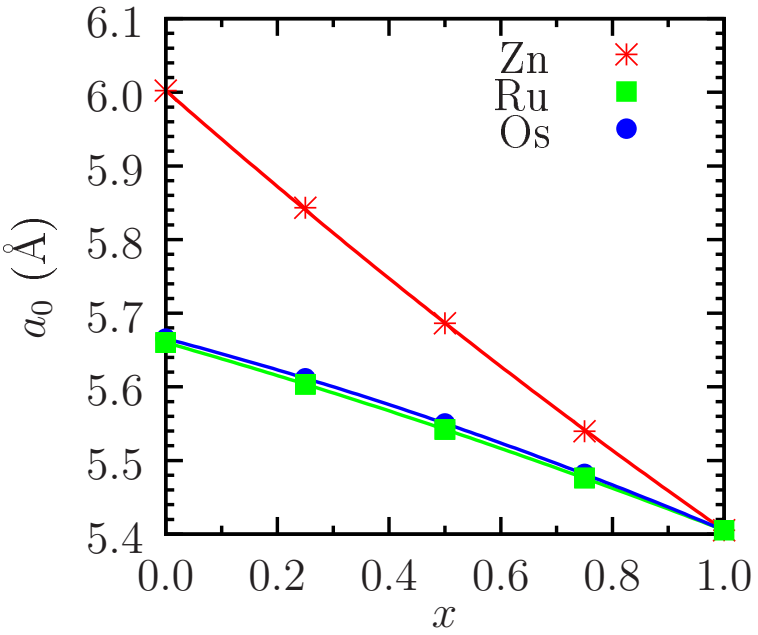

Figure 4-1: PBE lattice constant of $Fe_xM_{1-x}S_2$ as a function of x. The bowing parameters for M=Zn, Ru, and Os are $b_a = 0.0677$, -0.0382, and -0.0601 Å, respectively.

In Fig. 4-4, we show the miscibility of these systems by plotting the enthalpy of mixing (ΔH) as a function of concentration. The fitted regular solution interaction parameter is 851, 222, and 231 meV/FU for Zn, Ru, and Os, respectively. Using Eq. (4.4), the critical temperature at the top of the miscibility gap is estimated to be 4940, 1290, and 1340 K, respectively (Table 4.2), which is well above the melting temperature of pyrite ($T_m = 1016$ K; see Ref. [5]). The elastic constants calculated at $x = 0.5$ and the critical temperature of the spinodal instability are also given in Table 4.2.

Our results indicate that all three elements, Zn, Ru, and Os, may be difficult to incorporate in FeS_2. A similar problem has been identified when trying to design $(Fe, Mn)S_2$ mixtures in order to control the low-to-high spin transition [52].

4.3.2 Elements that do not form pyrite structures with S

In principle, alloying elements obviously do not have to form the pyrite structure in their binary with S in order to be effective at increasing the gap of FeS_2. However, such potential alloying elements are less likely to be miscible. This can be observed by considering the total enthalpy of the mixing reaction,

$$\Delta H = \Omega x_{\mathrm{Fe}} x_{\mathrm{M}} + x_{\mathrm{M}} \Delta H_{p' \to \mathrm{pyrite}}, \tag{4.8}$$

which besides the regular-solution-like term now also contains a positive promotion energy to bring the M sulfide from its ground state phase p' to the pyrite structure. While we do not calculate $\Delta H_{p' \to \mathrm{pyrite}}$ for these elements, we find that the regular solution enthalpy alone

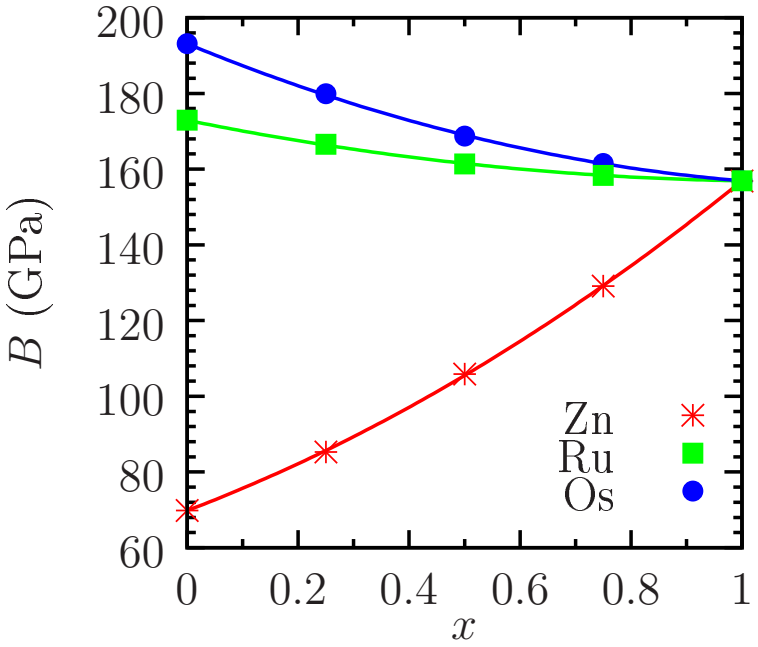

Figure 4-2: Bulk modulus of $Fe_xM_{1-x}S_2$ as a function of x. The bowing parameters for M=Zn, Ru, and Os are $b_B = 31.4$, 13.6, and 24.0 GPa, respectively.

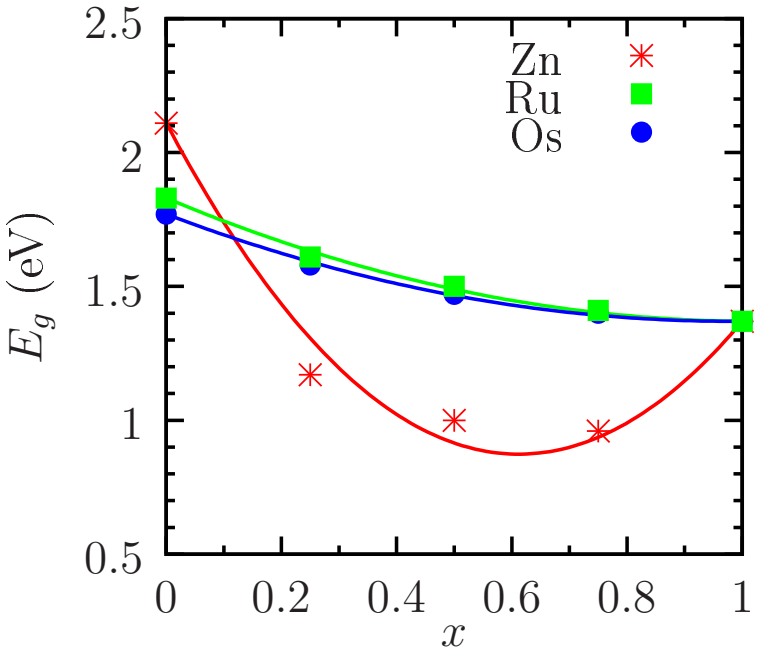

Figure 4-3: Band gap of $Fe_xM_{1-x}S_2$ as a function of x. The bowing parameters for M=Zn, Ru, and Os are $b_g = 3.3$, 0.44, and 0.41 eV, respectively.

Table 4.1: Lattice constants (a_0 as calculated within PBE; in Å), bulk modulus (B in GPa), pressure derivative of the bulk modulus (B'), and Δ-sol fundamental gap (E_g in eV) of $Fe_xM_{1-x}S_2$. Experimental values are given in brackets whenever available. The $x = 1$ data set refers to FeS_2. B and B' are given at the calculated lattice parameter, while E_g is calculated at the lattice parameter that is linearly interpolated between the experimental lattice parameter of the end members.

M	x	a_0	B	B'	E_g
-	1	5.405 (5.416)[a]	156.9	5.47	1.4 (0.95)[b]
Zn	0.75	5.540	129.1	4.83	1.0
	0.5	5.686	105.9	4.66	1.0
	0.25	5.843	85.3	2.32	1.2
	0	6.002 (5.954)[c]	69.8	5.04	2.1 (2.5)[d]
Ru	0.75	5.476	158.3	4.93	1.4
	0.5	5.542	161.4	5.21	1.5
	0.25	5.603	166.6	4.79	1.6
	0	5.660 (5.611)[e]	172.9	4.94	1.8 (1.3)[b]
Os	0.75	5.482	161.5	4.92	1.4
	0.5	5.550	168.7	5.17	1.5
	0.25	5.612	179.9	4.61	1.6
	0	5.666 (5.619)[f]	193.1	4.96	1.8 (2.0)[b]

[a] Ref. [4].
[b] Ref. [5].
[c] Ref. [92].
[d] Ref. [35] (estimate).
[e] Ref. [96].
[f] Ref. [97].

Table 4.2: Elastic constants (in GPa) and critical temperatures [T_c and T_c^* obtained from Eqs. (4.4) and (4.5), respectively; in K] of $Fe_{0.5}M_{0.5}S_2$.

M	c_{11}	c_{12}	T_c	T_c^*
Zn	199.8	59.0	4940	3350
Ru	401.0	41.5	1290	648
Os	430.7	37.7	1340	615

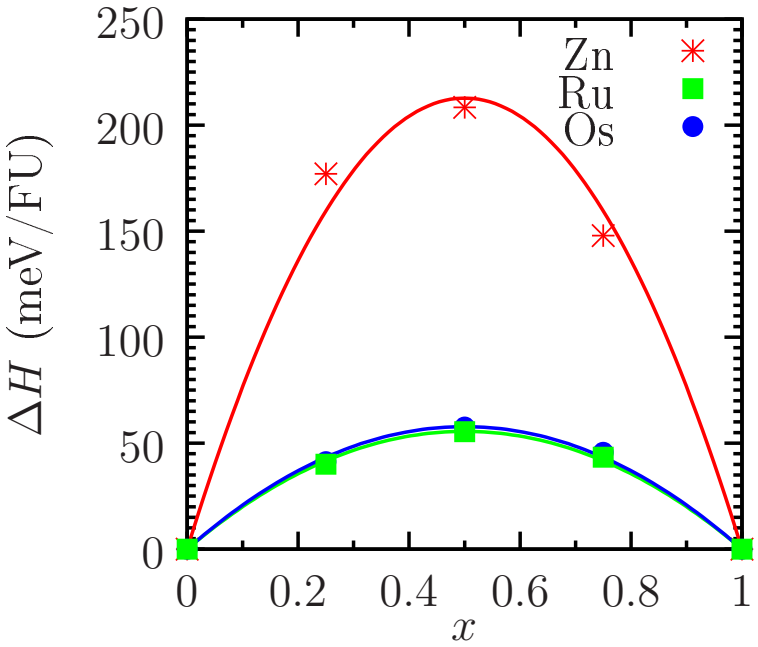

Figure 4-4: Mixing enthalpy of $Fe_xM_{1-x}S_2$ as a function of x. The bowing parameters for M=Zn, Ru, and Os are $\Omega = 851$, 222, and 231 meV/FU, respectively.

is already quite limiting for mixing these elements into pyrite.

We obtain the Δ-sol band gap at the PBE lattice constant (Table 4.4) for each M in the hypothetical MS_2 pyrite crystal structure, since the experimental lattice constants for these structures are unknown. Results are listed in Table 4.3 in ascending order of the atomic number of M. Hypothetical semiconductor compounds whose band gap is higher than that of FeS_2 include the group II elements—Be, Mg, Ca, Sr, and Ba—as well as the transition metal Cd. For these six potential candidates, we investigate the band gap bowing parameter and whether they are miscible with FeS_2.

Figure 4-5 shows the band gap bowing effect of alloying pyrite with the six candidates. We observe an increasing trend in the bowing parameter down the group II elements, ranging from 3.1 eV in $(Fe, Be)S_2$ to 6.8 eV in $(Fe, Ba)S_2$. Due to the large bowing effect, band gaps at intermediate compositions are considerably smaller than FeS_2. In Fig. 4-6, the mixing enthalpy exhibits a similar trend such that the $(Fe, M)S_2$ system becomes increasingly immiscible as M goes down group II. The interaction parameter for Be already translates to a critical temperature of 2740 K [Eq. (4.4)]. Therefore, these materials are unlikely candidates to increase the band gap of pyrite.

4.4 Discussion

We have evaluated the potential of a large number of alloying elements to increase the band gap of FeS_2. In addition to the known higher-gap pyrites—ZnS_2, RuS_2, and OsS_2—we also find the group II elements and Cd have larger Δ-sol gaps in the pyrite structure than FeS_2

Table 4.3: Δ-sol fundamental gaps for elements that do not form the pyrite structure with S (E_g in eV). The potential candidates are the group II elements (Be, Mg, Ca, Sr, Ba) and Cd.

M	E_g	M	E_g	M	E_g	M	E_g
Be	2.02	Ga	0.20	Rh	0.25	Ta	0.15
Mg	2.50	Ge	0.94	Pd	0.27	W	0.14
Si	0.48	Sr	2.30	Ag	0.28	Re	0.15
Ca	2.46	Y	−0.63	Cd	1.68	Ir	−0.09
Sc	−0.57	Zr	0.87	In	−1.09	Pt	0.24
Ti	0.26	Nb	0.20	Sn	0.93	Au	0.31
V	0.14	Mo	0.15	Ba	2.07	Hg	0.59
Cr	0.12	Tc	0.13	Hf	1.14	Pb	1.33

Table 4.4: Lattice constant (a_0 in Å), bulk modulus (B in GPa), pressure derivative of the bulk modulus (B'), and band gap (E_g in eV) of $Fe_xM_{1-x}S_2$ for candidates M that do not form the pyrite structure with S. The $x = 1$ data set refers to FeS_2.

M	x	a_0	B	B'	E_g
-	1	5.405	156.9	5.47	1.4
Be	0.75	5.443	134.9	4.50	1.0
	0.5	5.480	116.2	4.32	1.0
	0.25	5.514	100.5	4.42	1.1
	0	5.543	88.1	4.10	2.0
Mg	0.75	5.572	123.3	4.39	0.89
	0.5	5.752	97.5	4.60	0.91
	0.25	5.940	77.2	4.57	1.1
	0	6.133	59.9	4.57	2.5
Ca	0.75	5.692	113.8	4.98	0.55
	0.5	6.005	83.2	4.92	0.53
	0.25	6.333	60.5	4.75	0.97
	0	6.678	44.4	4.32	2.5
Sr	0.75	5.761	106.8	4.55	0.24
	0.5	6.158	75.4	5.29	0.31
	0.25	6.580	52.1	4.22	0.75
	0	7.020	37.6	4.53	2.3
Cd	0.75	5.634	123.6	5.23	0.61
	0.5	5.879	96.4	4.48	0.61
	0.25	6.139	74.3	4.81	0.79
	0	6.412	57.1	4.57	1.7
Ba	0.75	5.827	101.7	4.54	0.04
	0.5	6.321	67.4	5.36	0.23
	0.25	6.851	44.1	5.26	0.57
	0	7.403	31.8	4.36	2.1

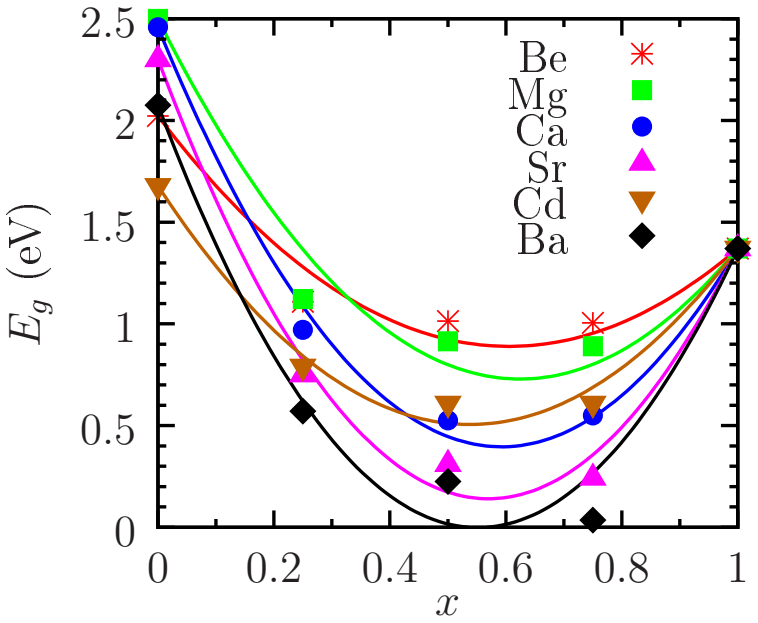

Figure 4-5: Band gap bowing of $Fe_xM_{1-x}S_2$, where M=Be, Mg, Ca, Sr, Cd, Ba. For group II candidates, the bowing effect becomes more prominent down the group.

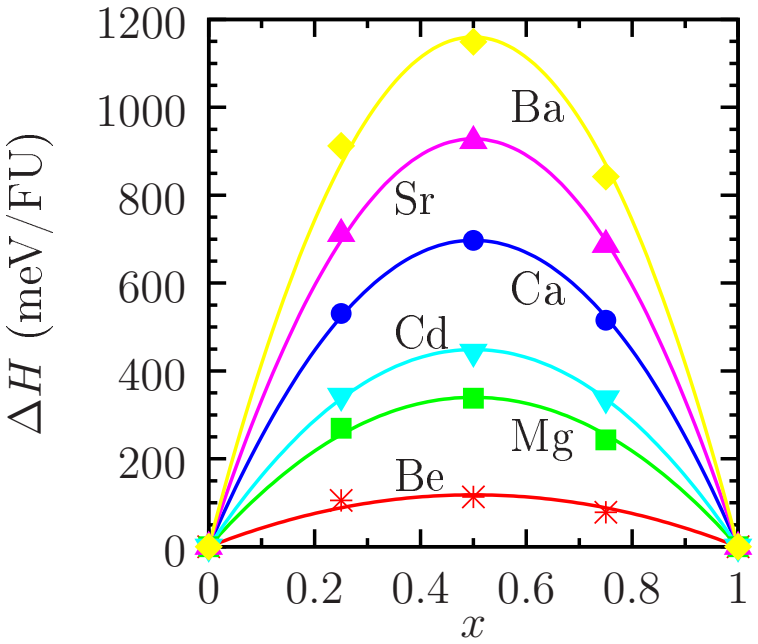

Figure 4-6: Mixing enthalpy of $Fe_xM_{1-x}S_2$, where M=Be, Mg, Ca, Sr, Cd, Ba. For group II elements, the miscibility decreases down the group.

(Table 4.3). The lattice constants of all these candidate systems closely follow Vegard's law (Tables 4.1 and 4.4). While small gap bowing ($b_g \approx 0.4$ eV) and band gap enhancement are observed for Ru and Os, large gap bowing is observed in other systems, ranging from 3.1 eV in Be to 6.8 eV in Ba, resulting in a decrease in the band gap of FeS_2 at intermediate alloying concentrations (Figs. 4-3 and 4-5). In all candidate systems considered, the mixing enthalpy ΔH is the most limiting quantity, as it inhibits alloying into FeS_2 (Figs. 4-4 and 4-6). Even within the most miscible systems, $(Fe, Ru)S_2$ and $(Fe, Os)S_2$, the regular solution critical temperature is around 1300 K, substantially higher than the melting point of FeS_2 (Table 4.2). The problem is further compounded by the fact that the large positive ΔH correlates to large band gap bowing (compare Figs. 4-3 and 4-4; Figs. 4-5 and 4-6), making all elements that have larger gaps in the (hypothetical) pyrite structure examined in this study ineffective to increase the band gap of pyrite.

The correlation between band gap bowing and miscibility can be traced to differences in ionic radius and electronegativity between the solvent and solute. We shall denote the differences as $\Delta r = r_{\mathrm{M}} - r_{\mathrm{Fe}}$ and $\Delta\chi = \chi_{\mathrm{M}} - \chi_{\mathrm{Fe}}$, respectively. In Table 4.5, we list the calculated band gap bowing parameter and interaction parameter of all examined candidate systems together with their experimental Shannon ionic radius [98] (low spin 2+ charge state in octahedral configuration; see Chapter 2) and electronegativity [99]. As illustrated in Fig. 4-7, we observe that the interaction parameter increases with both $\Delta\chi$ and Δr, indicating the $(Fe, M)S_2$ system is less miscible for larger differences in electronegativity or size.

On the other hand, for elements that have been successfully incorporated into pyrite, namely, the transition metals Co, Ni, and Cu (Sec. 4.1) [91,92], the corresponding Shannon ionic radius is 0.65, 0.69, and 0.73 Å [98], and the electronegativity is 1.88, 1.91, and 1.90 [99]. The differences compared to Fe are $\Delta r = 0.04$, 0.08, and 0.12 Å, and $\Delta\chi = 0.05$, 0.08, and 0.07, respectively, for Co, Ni, and Cu. Therefore, Co is expected to be the most soluble element within pyrite. Indeed, it has been experimentally demonstrated that Co forms a solid solution with pyrite at all compositions [91]. $Fe_xNi_{1-x}S_2$ has also been synthesized for $0.4 \leq x \leq 0.6$, showing substantial solubility [92]. As for Cu, although its electronegativity is similar to that of Fe, the ionic radius difference is 0.12 Å, comparable to Mg and Zn (Table 4.5). A limited solubility is exhibited in $Fe_xCu_{1-x}S_2$, where compositions of only $0.16 \leq x \leq 0.27$ are achieved [92]. Despite their different degrees of solubility, the Co, Ni, and Cu disulfides have lower band gaps [5], and are not suitable for the band gap enhancement of pyrite, as pointed out in Sec. 4.1. The next element in the transition metal series, Zn, has a comparable size difference to Cu ($\Delta r = 0.13$ Å) and a larger estimated band gap (2.5 eV; Ref. [35]) that is verified computationally (2.1 eV; Table 4.1). However, in this case, its electronegativity difference of 0.18 makes ZnS_2 highly immiscible with FeS_2 and causes a large band gap bowing as shown in Fig. 4-3. Based on our results, we question whether Zn can really be effective in increasing the band gap and OCV of pyrite, as proposed by Altermatt *et al.* [89]. [Note that natural impurities typically occur below $O(10^{19})$ cm^{-3} in pyrite; see Refs. [5] and Chapter 3.] The strong positive correlations between miscibility and differences in ionic radius and electronegativity observed in this study may serve as general

Table 4.5: Shannon ionic radius [98] (r) and electronegativity [99] (χ) of M, and band gap bowing parameter (b_g) and interaction parameter (Ω) of $(Fe, M)S_2$. Data for Fe are shown in the first row. The ionic radii of Ru^{2+} and Os^{2+} are not available.

M	r (Å)	χ	b_g (eV)	Ω (meV/FU)
-	0.61	1.83	-	-
Be	0.45	1.57	3.1	473
Mg	0.72	1.31	4.5	1360
Ca	1.00	1.00	5.9	2790
Zn	0.74	1.65	3.3	851
Sr	1.18	0.95	6.6	3710
Ru	-	2.2	0.44	222
Cd	0.95	1.69	4.1	1800
Ba	1.35	0.89	6.8	4640
Os	-	2.2	0.41	231

guiding rules in materials design for band gap engineering in other systems.

We remark on the improvement of calculated band gaps using the Δ-sol method. The GGA band structures of ZnS_2, RuS_2, and OsS_2 are shown in Fig. 4-8. (See Chapter 2 for the band structure of FeS_2.) Going down the Fe column in the periodic table (Fe, Ru, Os), the experimental band gap increases monotonically from 0.95, 1.3, to 2.0 eV. The Kohn-Sham gap [$\epsilon_{\mathrm{CBM}} - \epsilon_{\mathrm{VBM}}$, which is the difference in eigenvalues at the conduction band minimum (CBM) and valence band maximum (VBM)] down the group is, respectively, 0.4, 0.4, and -0.07 eV, which corresponds to an increasingly severe underestimation of 0.55 (-58%), 0.9 (-69%), and 2 eV (-100%), as listed in Table 4.1. This trend is in direct contradiction to the common belief that *relative* Kohn-Sham gaps within a chemically similar family of materials should be in reasonable agreement with experiment. On the other hand, the Δ-sol method yields band gaps of 1.4 (+47%), 1.8 (+38%), and 1.8 eV (-10%), respectively, showing substantial improvement in both the accuracy and the qualitative trend.

Due to the significant discrepancy between the Kohn-Sham gap and the experimental gap, an *ad hoc* correction is usually made such that the band gaps of the end members are fixed at their experimental gaps, and the gaps at intermediate compositions are adjusted by linear interpolation of the gap errors at $x = 0$ and $x = 1$. This GGA band gap correction scheme can be found in, e.g., Ref. [100]. One may question whether the implementation of such an interpolation scheme would affect our results, since the pyrite band gap is calculated to be 1.4 eV within the Δ-sol method, which is 0.45 eV higher than the experimental value [5], and a downward shift at $x = 1$ in Fig. 4-5 would seem to make the candidate systems more effective. However, we do not show such corrections in this study for three reasons: (i) The band gap bowing parameter is obtained by fitting the calculated band gaps to a quadratic function, and it is independent of a linear correction term. (ii) The band gap at $x = 0.5$ is significantly smaller than that of both end members for most of the materials examined here, yielding a substantial bowing parameter. Since the bowing parameter [$O(1)$ eV] is much

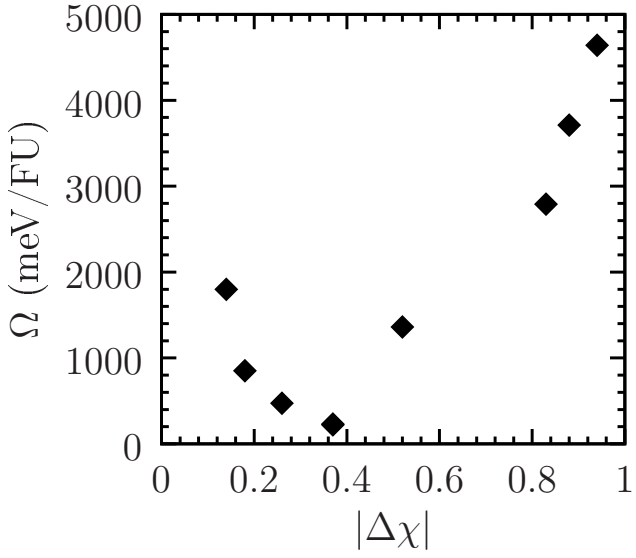

(a)

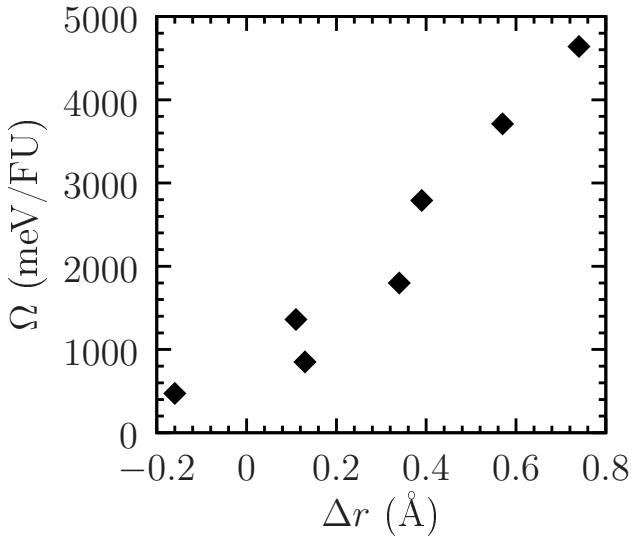

(b)

Figure 4-7: Interaction parameter (Ω) as a function of (a) difference in electronegativity [99] ($\Delta\chi$); and (b) difference in Shannon ionic radius [98] (Δr). Ru and Os are not plotted in (b) because their Shannon ionic radii in the 2+ state are not available.

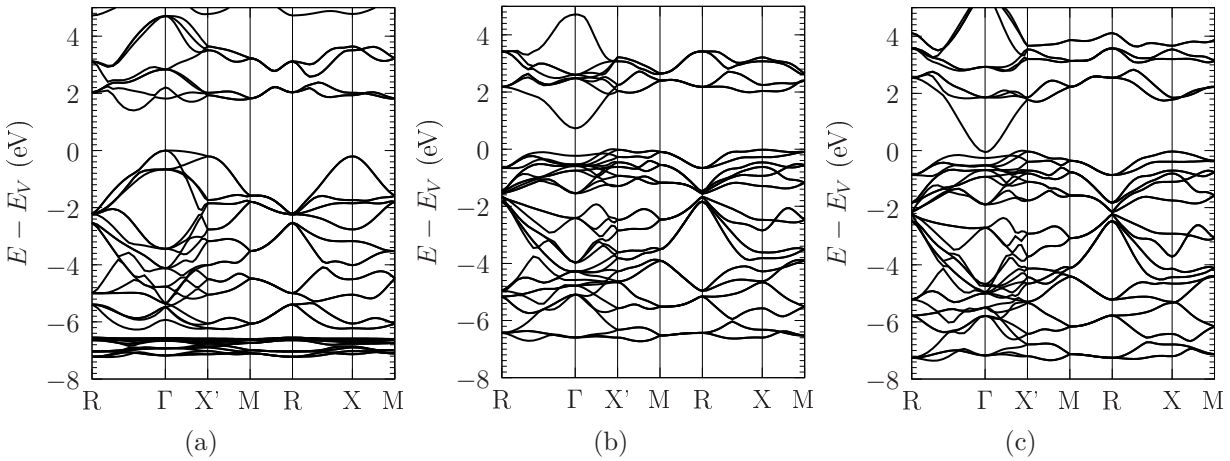

Figure 4-8: Band structure of (a) ZnS_2; (b) RuS_2; and (c) OsS_2.

larger than the mean error in the Δ-sol gap [$O(0.1)$ eV] [67], the band gap would decrease with solute concentration near the FeS_2 end member regardless of whether the correction is applied. Thus, the conclusion of whether a candidate is feasible would remain the same even if the correction scheme were to be adopted. (iii) The experimental band gaps for the nonisostructural candidates in the pyrite structure are unknown. It would be inconsistent to use experimental gaps at one end (Fe limit) and computed gaps at the other (M limit).

Only ordered structures have been used in our calculations. Due to the fact that the cation sites form a face-centered cubic sublattice (Chapter 2), there is only one unique configuration at $x = 0.25$, 0.5, and 0.75 for the unit cell. One may wonder if random cation arrangements would give substantially different results. Special quasirandom structures (SQS) are commonly used to simulate the structure of a random alloy using a small supercell (typically $2 \times 2 \times 2$) whose correlation function closely approximates that of an ideal random alloy for a given concentration [101]. We have tested the case of $(Fe, Zn)S_2$, using the initial structure generated by von Pezold *et al.* [102] within the Alloy Theoretic Automated Toolkit (ATAT) code [103]. The ionically-relaxed mixing enthalpy obtained from the SQS approach is even higher than that obtained from the unit cell approach. Given that the mixing enthalpy ΔH obtained from the latter is already highly limiting for all systems, we have not carried out further investigations on the configurational effects using the SQS approach. For the same reason, the $\Delta H_{p' \to \text{pyrite}}$ term in Eq. (4.8) has not been evaluated. We do recommend that, however, if a successful candidate were identified from the screening procedure, then more detailed analyses of the phase stability and ordering effects should be performed.

While our results offer a pessimistic perspective on the likelihood of increasing the band gap of FeS_2, it is important to note that there are some possibilities that we have not considered:

(i) *Anion mixing.* Isovalent alternatives for the anion are very limited. $FeSe_2$ and $FeTe_2$ crystallize in the marcasite phase and are nonisostructural to pyrite [104]. The experimental band gap of the diselenide varies from 0.5 to 1 eV [104, 105], and that of the ditelluride is

even smaller [104], which is undesirable.

(ii) *Mixing in both sites.* Isostructural diselenides and ditellurides include the compounds of such elements as Mn, Ru, Os, and Co [5]. The $(\mathrm{Fe,M})(\mathrm{S,A})_2$ class of materials, where M is one of the above transition metals and A=Se or Te, has not been studied. Unfortunately, the toxicity and scarcity of these chalcogens would make them unfavorable for large-scale photovoltaic applications.

(iii) *Mixtures of alloying cations of the form* $(\mathrm{Fe,M,N})\mathrm{S}_2$. Here the combined aliovalent alloying elements M and N should average to a 2+ charge. However, it is likely that a large addition of such elements will lead to the formation of intermediate compounds due to the effective electrostatic interaction between cations of different charge [106].

Finally, it has also been amply demonstrated that high supersaturation of alloying elements can be achieved in materials with far-from-equilibrium techniques such as pulsed-laser melting [107]. In these situations the spinodal instability will play a key role in the reliability and durability of the synthesized product.

4.5 Conclusions

The feasibility of alloying pyrite FeS_2 to enhance its band gap is investigated from first-principles. Among the isostructural candidates (Zn, Ru, Os), band gap enhancement is observed for Ru and Os, but they are expected to exhibit poor miscibility. Using a materials screening procedure, we identify six nonisostructural candidates, namely, the group II elements (Be, Mg, Ca, Sr, Ba) and Cd, that have larger band gaps in the pyrite structure compared to FeS_2. Large band gap bowing effects are found in these systems, making them ineffective to enhance the band gap of pyrite. We also observe positive correlations between immiscibility and differences in the ionic radius and electronegativity.

Chapter 5

Size-pH effects on the relative stability of FeS_2 polymorphs

The beginning of knowledge is the discovery of something we do not understand.

FRANK HERBERT

5.1 Introduction

As already introduced in Chapter 1, the effect of nanoparticle size on the stability of polymorphs is well understood in terms of surface energies and surface-to-bulk ratios [8],

$$G = g_b V + \gamma A, \tag{5.1}$$

where g_b is the bulk Gibbs free energy density, γ is the surface energy, A is the surface area, and V is the volume of the particle. On the other hand, for aqueous environments, Finnegan *et al.* have used a modified surface energy term in the free energy

$$G = g_b V + (\gamma + \sigma\phi)A, \tag{5.2}$$

where σ is the surface charge density and ϕ is the electrostatic potential difference between the solid and liquid phases, to explain the relative stability of TiO_2 polymorphs [108] under different pH conditions. While σ could be measured from potentiometric titration, from which ϕ could be inferred via the Gouy-Chapman equation, γ was not measured as a function of pH in their work. From the computational aspects, Barnard and Curtiss have been able to predict TiO_2 particle morphology by considering the energies of adsorbed surfaces that are representative of acidic or basic conditions [109]. More recently, it has been shown that the effect of pH can be quantitatively modeled via adsorbate chemical potentials to predict the morphology of $LiFePO_4$ particles [110, 111]. However, a direct computational verification of Eq. (5.2) has not been demonstrated for the prediction of the relative stability of polymorphs.

In this chapter we shall address how the combined effects of particle size and pH may alter the relative stability of pyrite and marcasite FeS_2, where the metastable phase marcasite is known to be stabilized in acidic solutions [9–11]. The rest of the section is organized as follows. (i) We shall first examine the size effect via computed pristine surface energies of pyrite and marcasite. Due to the lower surface energy of marcasite, we verify that marcasite is the stable phase at the nanoscale. (ii) Adsorbed surface energies are computed to model the morphology and phase stability as a function of pH, using the neutral-particle framework developed in Refs. [110, 111]. (iii) A direct computation of Eq. (5.2) is presented using the joint density functional theory (JDFT) approach [112, 113]. Charged particles are modeled by charged slabs that are balanced with a countercharge in the implicit aqueous medium within the JDFTx code [114–116].

5.2 Size dependence

In this section we first examine the role of pristine surface energies on the phase stability of polymorphs.

5.2.1 Theoretical framework

The γ in Eqs. (5.1) and (5.2), called the surface grand potential, is formally a Legendre transform of the free energy with respect to μn.

Definition. The surface energy is defined as

$$\gamma(T, P, \{\mu_i\}) = \frac{1}{2S}\left[G(T, P, \{n_i\}) - \sum_{i\in\mathcal{A}} n_i\mu_i(T, a_i)\right],$$

where S is the cross-sectional area of the slab and $\mathcal{A}$ is the set of all atoms (including any adsorbates) in the solid phase.

In practice, entropic and pressure effects are neglected, and the Gibbs free energy G is approximated by the total energy E, providing a more convenient means of computation:

$$\gamma \approx \frac{1}{2S}\left(E - \sum_{i\in\mathcal{A}} n_i\mu_i\right). \tag{5.3}$$

From this definition, we can rewrite the pristine surface energy in terms of total energies.

Corollary 5.1. Given a reference bulk total energy E_0 (for the same system size as the surface), the pristine surface energy is

$$\gamma_0 = \frac{E - E_0}{2S}.$$

Proof. Since the surface is pristine, $\mathcal{A}$ represents all atomic species of the bulk, which leads to

$$\sum_{i\in\mathcal{A}} n_i\mu_i = E_0. \qquad \square$$

Given a set of surface energies $\left\{\gamma_0^{hkl}\right\}$, the Wulff shape $\mathcal{W}$ of a single crystal particle can be constructed. At a given volume V, we define the effective radius as

$$r_{\text{eff}} = \left(\frac{3V}{4\pi}\right)^{\frac{1}{3}}. \tag{5.4}$$

We assume $\left\{\gamma_0^{hkl}\right\}$ is independent of r_{eff}. The total free energy of a single crystal particle is

$$G = g_b V + \sum_{(hkl)\in\mathcal{W}} \gamma_0^{hkl} A^{hkl}, \tag{5.5}$$

where g_b is the bulk free energy normalized by volume, and the summation is over all facets in the Wulff shape $\mathcal{W}$.

5.2.2 Computational details

Density functional theory (DFT) [36, 37] calculations within the Perdew-Burke-Ernzerhof (PBE) [45, 46] generalized gradient approximation (GGA) were performed using the plane-wave code Vienna Ab-initio Simulation Package (VASP) [40–43] with projector augmented wave (PAW) potentials [38, 39]. Energy convergence, surface energy calculation method, and Monkhorst-Pack [53] k-point selection criteria were similar to those already described in detail in Chapter 2.

We have only considered the low-index surfaces of pyrite [(100), (110), (111), and (210)] and marcasite [(100), (010), (001), (110), (101), and (011)].

5.2.3 Results

The pristine surface energies are shown in Table 5.1. From these energies, the Wulff shapes of pyrite and marcasite are constructed in Fig. 5-1. By computing the difference in total free energy [defined in Eq. (5.5)] between pyrite and marcasite, the size effect on the relative stability of pyrite and marcasite is shown in Fig. 5-2, where the energy difference in taken with respect to pyrite ($\Delta G = G_m - G_p$). Due to its lower surface energy [0.78 J/m^2 for (101)], marcasite is the stable phase at the nanoscale. [We remark that the marcasite (101) surface is the one that has the least lattice mismatch with the pyrite (100) surface, and that the interface between these two phases has been studied in Chapter 2.] It is predicted that pyrite becomes the ground state phase beyond a critical particle radius of 2-3 nm.

Table 5.1: Pyrite and marcasite low-index pristine surface energies. Marcasite has lower surface energy than pyrite.

Phase	(hkl)	γ_0 (J/m^2)
Pyrite	(100)	1.04
	(110)	1.72
	(111)	1.43
	(210)	1.48
Marcasite	(100)	1.72
	(010)	1.18
	(001)	1.35
	(110)	1.31
	(101)	0.78
	(011)	1.39

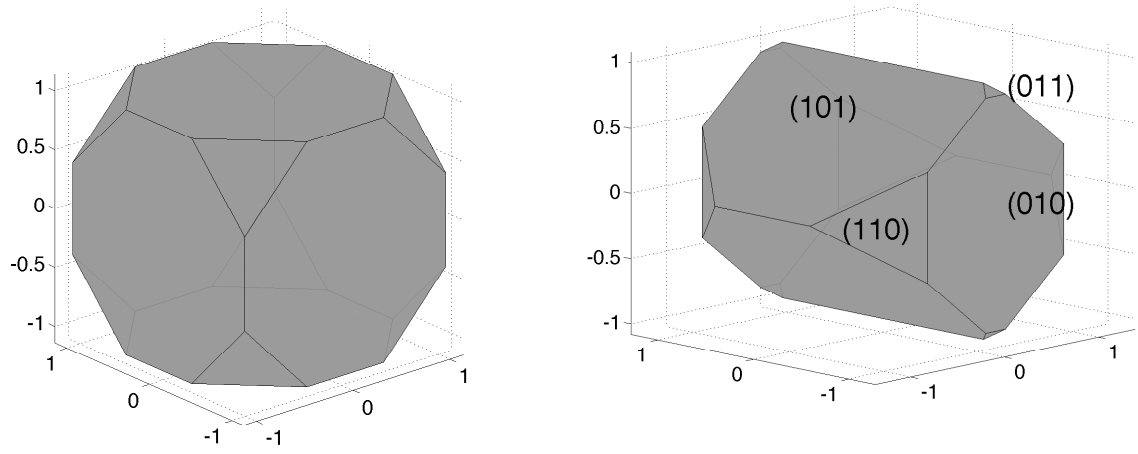

Figure 5-1: Wulff shapes of pyrite (left) and marcasite (right) obtained from pristine surface energies.

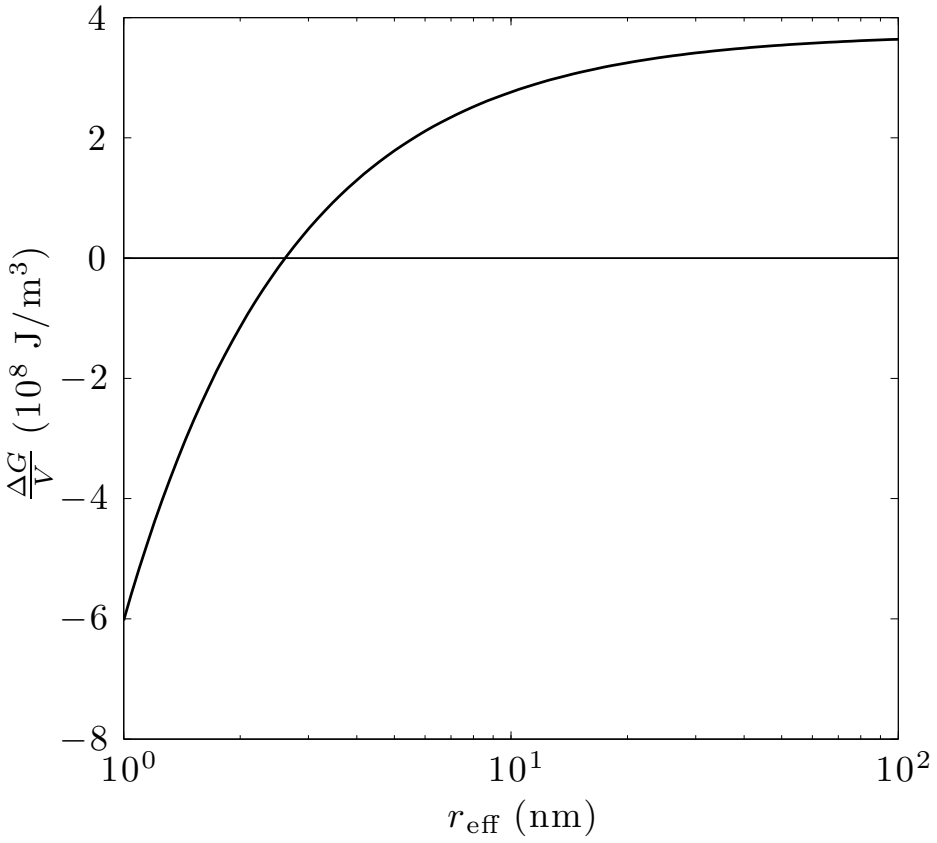

Figure 5-2: Relative stability of pyrite and marcasite as a function of particle size. The energy difference is taken with respect to pyrite.

5.3 pH dependence for charge-neutral particles

In this section we incorporate the effect of pH through the neutral-particle framework developed by Refs. [110, 111]. We provide an equivalent derivation in terms of pH instead of μ_{O}.

5.3.1 Theoretical framework

To model the effect of pH, four adsorbate species (O, OH, H_2O, H) are considered for each facet. The formation energy of water is

$$\Delta G^f_{\mathrm{H_2O}} = \mu^0_{\mathrm{H_2O}} - \mu^0_{\mathrm{H_2}} - \mu^0_{\mathrm{O}}. \tag{5.6}$$

The oxygen reference chemical potential ($\mu^0_{\mathrm{O}} = -4.57$ eV/O) is fitted to experimental formation energies of transition metal oxides [61]. The hydrogen reference chemical potential ($\mu^0_{\mathrm{H}} = -3.73$ eV/H) is fitted to reproduce the experimental formation energy of water ($\Delta G^f_{\mathrm{H_2O}} = -2.46$ eV/H_2O). We shall express the surface energy as a function of pH for each adsorbate, that is,

$$\gamma(\mathrm{pH}) = \frac{1}{2S}\left[E - \sum_i n_i \mu_i(\mathrm{pH})\right]. \tag{5.7}$$

(i) H-capped surface. Using the standard hydrogen electrode, $\mu^0_{\mathrm{H^+}} = \mu^0_{\mathrm{H}}$. Therefore,

$$\begin{aligned}\mu_{\mathrm{H^+}} &= \mu^0_{\mathrm{H^+}} + kT\ln a_{\mathrm{H^+}} \\ &= \mu^0_{\mathrm{H}} - kT\ln(10)\mathrm{pH}\end{aligned} \tag{5.8}$$

and

$$\gamma_{\mathrm{H}} = \frac{1}{2S}\left\{E - E_0 - n_{\mathrm{H}}\left[\mu^0_{\mathrm{H}} - kT\ln(10)\mathrm{pH}\right]\right\}. \tag{5.9}$$

(ii) H_2O-capped surface. Setting $\mu_{\mathrm{H_2O}} = \mu^0_{\mathrm{H_2O}}$, we have

$$\mu_{\mathrm{H_2O}} = \Delta G^f_{\mathrm{H_2O}} + \mu^0_{\mathrm{H_2}} + \mu^0_{\mathrm{O}} \tag{5.10}$$

and

$$\gamma_{\mathrm{H_2O}} = \frac{1}{2S}\left[E - E_0 - n_{\mathrm{H_2O}}\left(\Delta G^f_{\mathrm{H_2O}} + \mu^0_{\mathrm{H_2}} + \mu^0_{\mathrm{O}}\right)\right], \tag{5.11}$$

which is independent of pH.

(iii) OH-capped surface. Based on the fact that the proton and hydroxyl chemical potentials are coupled, the relation

$$\mu_{\mathrm{OH^-}} = \mu_{\mathrm{H_2O}} - \mu_{\mathrm{H^+}} \tag{5.12}$$

gives

$$\gamma_{\mathrm{OH}} = \frac{1}{2S}\left\{E - E_0 - n_{\mathrm{OH}}\left[\Delta G^f_{\mathrm{H_2O}} + \mu^0_{\mathrm{H}} + \mu^0_{\mathrm{O}} + kT\ln(10)\mathrm{pH}\right]\right\}. \tag{5.13}$$

A proof of Eq. (5.12) is given in Corollary 5.3.

(iv) O-capped surface. Similarly, we write

$$\mu_{O^{2-}} = \mu_{H_2O} - 2\mu_{H^+} \tag{5.14}$$

to obtain

$$\gamma_O = \frac{1}{2S}\left\{E - E_0 - n_O\left[\Delta G^f_{H_2O} + \mu^0_O + 2kT\ln(10)\text{pH}\right]\right\}. \tag{5.15}$$

5.3.2 Computational details

All slab calculations were kept charge neutral. An adsorbed surface was modeled with full coverage of one monolayer of H, H_2O, OH, or O species. Initial adsorption sites for O-containing species were chosen above the cation Fe, forming an Fe—O bond. For H, both Fe and S adsorption sites were computed on the pyrite (100) surface. We found that the Fe adsorption site was more energetically favorable for the neutral H adsorption process. Therefore, the Fe site was chosen for H-adsorption on all the other surfaces. The surfaces were allowed to relax.

5.3.3 Results

The surface energy diagrams of pyrite and marcasite are shown in Figs. 5-3 and 5-4, respectively. These diagrams are analogous to the semiconductor point defect formation energy diagrams (see Chapter 3) in the following ways. (i) Each surface energy line is obtained from a single computation. (ii) The slope is proportional to the charge state of the species. (iii) The most stable adsorbate species is indicated by the lower envelope of the lines. (iv) Kinks in the lower envelope represent critical pH values at which the adsorption of one species transitions into another.

It is observed that the proton-adsorbed surfaces in pyrite are almost never energetically favorable within the entire $[0, 14]$ pH range. The H_2O-adsorbed surface has the lowest surface energy under highly acidic conditions and transitions into either OH- or O-adsorbed as pH increases. The similar phenomenon is observed for marcasite, except that H-adsorption is favorable below pH ~ 2 for (110) and (011), and that O-adsorption on (110) has the lowest surface energy even under mildly acidic conditions, which is unusual. Notice that, at a given pH, it is possible that different adsorbates are favored on different facets of the Wulff shape.

Using this set of surface energies, the Wulff shapes can be constructed as a function of pH, where a few snapshots are shown in Fig. 5-5. We can now write the total free energy difference between pyrite and marcasite as a function of both pH and r:

$$\begin{aligned}\Delta G(\text{pH}, r) = \Delta g_b V(r) &+ \sum_{(hkl)\in\mathcal{W}^\alpha}\left[\min_i \gamma_i^{\alpha(hkl)}(\text{pH})\right] A^{\alpha(hkl)}(r) \\ &- \sum_{(hkl)\in\mathcal{W}^\beta}\left[\min_i \gamma_i^{\beta(hkl)}(\text{pH})\right] A^{\beta(hkl)}(r).\end{aligned} \tag{5.16}$$

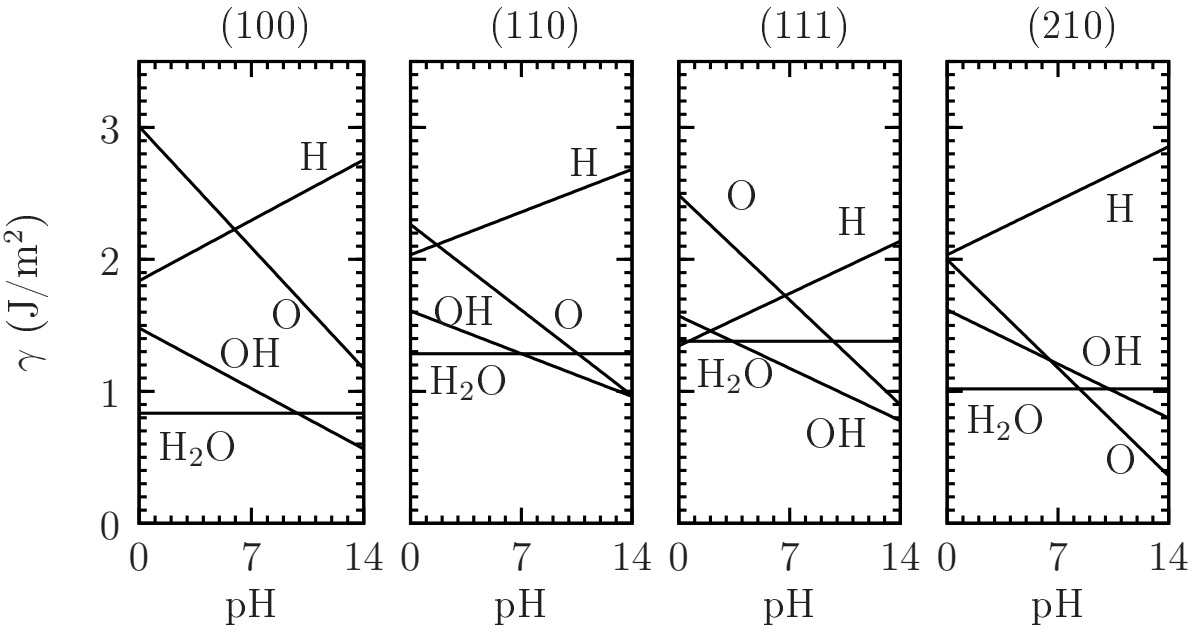

Figure 5-3: Surface energy versus pH diagram of pyrite.

The size-pH phase diagram for FeS_2 polymorphs is drawn in Fig. 5-6. Compared to the pristine surface case, the critical size transition from marcasite to pyrite remains at the nanoscale because the surface energies are of the same order of magnitude. While the prediction that pyrite is stable under basic conditions is qualitatively correct, the pH transition of 12 does not agree well with the empirical observation of 5 or 6 [10, 11]. The discrepancy may be caused by the unphysical assumption that particles remain charge neutral irrespective of the pH in the aqueous environment. This limitation will be addressed in the next section. Furthermore, we have neglected chemical reactions on the surface that may result in off-stoichiometry, possibility of co-adsorption, effects of other aqueous ionic species, as well as energetic contributions from the corners and edges of nanoparticles. Such complications are unfortunately beyond the scope of this thesis and will be left as future work.

5.4 Charged particles

Due to the inadequacy of the charge-neutral framework, we now consider the thermodynamics of charged particles in solution. Here we allow the possibility that an adsorbed surface can become charged as a result of chemisorption of ions from the aqueous environment. A generalized surface energy for charged slabs is derived and applied to the study of FeS_2 polymorphs.

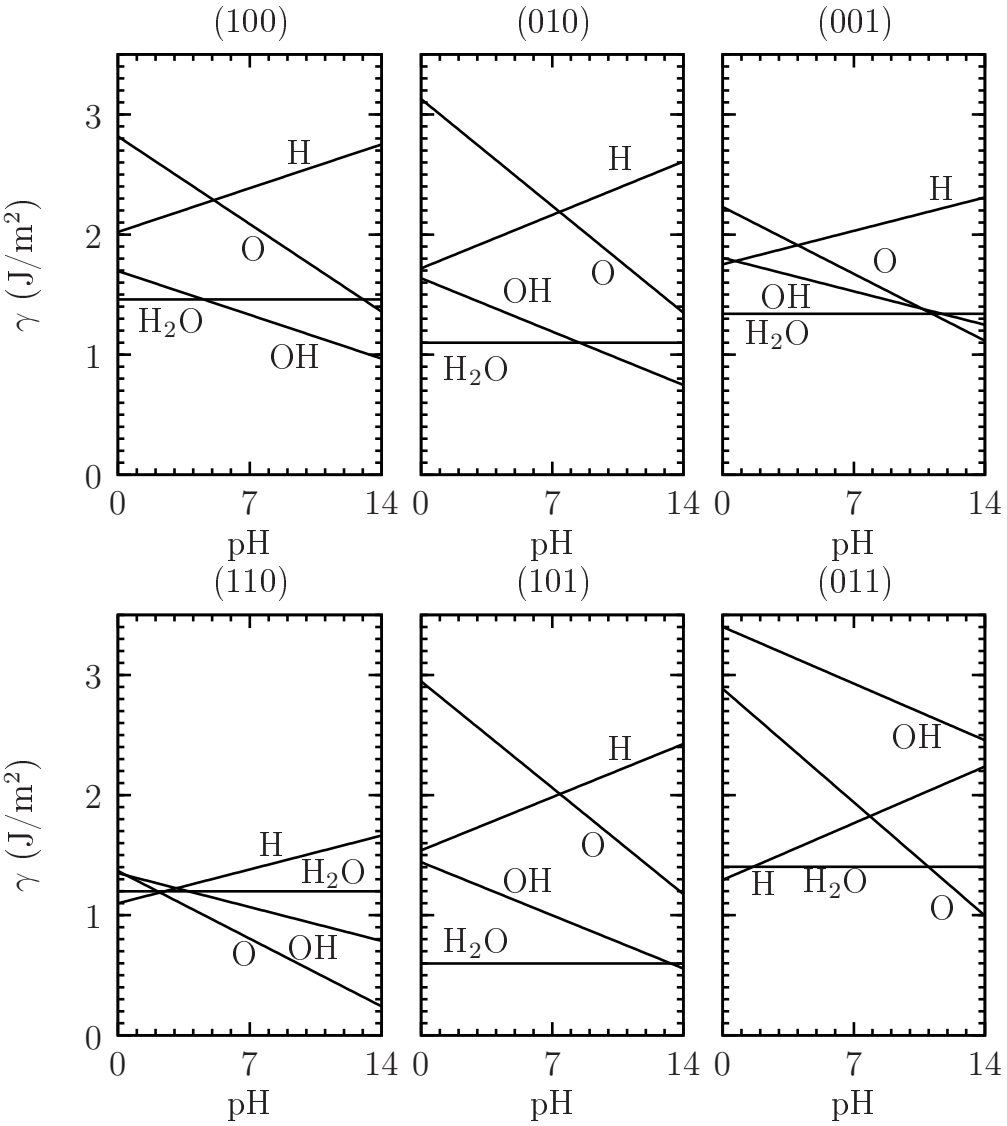

Figure 5-4: Surface energy versus pH diagram of marcasite.

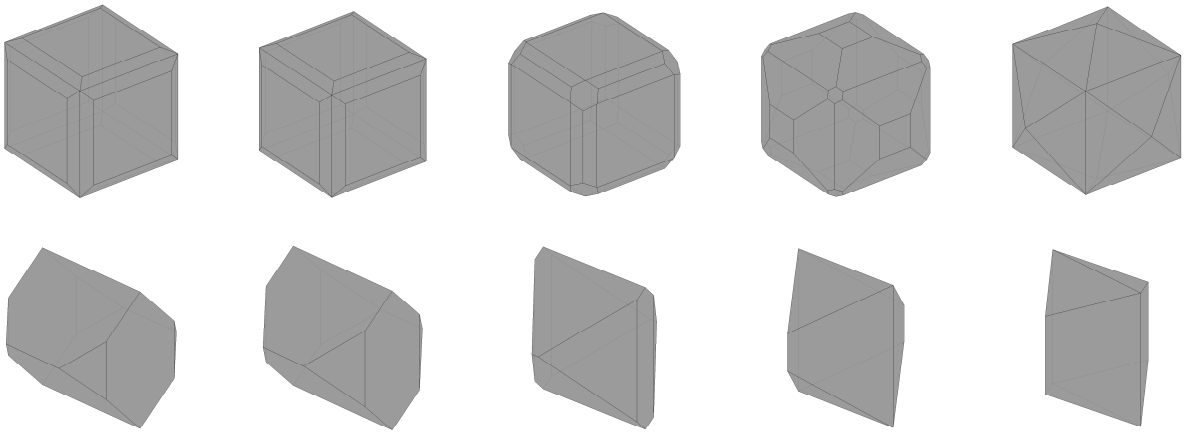

Figure 5-5: Wulff shape of pyrite (top) and marcasite (bottom). The pH is 1, 4, 7, 10, and 13 from left to right.

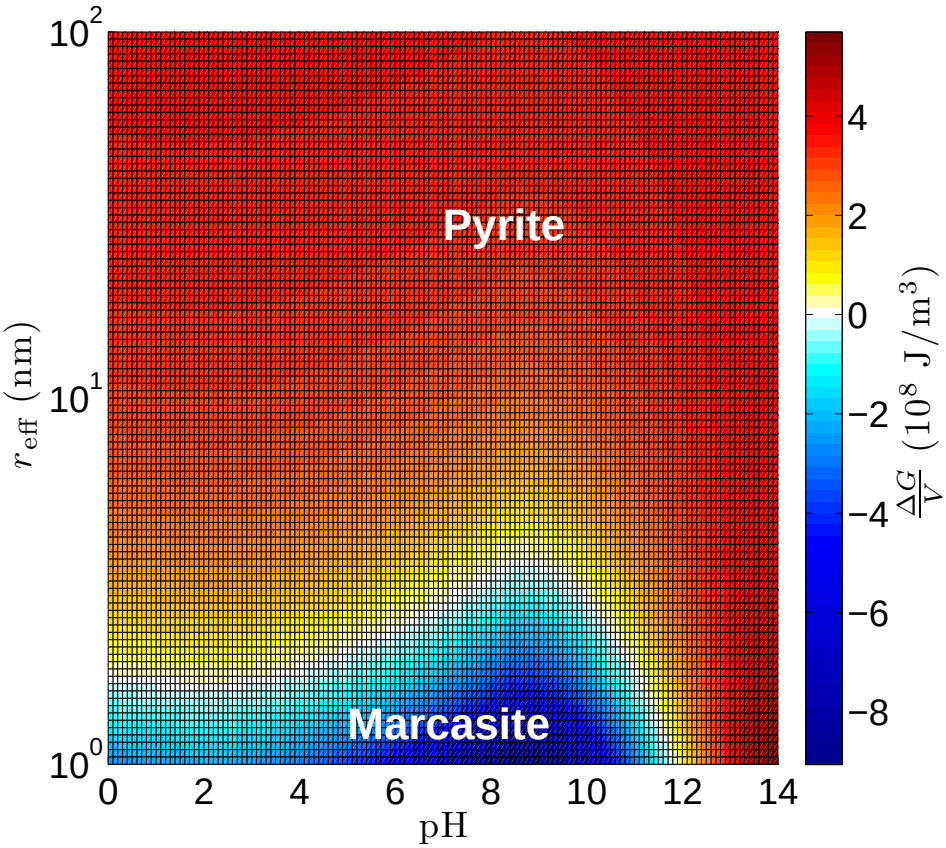

Figure 5-6: Size-pH phase diagram for FeS_2 polymorphs pyrite and marcasite. The energy difference is taken with respect to pyrite.

5.4.1 The electrochemical potential $\overline{\mu}$

Definition. For a (possibly charged) species i in phase α, the electrochemical potential is defined as [117]

$$\begin{aligned}\overline{\mu}_i^\alpha &= \mu_i^\alpha + z_i e\phi^\alpha \\ &= \mu_i^{0\alpha} + kT\ln a_i^\alpha + z_i e\phi^\alpha,\end{aligned}$$

where μ_i is the chemical potential, z_i is the charge of i, ϕ is the inner potential, and a_i is the activity.

Some simple properties of $\overline{\mu}$ are given below.

Lemma 5.2. (i) For uncharged species, $\overline{\mu}_i = \mu_i$. (ii) For a pure phase at unit activity, $\overline{\mu}_i = \mu_i^0 + z_i e\phi$. (iii) Equilibrium of species i between phases α and β holds when $\overline{\mu}_i^\alpha = \overline{\mu}_i^\beta$.

Proof. (i) An uncharged species i has $z_i = 0$. By definition, $\overline{\mu}_i = \mu_i$. (ii) Setting $a_i = 1$, we obtain $\overline{\mu}_i = \mu_i^0 + z_i e\phi$. (iii) This is obvious by starting from $\Delta G = 0$ and holding all other thermodynamic forces constant. □

We can now give a proof of Eq. (5.12).

Corollary 5.3. The chemical potentials of protons and hydroxyls are coupled by the relation

$$\mu_{\mathrm{H_2O}} = \mu_{\mathrm{H^+}} + \mu_{\mathrm{OH^-}}.$$

Proof. Consider the equilibrium condition:

$$\mathrm{H_2O} \rightleftharpoons \mathrm{H^+} + \mathrm{OH^-}.$$

Since H_2O is a neutral species, by (i) of Lemma 5.2, $\mu_{\mathrm{H_2O}} = \overline{\mu}_{\mathrm{H_2O}}$. At equilibrium [(iii) of Lemma 5.2],

$$\overline{\mu}_{\mathrm{H_2O}} = \overline{\mu}_{\mathrm{H^+}} + \overline{\mu}_{\mathrm{OH^-}}.$$

By definition of $\overline{\mu}$,

$$\begin{aligned}\overline{\mu}_{\mathrm{H^+}} + \overline{\mu}_{\mathrm{OH^-}} &= \mu_{\mathrm{H^+}} + e\phi + \mu_{\mathrm{OH^-}} - e\phi \\ &= \mu_{\mathrm{H^+}} + \mu_{\mathrm{OH^-}}.\end{aligned}$$

□

5.4.2 The electrochemical surface energy $\overline{\gamma}$

Consider the adsorption process of a charged species on a particle M in solution. We shall use proton adsorption in the following derivations, without loss of generality:

$$\mathrm{M} + \mathrm{H^+} \rightarrow \mathrm{MH^+}. \tag{5.17}$$

The reaction energy is

$$\begin{aligned}\Delta G_{\text{rxn}} &= \overline{\mu}^s_{\text{MH}^+} - \overline{\mu}^s_{\text{M}} - \overline{\mu}^l_{\text{H}^+} \\ &= \mu_{\text{MH}^+} + e\phi^s - \mu_{\text{M}} - \left[\mu^0_{\text{H}} - kT\ln(10)\text{pH} + e\phi^l\right] \\ &= \mu_{\text{MH}^+} - \mu_{\text{M}} - \left[\mu^0_{\text{H}} - kT\ln(10)\text{pH}\right] + e(\phi^s - \phi^l),\end{aligned} \tag{5.18}$$

where superscripts s and l indicate solid and liquid phases, respectively. The first three terms are a collection of chemical potentials, which by Eq. (5.3) can be written as $2S\widetilde{\gamma}$ for some form of $\widetilde{\gamma}$ (details in next section).

Definition. The electrochemical surface energy is defined as $\overline{\gamma} = \Delta G_{\text{rxn}}/2S$.

Using the above definition and rewriting $\phi = \phi^s - \phi^l$, we obtain

$$\overline{\gamma} = \widetilde{\gamma} + \sigma\phi. \tag{5.19}$$

Although the pH effect can be incorporated in the same way as presented in Sec. 5.3, one should notice that here $\widetilde{\gamma}$ is dependent on the charge of the slab. The surface charge density σ induces a potential difference of ϕ between the solid and liquid phases. These charge-dependent quantities are difficult to obtain from vacuum-slab computations due to spurious image charge interactions and the absence of a liquid medium. Recently, however, it has been shown that by including the aqueous region as a dielectric medium with a countercharge, these quantities can be reliably computed within joint density functional theory (JDFT; see Sec. 5.5.1), yielding potentials of zero charge that agree very well with experiment, without *ad hoc* energy corrections [113]. Thus, by obtaining electrochemical surface energies through Eq. (5.19), we can reconstruct a size-pH phase diagram for charged particles that would allow for the prediction of the relative stability of polymorphs:

$$\begin{aligned}\Delta G(\text{pH}, r) = \Delta g_b V(r) &+ \sum_{(hkl)\in\mathcal{W}^\alpha} \left[\min_i \overline{\gamma}_i^{\alpha(hkl)}(\text{pH})\right] A^{\alpha(hkl)}(r) \\ &- \sum_{(hkl)\in\mathcal{W}^\beta} \left[\min_i \overline{\gamma}_i^{\beta(hkl)}(\text{pH})\right] A^{\beta(hkl)}(r),\end{aligned} \tag{5.20}$$

which compared to Eq. (5.16) we have only replaced the vacuum surface energy γ with the electrochemical surface energy $\overline{\gamma}$.

5.4.3 A theorem on $\overline{\gamma}$

To understand how one can compute the electrochemical surface energy $\overline{\gamma}$, the nature of $\widetilde{\gamma}$ in Eq. (5.19) must be first elucidated by revisiting

$$\Delta G_{\text{rxn}} = \mu_{\text{MH}^+} - \mu_{\text{M}} - \left[\mu^0_{\text{H}} - kT\ln(10)\text{pH}\right] + e\phi. \tag{5.21}$$

We expand the first term into several energy differences:

$$\mu_{\mathrm{MH}^+} = \mu_{\mathrm{MH}}^{s/v} + \left(\mu_{\mathrm{MH}}^{s/l} - \mu_{\mathrm{MH}}^{s/v}\right) + \left(\mu_{\mathrm{MH}^+}^{s/l} - \mu_{\mathrm{MH}}^{s/l}\right), \tag{5.22}$$

where superscripts indicate the type of interface (solid s, liquid l, or vacuum v) present in the supercell. In doing so, the first term, together with the pH-dependent adsorbate chemical potential, is written as γ_{i^0} after normalization by the surface area, i.e., in the case of proton adsorption,

$$\gamma_{\mathrm{H}^0} = \frac{1}{2S}\left\{\mu_{\mathrm{MH}}^{s/v} - \mu_{\mathrm{M}} - \left[\mu_{\mathrm{H}}^0 - kT\ln(10)\mathrm{pH}\right]\right\}. \tag{5.23}$$

These energies have been calculated in the previous section on neutral particles.

The normalized energy difference in the first bracketed term of Eq. (5.22) is the surface solvation energy, written as $\gamma_{i^0,\mathrm{solv}}$. (The reference energy of the liquid region has already been taken into account in the JDFTx code.) Therefore,

$$\gamma_{\mathrm{H}^0,\mathrm{solv}} = \frac{1}{2S}\left(\mu_{\mathrm{MH}}^{s/l} - \mu_{\mathrm{MH}}^{s/v}\right). \tag{5.24}$$

In the second bracketed term of Eq. (5.22), we shall simply label the two total energies as Ξ and F, respectively. The energies cannot be directly compared because Ξ is obtained at constant electron chemical potential μ_e, while F is obtained at constant number of electrons n_e. Instead, comparison of the neutral $(\mu_0; n_0)$ and the charged $(\mu_1; n_1)$ systems can be achieved by performing a Legendre transform with respect to $\mu_e n_e$, i.e.,

$$\begin{aligned}
\gamma_{i^{0/\pm}} &= \frac{1}{2S}\left[\Xi(\mu_1) - \Xi(\mu_0) + n_0\delta\mu\right] \\
&= \frac{1}{2S}\left\{\Xi(\mu_1) - \left[F(n_0) - n_0\mu_0\right] + n_0\delta\mu\right\} \\
&= \frac{1}{2S}\left\{\Xi(\mu_1) - \left[F(n_0) - n_0\mu_1\right]\right\},
\end{aligned} \tag{5.25}$$

where a work done of $n_0\delta\mu$ is initially applied to the neutral system to bring the chemical potential from μ_0 to μ_1. The physical interpretation of $\gamma_{i^{0/\pm}}$ is the ionization energy of the surface. The concept is illustrated in Fig. 5-7. The potential difference between the solid and liquid phases is equal to $\delta\mu$, since the potential of the liquid is set to 0. Using typical lattice constants and atomic densities, a slab with full-coverage of charged adsorbate species yields surface charge densities on the order of $\sigma_{\max} \sim 1$ C/m^2. (It also corresponds to an unrealistic potential difference on the order of 10 V.) However, experimentally measured charge densities are one order of magnitude lower, which may be due to partial coverage or partial charge transfer into the bulk as a result of energetically unfavorable coulombic repulsion on the surface. For instance, Bonnett and Marzari have calculated that a proton adsorbed onto Pt(111) and Pt(100) only carries a charge of 0.09+ and 0.02+, respectively [118]. Therefore, $\Xi(\mu_1)$ is computed such that the resulting charge is only a fraction of the maximally-charged case, i.e., $\delta n/2S = -\eta\sigma_{\max}$, where η is chosen to be 0.1. The issues of partial coverage and

partial charges are left for future work.

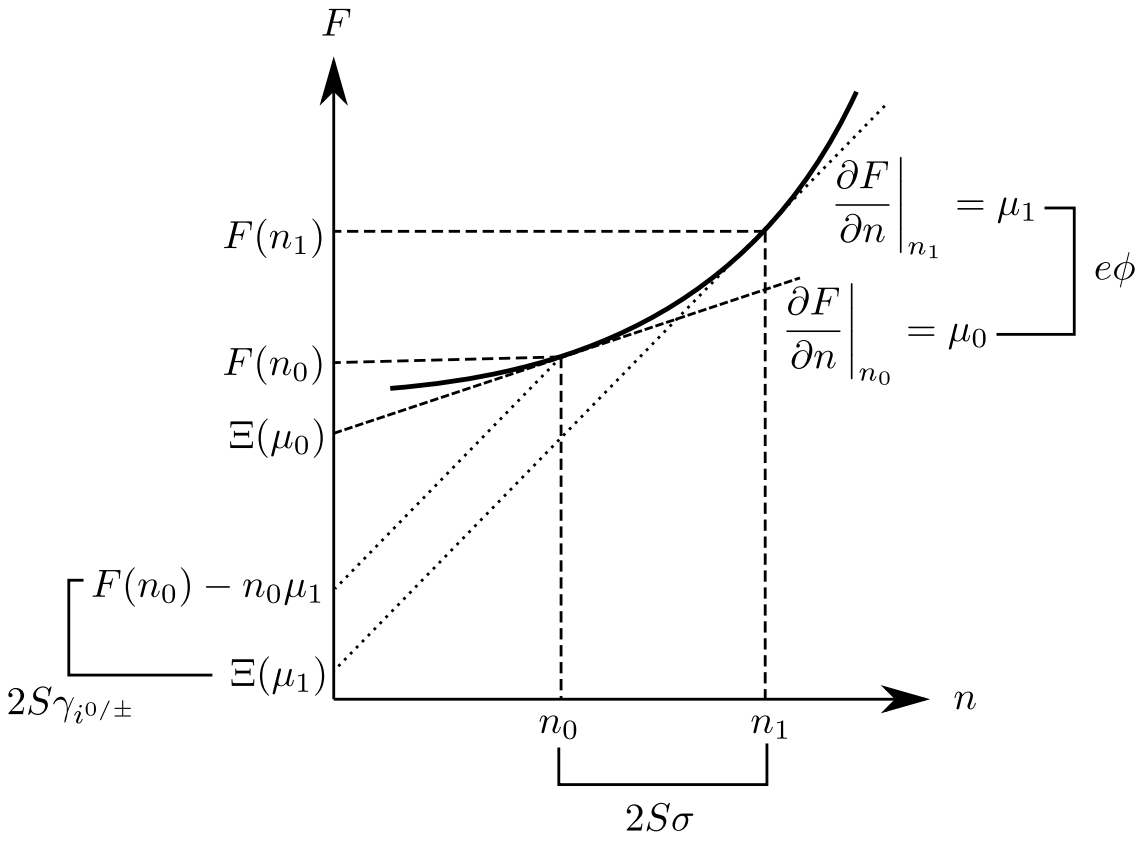

Figure 5-7: Schematic of the differences between F, Ξ, n, and μ, and their relationship to $\gamma_{i^{0/\pm}}$, σ, and ϕ. Legendre transform of $F(n_0)$ and $F(n_1)$ gives the quantities $\Xi(\mu_0)$ and $\Xi(\mu_1)$. The cross-sectional area is given by S.

We now arrive at the following theorem, where the derivation has already been shown.

Theorem 5.4. The electrochemical surface energy (with adsorbate species i) can be expressed in terms of the aforementioned surface energies:

$$\overline{\gamma}_i = \gamma_{i^0} + \gamma_{i^0,\text{solv}} + \gamma_{i^{0/\pm}} + \sigma\phi. \tag{5.26}$$

This equation represents, physically, the creation of a surface (γ_{i^0}), its solvation in water ($\gamma_{i^0,\text{solv}}$), and ionization of the surface ($\gamma_{i^{0/\pm}}$), inducing a potential difference between the solid and liquid phases ($\sigma\phi$). The third and fourth terms arise due to charge, and are irrelevant for neutral systems such as in the case of H_2O adsorption. Without loss of generality, the same procedure can be done for other charged adsorbate species OH^- and O^{2-}. Notice that Eq. (5.26) can also be derived by generalizing the definition of surface energy in Eq. (5.3)—

replace the chemical potentials with electrochemical potentials, i.e.,

$$\overline{\gamma} = \frac{1}{2S}\left(\overline{\Xi} - \sum_{i\in\mathcal{A}} n_i \overline{\mu}_i\right). \tag{5.27}$$

We verify that $\overline{\gamma}$ is indeed a generalization of γ such that the latter is recovered for a neutral surface.

Corollary 5.5. If $\mathcal{A}$ is neutral, then $\overline{\gamma} = \gamma$.

Proof. First note that for a neutral bulk, $\overline{\Xi}$ is just the total energy E. Then, by definition of $\overline{\mu}$,

$$\begin{aligned}\overline{\gamma} &= \frac{1}{2S}\left[E - \sum_{i\in\mathcal{A}} n_i(\mu_i + z_i e\phi^s)\right] \\ &= \frac{1}{2S}\left(E - \sum_{i\in\mathcal{A}} n_i\mu_i\right) - \frac{e\phi^s}{2S}\sum_{i\in\mathcal{A}} n_i z_i.\end{aligned}$$

Since $\mathcal{A}$ is neutral, $\sum_{i\in\mathcal{A}} n_i z_i = 0$, and, thus, we obtain

$$\overline{\gamma} = \frac{1}{2S}\left(E - \sum_{i\in\mathcal{A}} n_i\mu_i\right) = \gamma.$$

The result holds regardless of the presence of adsorbates. □

We remark that, for clean surfaces without adsorbates, Eq. (5.26) still holds such that

$$\overline{\gamma} = \gamma_0 + \gamma_S + \gamma_I + \sigma\phi, \tag{5.28}$$

where γ_0, γ_S, and γ_I are the pristine, solvation, and ionization surface energies, respectively. In this case, however, $\overline{\gamma}$ cannot be readily expressed as a function of pH.

5.5 Computational method

5.5.1 Joint density functional theory

Here the essence of joint density-functional theory (JDFT) is presented. Details can be found in Refs. [112, 113, 119]. The hamiltonian of a solid-liquid system can be expressed as

$$\mathcal{H}_{\text{JDFT}}[n, \{N_\alpha\}] = \mathcal{H}_{\text{DFT}}[n] + \mathcal{H}_l[\{N_\alpha\}] + \mathcal{H}_{s-l}[n, \{N_\alpha\}], \tag{5.29}$$

where $n(\mathbf{r})$ is the electron density of the solid, $\{N_\alpha(\mathbf{r})\}$ is the density of the nuclei of the atomic species in the environment, $\mathcal{H}_{\text{DFT}}$ is the hamiltonian of the solid within DFT, $\mathcal{H}_l$

is the hamiltonian of the liquid, and $\mathcal{H}_{s-l}$ is the hamiltonian for the solid-liquid coupling. This expression is exact in theory, but each term needs to be approximated in practice. The solid is approximated by $\mathcal{H}_{\rm KS}$, the standard Kohn-Sham density functional. Liquid effects are treated by a polarizable continuum model (PCM). It is assumed that the coupling term between the explicit solute and solvent environment is purely electrostatic. The last two functionals are approximated to be

$$\begin{aligned}\mathcal{H}_{\rm diel} &= \mathcal{H}_l + \mathcal{H}_{s-l} \\ &= \mathcal{H}_\epsilon[s,\epsilon] + \mathcal{H}_\kappa[s,\eta] + \iint d\mathbf{r}\, d\mathbf{r}'\, \frac{\rho_l(\mathbf{r}')}{|\mathbf{r}-\mathbf{r}'|}\left(\rho_s(\mathbf{r}) + \frac{\rho_l(\mathbf{r})}{2}\right) + \mathcal{H}_{\rm cav}[s],\end{aligned} \tag{5.30}$$

where $\rho_s(\mathbf{r}) = n(\mathbf{r}) - N(\mathbf{r})$ is the total charge density of the solid with both electron and nuclei contributions, $\mathcal{H}_\epsilon$ and $\mathcal{H}_\kappa$ describe the internal energies of the dielectric response of neutral molecules and ions, respectively. The last term includes all other effects (e.g., cavitation) of the fluid, and is assumed to take the form of

$$\mathcal{H}_{\rm cav}[s] = \tau \int d\mathbf{r}\, |\nabla s|, \tag{5.31}$$

where τ is an effective tension. The cavity shape function, s, is defined by the electron density $n(\mathbf{r})$ via

$$s(n(\mathbf{r})) = \frac{1}{2}\mathrm{erfc}\frac{\ln(n(\mathbf{r})/n_c)}{\sigma\sqrt{2}}. \tag{5.32}$$

The transition electron density n_c, transition width σ, and tension τ are fitted to solvation energies of selected molecules from quantum chemistry calculations. The local density of the solvent is thus $N_l(\mathbf{r}) = N_b s(n(\mathbf{r}))$, where N_b is the bulk density (molecules per volume). The dielectric constant and inverse Debye screening length are defined in terms of $N_l(\mathbf{r})$:

$$\epsilon(\mathbf{r}) = 1 + \frac{N_l(\mathbf{r})}{N_b}(\epsilon_b - 1), \tag{5.33}$$

$$\kappa(\mathbf{r}) = \kappa_b^2 \frac{N_l(\mathbf{r})}{N_b}. \tag{5.34}$$

It can be shown that, within the linear PCM approximation,

$$\mathcal{H}_{\rm diel} = \int d\mathbf{r} \left\{ \phi(\mathbf{r})\rho_s(\mathbf{r}) - \frac{\epsilon(\mathbf{r})}{8\pi}|\nabla\phi(\mathbf{r})|^2 - \frac{\epsilon_b\kappa^2(\mathbf{r})}{8\pi}[\phi(\mathbf{r})]^2 \right\}. \tag{5.35}$$

The total energy is minimized by solving the modified Poisson equation

$$\nabla\cdot[\epsilon(\mathbf{r})\nabla\phi(\mathbf{r})] - \epsilon_b\kappa^2(\mathbf{r})\phi(\mathbf{r}) = -4\pi[n(\mathbf{r}) - N(r)] \tag{5.36}$$

together with the standard Kohn-Sham equations self-consistently.

The reader is referred to Ref. [119] for full derivations.

5.5.2 Computational details

We employ the Fritz-Haber-Institute pseudopotentials [120] for all JDFTx calculations. A liquid region of at least 20 Å is used in solid-liquid calculations, with the liquid bulk dielectric constant fixed at $\epsilon = 80$, following Ref. [113].

For each adsorbate i, γ_{i^0} is obtained by surface ionic relaxation within VASP, whereas $\gamma_{i^0,\mathrm{solv}}$, $\gamma_{i^{0/\pm}}$, and $\sigma\phi$ are calculated within JDFTx, all at the JDFTx lattice constants. This is necessary because the oxygen reference chemical potential is obtained from a fit to formation energies of transition metal oxides within VASP [61], and hence the energy comparisons with respect to the adsorbate chemical potentials are only meaningful within VASP.

Adsorbate sites are chosen in a similar fashion as described in Sec. 5.3.2, except protons are initialized on S sites rather than Fe sites, since it is expected that the charge repulsion between the Fe cation and protons is unfavorable.

To obtain electrochemical surface energies, the following procedure is used. (i) Compute lattice constants within JDFTx using Murnaghan equation of state (e.g., a in cubic pyrite) or sequential refinement of volume mesh (e.g., a, b, c in orthorhombic marcasite). Generate pristine surfaces at JDFTx lattice constants. (ii) Perform adsorbed surface ionic relaxation within VASP at JDFTx lattice constants. (iii) Using the relaxed geometry, compute the solid-vacuum system in JDFTx and store the wavefunction and charge density. (iv) Compute neutral solid-liquid system starting from the wavefunction and charge density obtained from the previous step. (v) Compute charged solid-liquid system at constant electron chemical potential.

The accuracy of solid-liquid potential differences has been verified by capturing features in the Gouy-Chapman-Stern model and agreement with experiment in potential of zero charge calculations for various metal slabs [113]. The accuracy of charged-slab computations has been assessed by the excellent agreement in the double-layer capacitance, which is obtained from the slope of surface charge density versus applied voltage, between computation and experiment [113].

5.6 Results

5.6.1 Bulk and pristine surface calculations

JDFT lattice constants are obtained from constant volume computations with relaxation of all internal coordinates (Table 5.2). Compared to experiment, lattice constants are overestimated within JDFTx, unlike the underestimation within VASP, even though the PBE exchange-correlation functional is used in both cases. This is attributed to the different pseudopotentials. Pyrite is the stable phase within JDFTx, in agreement with experiment. However, one should notice that the calculated energy difference of -1.6 meV/FU between the two phases is very small, and that the experimental value has large uncertainty (-43.4 ± 30.7 meV/FU).

Since the structural parameters within JDFTx are sufficiently different from those within VASP, the clean and adsorbed surfaces are created at the JDFTx lattice constants. Despite

Table 5.2: Comparison of lattice constants (in Å), pristine surface energies (in J/m^2), and relative stability (in meV/FU) of pyrite and marcasite between VASP and JDFTx computations.

		VASP	JDFTx	Expt.[a]
Pyrite	a	5.403	5.529	5.416
	$\gamma^{(100)}$	1.04	0.99	
	$\gamma^{(110)}$	1.72	1.68	
	$\gamma^{(111)}$	1.43	1.67	
	$\gamma^{(210)}$	1.48	1.55	
Marcasite	a, b, c	4.438, 5.409, 3.388	4.4508, 5.519, 3.482	4.443, 5.425, 3.387
	$\gamma^{(100)}$	1.72	1.86	
	$\gamma^{(010)}$	1.18	1.13	
	$\gamma^{(001)}$	1.35	1.31	
	$\gamma^{(110)}$	1.31	1.48	
	$\gamma^{(101)}$	0.78	0.85	
	$\gamma^{(011)}$	1.39	1.56	
Relative stability	$g_p - g_m$	21.6	−1.6	-43.4 ± 30.7

[a] Lattice constants are taken from Ref. [4] (pyrite) and Ref. [27] (marcasite). Experimental enthalpies of formation at 298.15 K are taken from Ref. [27].

the discrepancy in lattice constants (within $\sim 2\%$), pristine surface energies obtained from both codes are still in good agreement (within $\sim 10\%$).

5.6.2 Charged surface calculations

For each low-index surface and adsorbate, the four constituent surface energy terms of $\overline{\gamma}$ are listed in Table 5.3. As mentioned in Sec. 5.4.3, the charge carried by each adsorbate is only a fraction $\eta = 0.1$ of its full charge. The first term, except in the cases of H^+-adsorption (due to different adsorption sites, see Sec. 5.5.2), agrees well with the charge-neutral calculation in VASP as presented in Sec. 5.3.3. The second term, the solvation energy of the neutral surface, is always negative since unpaired electrons are screened by the dielectric medium. Its magnitude varies between 30 mJ/m^2 for O^{2-}-adsorbed marcasite (011) to 1.6 J/m^2 for H^+-adsorbed pyrite (110). The third and fourth terms are irrelevant for the neutral H_2O-adsorbed surfaces, but are also unavailable for a few others, namely, the H^+-adsorbed marcasite (001), (110), and (011) surfaces. In these calculations, the surface remains charge-neutral within any reasonable potential difference between the solid and liquid phases.

Furthermore, for H^+-adsorbed pyrite (210), marcasite (100), and (010), as well as O^{2-}-adsorbed marcasite (010), an unusually large magnitude in the surface ionization energy $\gamma_{i^{0/\pm}}$ is found. For instance, at a modest potential of 0.4 V, the maximally-charged case ($\eta = 1$) is attained for H^+-adsorbed pyrite (210). The behavior of these 4 cases are not well-understood and require further investigation. They have been excluded from $\overline{\gamma}$ and the

subsequent surface energy diagrams.

As defined in Eq. (5.26), the electrochemical surface energy $\overline{\gamma}$ is the sum of the 4 energies in Table 5.3. Surface energy diagrams of pyrite and marcasite are plotted in Figs. 5-8 and 5-9, respectively. Unlike the neutral-particle scheme, here we find that H^+ adsorption is energetically favorable on half of the surfaces considered, and that O^{2-} adsorption is almost never favorable [except on pyrite (210) for pH $\gtrsim$ 8 and marcasite (110) for pH $\gtrsim$ 6].

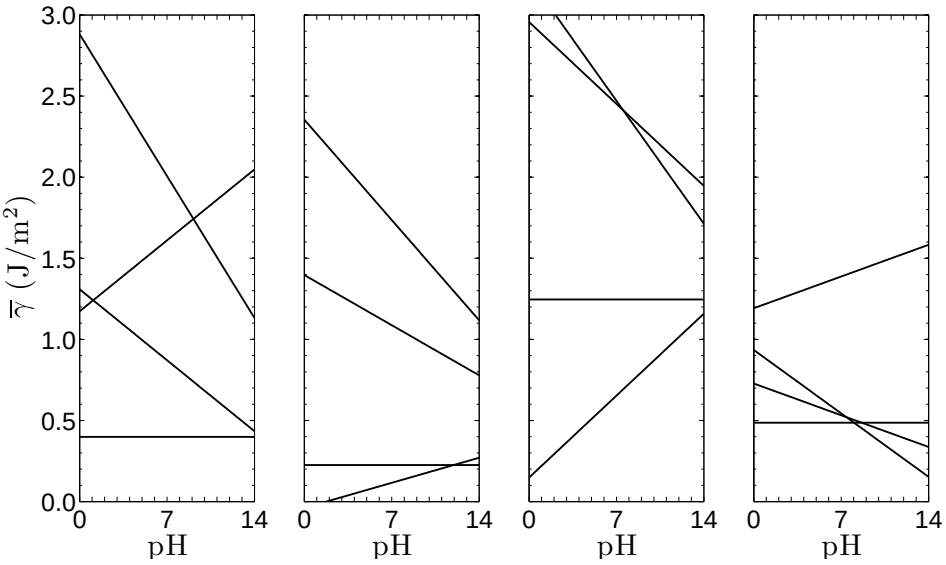

Figure 5-8: Pyrite (100), (110), (111), and (210) surface energy $\overline{\gamma}$ versus pH.

5.7 Discussion

By comparing Figs. 5-8 and 5-9 the phase stability of pyrite and marcasite is predicted. Notice that the surface energy of H^+-adsorbed pyrite (110) becomes negative for pH $\lesssim$ 2. Mathematically, this indicates that the particle would form infinitesimal (110) facets, which physically means that it is unstable. This situation is analogous to point defect formation energy calculations such that a negative formation energy prevents the Fermi level from reaching that position (see Chapter 3), otherwise the bulk host would be completely comprised of such defects. Therefore, for pH $\lesssim$ 2, it is predicted that marcasite is the stable phase.

On the other hand, for pH $\gtrsim$ 2, the pyrite (110) surface energy remains smaller than all marcasite surface energies, which means that pyrite is the stable phase for the entire pH range of 2 to 14. Moreover, since the marcasite surface energy is always higher than pyrite, the relative phase stability is size-*independent*. The implication for the synthesis of marcasite is that, as marcasite grows under acidic conditions, there is no driving force for

Table 5.3: Pyrite and marcasite surface energies (in J/m^2) with adsorbates H^+, H_2O, OH^-, and O^{2-}. Dashes indicate that no data are available. Numbers in brackets require further investigation and are not included in the surface energy diagrams.

Phase	(hkl)	i	$\gamma_{i^0}(\mathrm{pH}=0)$	$\gamma_{i^0,\mathrm{solv}}$	$\gamma_{i^{0/\pm}}$	$\sigma\phi$
Pyrite	(100)	H^+	1.898	−0.772	−0.036	0.083
		H_2O	0.540	−0.141	–	–
		OH^-	1.352	−0.078	−0.037	0.072
		O^{2-}	2.818	−0.082	−0.156	0.302
	(110)	H^+	1.531	−1.573	−0.006	0.009
		H_2O	1.213	−0.988	–	–
		OH^-	1.551	−0.170	−0.017	0.033
		O^{2-}	2.352	−0.077	−0.072	0.152
	(111)	H^+	1.407	−1.259	–	–
		H_2O	1.397	−0.151	–	–
		OH^-	2.996	−0.097	−0.057	0.115
		O^{2-}	3.078	−0.055	−0.226	0.432
	(210)	H^+	2.070	−0.878	(−1.661)	(0.188)
		H_2O	1.341	−0.855	–	–
		OH^-	1.697	−0.974	−0.006	0.011
		O^{2-}	1.930	−1.029	−0.028	0.062
Marcasite	(100)	H^+	1.694	−0.093	(−4.128)	(0.322)
		H_2O	1.204	−0.189	–	–
		OH^-	1.621	−0.183	−0.025	0.050
		O^{2-}	2.620	−0.056	−0.096	0.187
	(010)	H^+	1.618	−0.059	(−4.496)	(0.439)
		H_2O	0.937	−0.229	–	–
		OH^-	1.483	−0.194	−0.034	0.068
		O^{2-}	2.894	−0.056	(1.755)	(0.839)
	(001)	H^+	1.910	−1.292	–	–
		H_2O	1.213	−0.309	–	–
		OH^-	1.623	−0.170	−0.011	0.022
		O^{2-}	2.039	−0.098	−0.043	0.084
	(110)	H^+	1.311	−0.993	–	–
		H_2O	1.230	−0.130	–	–
		OH^-	1.280	−0.156	−0.017	0.034
		O^{2-}	1.277	−0.042	−0.061	0.119
	(101)	H^+	1.919	−0.043	−0.020	0.042
		H_2O	0.552	−0.172	–	–
		OH^-	1.571	−0.202	−0.037	0.074
		O^{2-}	3.110	−0.077	−0.140	0.273
	(011)	H^+	1.330	−0.850	–	–
		H_2O	1.263	−0.132	–	–
		OH^-	2.514	−0.139	−0.045	0.093
		O^{2-}	2.768	−0.031	−0.154	0.298

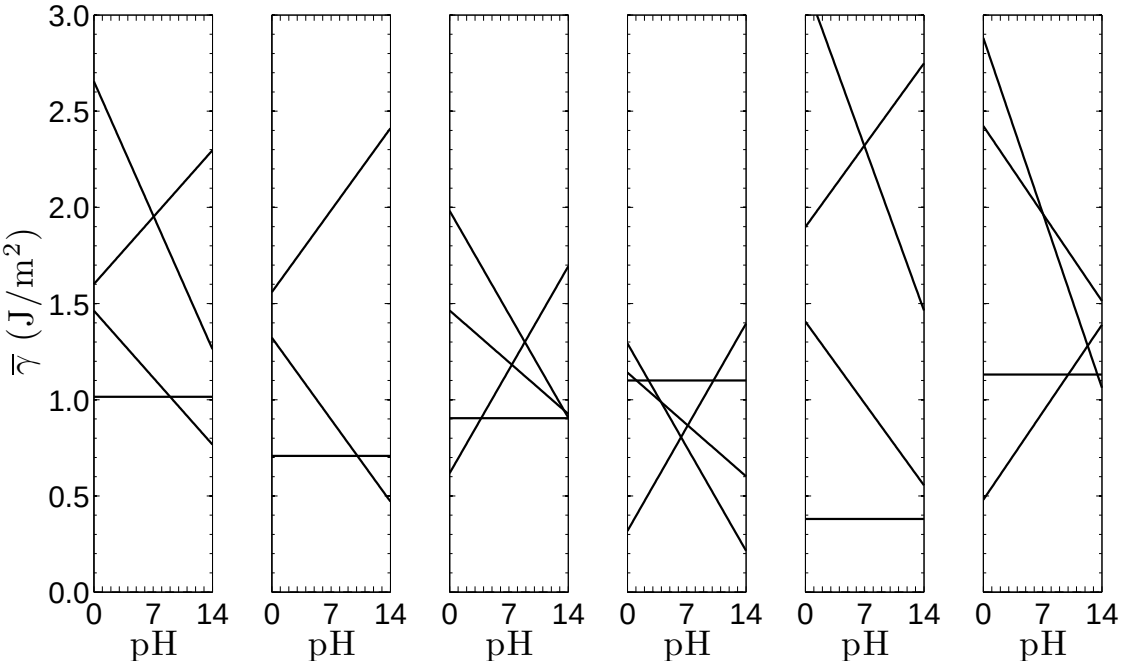

Figure 5-9: Marcasite (100), (010), (001), (110), (101), and (011) surface energy $\overline{\gamma}$ versus pH.

the marcasite-to-pyrite phase transformation to occur, and marcasite remains the thermodynamically stable phase. This may explain the experimental observation of large, well-defined euhedral marcasite crystals synthesized under acidic conditions [11]. The observation of small, anhedral pyrite crystals around the phase-transition pH [11] may be attributed to the low (110) surface energy and possible reactions that may form aggregates of off-stoichiometric surfaces.

Based on the energy contributions in Table 5.3, we see that the first two terms in Eq. (5.26) contribute the most to the electrochemical surface energy, whereas the last two terms partially compensate for each other and have little effect on $\overline{\gamma}$. We have also assumed that any given surface is always fully covered by some adsorbate. The slope of the surface energy line is determined by the coverage and the y-intercept is affected by partial charge fraction η of the species through Ξ. As seen from the pyrite (110) surface energy diagram (Fig. 5-8), the exact point at which $\overline{\gamma}$ crosses 0 is highly sensitive to the slope and intercept of the line, which in the present case determines the phase-transition pH. Therefore, we can only conclude that the pH transition is around 2 (and likely greater than 2 due to the smoothing effect of partial coverage). While the phase-transition pH is, in principle, represented by a single value in our framework, the transition region observed experimentally is not as sharply defined, but ranging from 4 to 6 in Ref. [11] and 2 to 5 in Ref. [10]. Within this range, an increasing percentage of marcasite is formed, together with pyrite, as pH decreases. The issues of partial coverage and partial charge have been recently addressed in the work of Bonnet and Marzari [118], which is also not free of parameters. A more accurate description

of charged surfaces and, hence, the relative stability of polymorphs in aqueous environment may be achieved by the addition of a more rigorous treatment of partial coverage and partial charge into our method presented here.

5.8 Future work

In this section we present some possible continuations of the work to address the limitations and remaining questions. From the computational perspective, the nonlinear fluid response within JDFT has been developed. On the theoretical modeling side, the issues of partial charge transfer and partial coverage still need to be more rigorously investigated.

5.8.1 Nonlinear PCM

Recently, Gunceler *et al.* have shown that the linear PCM overestimates the electrostatic interaction between ionic compounds and liquid water, leading to the development of a nonlinear PCM within JDFT [119]. To illustrate the difference between the linear and nonlinear response, the fluid shape function is drawn in Fig. 5-10 at $s(n) = 1/2$ [i.e., $n = n_c$ in Eq. (5.32)], which represents the transition boundary between the solid and liquid regions. Compared to the nonlinear PCM, the liquid in the linear PCM penetrates deeper into the solid, although it does not overlap with the core of the atomic nucleus. This is caused by a lack of saturation effects in the linear model specifically for ionic compounds, where the local electrostatic potential can be much larger than other materials such as metals and molecules [119]. The solvation energy (Table 5.4) calculated from the nonlinear model can be an order of magnitude smaller than that calculated from the linear model.

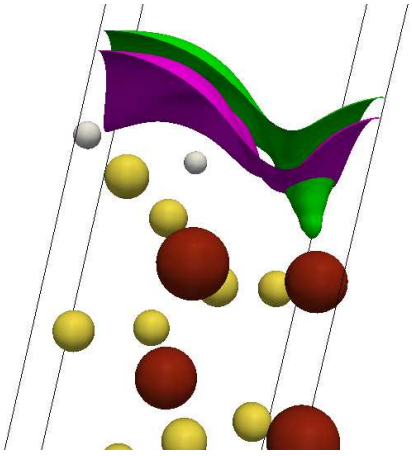

Figure 5-10: Fluid shape at the pyrite (100)/liquid interface. Brown, yellow, and white spheres represent Fe, S, and H atoms, respectively. Isosurfaces are drawn at a liquid density of half the bulk-liquid maximum, within the linear (green) and nonlinear (purple) PCM's.

Table 5.4: Pyrite and marcasite surface solvation energies (in J/m^2) with adsorbates H^+, H_2O, OH^-, and O^{2-} within the linear PCM in Ref. [113], reparametrized linear PCM, and nonlinear PCM in Ref. [119].

Phase	(hkl)	i	$\gamma_{i^0,\text{solv}}$		
			Linear [113]	Linear [119]	Nonlinear [119]
Pyrite	(100)	H^+	−0.772	−0.327	−0.029
		H_2O	−0.141	−0.052	−0.057
		OH^-	−0.078	−0.025	−0.027
		O^{2-}	−0.082	−0.033	−0.034
	(110)	H^+	−1.573	−0.848	−0.085
		H_2O	−0.988	−0.261	−0.123
		OH^-	−0.170	−0.081	−0.082
		O^{2-}	−0.077	−0.022	−0.026
	(111)	H^+	−1.259	−0.027	−0.033
		H_2O	−0.151	−0.070	−0.074
		OH^-	−0.097	−0.043	−0.041
		O^{2-}	−0.055	−0.014	−0.017
	(210)	H^+	−0.878	−0.525	−0.078
		H_2O	−0.855	−0.506	−0.058
		OH^-	−0.974	−0.569	−0.093
		O^{2-}	−1.029	−0.618	−0.063
Marcasite	(100)	H^+	−0.093	−0.031	−0.032
		H_2O	−0.189	−0.075	−0.077
		OH^-	−0.183	−0.092	−0.099
		O^{2-}	−0.056	−0.016	−0.018
	(010)	H^+	−0.059	−0.013	−0.015
		H_2O	−0.229	−0.099	−0.114
		OH^-	−0.194	−0.098	−0.102
		O^{2-}	−0.056	−0.017	−0.017
	(001)	H^+	−1.292	−0.028	−0.034
		H_2O	−0.309	−0.158	−0.164
		OH^-	−0.170	−0.087	−0.084
		O^{2-}	−0.098	−0.031	−0.035
	(110)	H^+	−0.993	−0.462	−0.030
		H_2O	−0.130	−0.042	−0.040
		OH^-	−0.156	−0.076	−0.069
		O^{2-}	−0.042	−0.011	−0.013
	(101)	H^+	−0.043	−0.009	−0.010
		H_2O	−0.172	−0.069	−0.072
		OH^-	−0.202	−0.101	−0.106
		O^{2-}	−0.077	−0.027	−0.028
	(011)	H^+	−0.850	−0.507	−0.039
		H_2O	−0.132	−0.058	−0.060
		OH^-	−0.139	−0.059	−0.063
		O^{2-}	−0.031	−0.001	−0.000

5.8.2 Partial charge transfer and partial coverage

Comparing with experimental surface charge densities reveals that, for instance, full coverage of protons on a surface results in a $\sigma_{\max}$ that is an order of magnitude higher than the measured values. This can be explained by the possibility of (i) coadsorption, where surface charge is partially compensated by adsorption of oppositely-charged species; (ii) partial oxidation or reduction of the host atoms, where in the case of proton adsorption on pyrite an Fe^{2+} ion may become Fe^{3+}; and (iii) partial coverage, where otherwise the electrostatic repulsion of a full coverage of like charges would likely be very energetically unfavorable.

To simplify the complexity, we assume a representative partial charge density, e.g., for proton adsorption,

$$\mathrm{M} + \mathrm{H}^+ + \lambda e^- \to \mathrm{MH}^{(1-\lambda)+}, \tag{5.37}$$

where λ is the electrosorption valency [118]. The reaction energy is

$$\Delta G_{\mathrm{rxn}} = \mu_{\mathrm{MH}^{(1-\lambda)+}} + (1-\lambda)e\phi^s - \mu_{\mathrm{M}} - \left[\mu_{\mathrm{H}}^0 - kT\ln(10)\mathrm{pH} + e\phi^l\right] - \lambda E_F, \tag{5.38}$$

where the electrochemical potential of electrons is the Fermi energy E_F. This gives an electrochemical surface energy of

$$\overline{\gamma}_i(\lambda) = \gamma_{i^0} + \gamma_{i^0,\mathrm{solv}} + \gamma_{i^{0/\pm}} + \sigma\phi - \frac{\lambda(e\phi^l + E_F)}{2S}, \tag{5.39}$$

where $\sigma = (1-\lambda)\sigma_{\max}$. In principle, one can then seek for the λ_0 that minimizes $\overline{\gamma}_i(\lambda)$, which requires that

$$\frac{\partial\overline{\gamma}_i(\lambda)}{\partial\lambda} = \frac{\partial\gamma_{i^{0/\pm}}}{\partial\lambda} + \frac{\partial\sigma\phi}{\partial\lambda} - \frac{e\phi^l}{2S} - \frac{1}{2S}\frac{\partial\lambda E_F}{\partial\lambda} = 0. \tag{5.40}$$

In the case of partial coverage, i.e., $\theta < 1$, the electrochemical surface energy becomes a function of both λ and θ, and we seek a solution for $\mathbf{D}\overline{\gamma}(\lambda,\theta) = \mathbf{0}$ with a positive-definite Hessian $\mathbf{H}\overline{\gamma}$.

5.9 Conclusions

Using a semi-empirical thermodynamics formalism and joint density functional theory computations, we have investigated the relative stability of the FeS_2 polymorphs, pyrite and marcasite, in aqueous environments. The theory of electrochemical surface energy is presented. We find qualitative agreement with experiment that marcasite (pyrite) formation is thermodynamically favorable under acidic (basic) conditions. Within the linear PCM in JDFT, for pH $\lesssim 2$, pyrite becomes unstable because the H^+-adsorbed pyrite (110) surface energy becomes negative; for pH $\gtrsim 2$, pyrite has lower surface energy than marcasite. Therefore, marcasite is predicted to be thermodynamically favorable under highly acidic conditions for all particle sizes. Possible extensions of the theory to partial coverage and partial charge are considered in brief.

Chapter 6

Concluding remarks

The outcome of any serious research can only be to make two questions grow where only one grew before.

Thorstein Veblen

We have studied the photovoltaic and thermodynamic properties of the FeS_2 polymorphs, pyrite and marcasite. In this final chapter, we state the important findings and impact of our work.

As presented in Chapter 2, we have questioned the role of marcasite in the low OCV of pyrite, based on our calculations that the band gap of marcasite is not smaller than that of pyrite [121]. To date, although the band gap of marcasite has not been directly verified from experiment, Seefeld *et al.* are able to synthesize mixed-phase pyrite/marcasite samples with 50 vol. % marcasite [122]. Compared to phase-pure pyrite samples, the presence of such a significant amount of marcasite gives very similar absorption coefficient and band gap, suggesting that the marcasite band gap is at least as big as the pyrite band gap, which confirms our theoretical predictions. To explain the low OCV of pyrite, surface off-stoichiometry [123, 124] and defects caused by marcasite [122] have been proposed, and we await further experimental evidence.

To explain the ubiquitous p-type conductivity of pyrite, we have proposed in Chapter 3 a mechanism involving oxygen-on-sulfur substitution [125]. Recent experiments once again produce p-type thin films with high impurity levels of oxygen [$O(10^{19})$ cm^{-3}], but among many other contaminants [126], and thus the effect of a single defect cannot be determined. Nonetheless, following the defect energy calculations of Yu *et al.* [123] and our own results [125], it has become clearer that pyrite FeS_2 is indeed a line compound, and that the observation of off-stoichiometric samples should be attributed to the presence of S-deficient phases instead of S vacancies [123].

In Chapter 4, we have found that, unfortunately, the band gap of pyrite cannot be effectively tuned via cation doping due to large electronegativity or size mismatch [127]. The candidate Zn is further studied by Hu *et al.* computationally, where although a modest 0.1-

eV band gap increase can be achieved with 6% doping, its incorporation is not energetically favorable [128]. The authors also claim that oxygen doping can enhance the band gap and absorptivity of pyrite. However, the hypothetical compound is not phase stable, and whether oxygen inclusion is desirable for transport properties remains questionable.

We remark that the highest efficiency pyrite solar cell ever made is a photoelectrochemical device [5]. The performance of such a device depends not only on the bulk properties of the photovoltaic material, but also on the band alignment of the material with the specific redox couple that is present in the aqueous region. It may be possible that, while the iodide/triiodide redox couple is the most optimal for pyrite [5], the band alignment at the pyrite/solution interface may simply be non-ideal to obtain a larger OCV than the current record of 0.2 V. Given that pyrite can be readily doped *n*- and *p*-type, future research direction should move toward making solid-state *p*-*n* junctions (either pyrite homojunction or, due to the low hole mobility, heterojunction) and improving sample qualities.

Finally, in Chapter 5, we have presented a framework for computing charged surface energies within joint density functional theory to predict polymorph stability in aqueous environment, using the FeS_2 polymorphs, pyrite and marcasite, as a model system. Our results are in relatively good agreement with experimental observations such that the metastable marcasite phase becomes the ground state in acidic conditions. To obtain a more accurate description and understanding of the electrochemical interface and energetics, one will need to investigate the possible effects of coadsorption, partial coverage of adsorbates, partial charge transfer, and adsorbates other than H^+, H_2O, OH^-, and O^{2-} that may play a role in surface reactions leading to off-stoichiometric surfaces. (See Sec. 5.8 for a brief discussion.) The effect of electrode potential can be readily incorporated, and, using empirical solvation energies for ions (as demonstrated in Refs. [110,111]), Pourbaix diagrams can be constructed for all inorganic crystalline materials, which will allow for an unprecedented prediction of phase stability as a function of particle size, pH, and electrode potential.

Bibliography

[1] W. Shockley and H.J. Queisser. Detailed balance limit of efficiency of p-n junction solar cells. *J. Appl. Phys.*, 32:510, 1961.

[2] J. Nelson. *The Physics of Solar Cells*. Imperial College Press, London, 2003.

[3] Martin A. Green. Third generation photovoltaics: Ultra-high conversion efficiency at low cost. *Progress in Photovoltaics: Research and Applications*, 9(2):123–135, 2001.

[4] Riley Murphy and Daniel R. Strongin. Surface reactivity of pyrite and related sulfides. *Surf. Sci. Rep.*, 64(1):1 – 45, 2009.

[5] A. Ennaoui, S. Fiechter, Ch. Pettenkofer, N. Alonso-Vante, K. Büker, M. Bronold, Ch. Höpfner, and H. Tributsch. Iron disulfide for solar energy conversion. *Sol. Energy Mater. Sol. Cells*, 29(4):289 – 370, 1993.

[6] I.J. Ferrer, D.M. Nevskaia, C. de las Heras, and C. Sanchez. About the band gap nature of FeS_2 as determined from optical and photoelectrochemical measurements. *Solid State Commun.*, 74(9):913 – 916, 1990.

[7] Cyrus Wadia, A. Paul Alivisatos, and Daniel M. Kammen. Materials availability expands the opportunity for large-scale photovoltaics deployment. *Environ. Sci. Technol.*, 43(6):2072–2077, 2009.

[8] M.R. Ranade, A. Navrotsky, H.Z. Zhang, J.F. Banfield, S.H. Elder, A. Zaban, P.H. Borse, S.K. Kulkarni, G.S. Doran, and H.J. Whitfield. Energetics of nanocrystalline TiO_2. *P. Natl. Acad. Sci. USA*, 99(2):6476–6481, 2002.

[9] E.T. Allen, J.L. Crenshaw, and H.E. Merwin. The sulphides of zinc, cadmium, and mercury; their crystalline forms and genetic conditions. *Amer. J. Sci.*, (202):341–396, 1912.

[10] James B. Murowchick and H.L. Barnes. Marcasite precipitation from hydrothermal solutions. *Geochim. Cosmochim. Ac.*, 50(12):2615 – 2629, 1986.

[11] M.A.A. Schoonen and H.L. Barnes. Reactions forming pyrite and marcasite from solution: II. Via FeS precursors below 100°C. *Geochim. Cosmochim. Ac.*, 55(6):1505 – 1514, 1991.

[12] M. Bronold, Y. Tomm, and W. Jaegermann. Surface states on cubic d-band semiconductor pyrite (FeS_2). *Surf. Sci.*, 314(3):L931 – L936, 1994.

[13] M. Bronold, K. Büker, S. Kubala, C. Pettenkofer, and H. Tributsch. Surface Preparation of FeS_2 via electrochemical etching and interface formation with metals. *Phys. Status Solidi A*, 135(1):231–243, 1993.

[14] Qiu Guanzhou, Xiao Qi, and Hu Yuehua. First-principles calculation of the electronic structure of the stoichiometric pyrite FeS_2(100) surface (No. 03-11). *Comput. Mater. Sci.*, 29(1):89 – 94, 2004.

[15] Jun Cai and Michael R. Philpott. Electronic structure of bulk and (001) surface layers of pyrite FeS_2. *Comput. Mater. Sci.*, 30(3-4):358 – 363, 2004.

[16] Cyrus Wadia, Yue Wu, Sheraz Gul, Steven K. Volkman, Jinghua Guo, and A. Paul Alivisatos. Surfactant-assisted hydrothermal synthesis of single phase pyrite FeS_2 nanocrystals. *Chem. Mater.*, 21(13):2568–2570, 2009.

[17] D. Spagnoli, K. Refson, K. Wright, and J. D. Gale. Density functional theory study of the relative stability of the iron disulfide polymorphs pyrite and marcasite. *Phys. Rev. B*, 81(9):094106, Mar 2010.

[18] M. Birkholz, S. Fiechter, A. Hartmann, and H. Tributsch. Sulfur deficiency in iron pyrite (FeS_{2-x}) and its consequences for band-structure models. *Phys. Rev. B*, 43(14):11926–11936, May 1991.

[19] M. Bronold, C. Pettenkofer, and W. Jaegermann. Surface photovoltage measurements on pyrite (100) cleavage planes: Evidence for electronic bulk defects. *J. Appl. Phys.*, 76(10):5800–5808, 1994.

[20] G. U. von Oertzen, W. M. Skinner, and H. W. Nesbitt. Ab initio and x-ray photoemission spectroscopy study of the bulk and surface electronic structure of pyrite (100) with implications for reactivity. *Phys. Rev. B*, 72(23):235427, Dec 2005.

[21] AM Abd El Halim, S. Fiechter, and H. Tributsch. Control of interfacial barriers in n-type FeS_2 (pyrite) by electrodepositing metals (Co, Cu) forming isostructural disulfides. *Electrochim. Acta*, 47(16):2615–2623, 2002.

[22] J. Oertel, K. Ellmer, W. Bohne, J. Röhrich, and H. Tributsch. Growth of n-type polycrystalline pyrite (FeS_2) films by metalorganic chemical vapour deposition and their electrical characterization. *J. Cryst. Growth*, 198-199(Part 2):1205 – 1210, 1999.

[23] S.L. Harmer and H.W. Nesbitt. Stabilization of pyrite (FeS_2), marcasite (FeS_2), arsenopyrite (FeAsS) and loellingite ($FeAs_2$) surfaces by polymerization and auto-redox reactions. *Surf. Sci.*, 564(1-3):38 – 52, 2004.

[24] Koichi Momma and Fujio Izumi. *VESTA*: a three-dimensional visualization system for electronic and structural analysis. *J. Appl. Crystallogr.*, 41(3):653–658, Jun 2008.

[25] R. Krishnamurthy and W.B. Schaap. Computing ligand field potentials and relative energies of d orbitals: Theory. *J. Chem. Educ.*, 47(6):433, 1970.

[26] F. Hulliger and E. Mooser. Semiconductivity in pyrite, marcasite and arsenopyrite phases. *J. Phys. Chem. Solids*, 26(2):429–433, 1965.

[27] F. Grønvold and E.F. Westrum Jr. Heat capacities of iron disulfides thermodynamics of marcasite from 5 to 700 K, pyrite from 300 to 780 K, and the transformation of marcasite to pyrite. *J. Chem. Thermodyn.*, 8(11):1039–1048, 1976.

[28] B. Hyde and M. O'Keeffe. Marcasite and pyrite (FeS_2). *Aust. J. Chem.*, 49(8):867–872, 1996.

[29] M. E. Fleet. Structural aspects of the marcasite-pyrite transformation. *Can. Mineral.*, 10(2):225, 1970.

[30] K.J. Brock and L.D. Slater. Epitaxial marcasite on pyrite from Rensselaer, Indiana. *Am. Mineral.*, 63(1-2):210, 1978.

[31] D. M. Schleich and H. S. W. Chang. Iron pyrite and iron marcasite thin films prepared by low pressure chemical vapor deposition. *J. Cryst. Growth*, 112(4):737–744, 1991.

[32] B. Thomas, T. Cibik, C. Höpfner, K. Diesner, G. Ehlers, S. Fiechter, and K. Ellmer. Formation of secondary iron-sulphur phases during the growth of polycrystalline iron pyrite (FeS_2) thin films by MOCVD. *J. Mater. Sci.-Mater. El.*, 9:61–64, 1998.

[33] W. Folkerts, G. A. Sawatzky, C. Haas, R. A. Groot, and F. U. Hillebrecht. Electronic structure of some 3d transition-metal pyrites. *J. Phys. C Solid State*, 20:4135, 1987.

[34] M. S. Jagadeesh and M. S. Seehra. Electrical resistivity and band gap of marcasite (FeS_2). *Phys. Lett. A*, 80(1):59–61, 1980.

[35] D. W. Bullett. Electronic structure of 3d pyrite-and marcasite-type sulphides. *J. Phys. C*, 15:6163, 1982.

[36] P. Hohenberg and W. Kohn. Inhomogeneous electron gas. *Phys. Rev.*, 136(3B):B864–B871, Nov 1964.

[37] W. Kohn and L. J. Sham. Self-consistent equations including exchange and correlation effects. *Phys. Rev.*, 140(4A):A1133–A1138, Nov 1965.

[38] P. E. Blöchl. Projector augmented-wave method. *Phys. Rev. B*, 50:17953, 1994.

[39] G. Kresse and D. Joubert. From ultrasoft pseudopotentials to the projector augmented-wave method. *Phys. Rev. B*, 59:1758, 1999.

[40] G. Kresse and J. Hafner. Ab initio molecular dynamics for liquid metals. *Phys. Rev. B*, 47:558, 1993.

[41] G. Kresse and J. Hafner. Ab initio molecular-dynamics simulation of the liquid-metal-amorphous-semiconductor transition in germanium. *Phys. Rev. B*, 49:14251, 1994.

[42] G. Kresse and J. Furthmüller. Efficient iterative schemes for ab initio total-energy calculations using a plane-wave basis set. *Phys. Rev. B*, 54(16):11169–11186, Oct 1996.

[43] G. Kresse and J. Furthmüller. Efficiency of ab-initio total energy calculations for metals and semiconductors using a plane-wave basis set. *Comput. Mater. Sci.*, 6(1):15 – 50, 1996.

[44] J. P. Perdew and Alex Zunger. Self-interaction correction to density-functional approximations for many-electron systems. *Phys. Rev. B*, 23(10):5048–5079, May 1981.

[45] J. P. Perdew, K. Burke, and M. Ernzerhof. Generalized gradient approximation made simple. *Phys. Rev. Lett.*, 77:3865, 1996.

[46] J. P. Perdew, K. Burke, and M. Ernzerhof. Erratum: Generalized gradient approximation made simple. *Phys. Rev. Lett.*, 78:1396, 1997.

[47] R. Armiento and A. E. Mattsson. Functional designed to include surface effects in self-consistent density functional theory. *Phys. Rev. B*, 72(8):085108, Aug 2005.

[48] Ann E. Mattsson and Rickard Armiento. Implementing and testing the AM05 spin density functional. *Phys. Rev. B*, 79(15):155101, Apr 2009.

[49] U von Barth and L Hedin. A local exchange-correlation potential for the spin polarized case: I. *J. Phys. C*, 5(13):1629, 1972.

[50] M.M Pant and A.K. Rajagopal. Theory of inhomogeneous magnetic electron gas. *Solid State Commun.*, 10(12):1157 – 1160, 1972.

[51] A. I. Liechtenstein, V. I. Anisimov, and J. Zaanen. Density-functional theory and strong interactions: Orbital ordering in mott-hubbard insulators. *Phys. Rev. B*, 52(8):R5467–R5470, Aug 1995.

[52] Kristin Persson, Gerbrand Ceder, and Dane Morgan. Spin transitions in the $Fe_xMn_{1-x}S_2$ system. *Phys. Rev. B*, 73(11):115201, Mar 2006.

[53] Hendrik J. Monkhorst and James D. Pack. Special points for brillouin-zone integrations. *Phys. Rev. B*, 13(12):5188–5192, Jun 1976.

[54] P. W. Tasker. The stability of ionic crystal surfaces. *J. Phys. C: Solid State Phys*, 12(22):4977–84, 1979.

[55] V. Fiorentini and M. Methfessel. Extracting convergent surface energies from slab calculations. *J. Phys.: Condens. Matter*, 8:6525, 1996.

[56] Andrew Hung, Joseph Muscat, Irene Yarovsky, and Salvy P. Russo. Density-functional theory studies of pyrite FeS_2(100) and (110) surfaces. *Surface Science*, 513(3):511 – 524, 2002.

[57] Andrew Hung, Joseph Muscat, Irene Yarovsky, and Salvy P. Russo. Density-functional theory studies of pyrite FeS_2(111) and (210) surfaces. *Surface Science*, 520(1-2):111 – 119, 2002.

[58] D.R. Alfonso. Computational Investigation of FeS_2 Surfaces and Prediction of Effects of Sulfur Environment on Stabilities. *The Journal of Physical Chemistry C*, 114(19):8971–8980, 2010.

[59] V. Eyert, K.-H. Höck, S. Fiechter, and H. Tributsch. Electronic structure of FeS_2: The crucial role of electron-lattice interaction. *Phys. Rev. B*, 57(11):6350–6359, Mar 1998.

[60] Heather J. Kulik, Matteo Cococcioni, Damian A. Scherlis, and Nicola Marzari. Density functional theory in transition-metal chemistry: A self-consistent Hubbard U approach. *Phys. Rev. Lett.*, 97(10):103001, Sep 2006.

[61] Lei Wang, Thomas Maxisch, and Gerbrand Ceder. Oxidation energies of transition metal oxides within the GGA+U framework. *Phys. Rev. B*, 73(19):195107, May 2006.

[62] G. Willeke, R. Dasbach, B. Sailer, and E. Bucher. Thin pyrite (FeS_2) films prepared by magnetron sputtering. *Thin Solid Films*, 213(2):271 – 276, 1992.

[63] Jochen Heyd, Gustavo E. Scuseria, and Matthias Ernzerhof. Hybrid functionals based on a screened coulomb potential. *J. Chem. Phys.*, 118(18):8207–8215, 2003.

[64] Jochen Heyd, Gustavo E. Scuseria, and Matthias Ernzerhof. Erratum: "Hybrid functionals based on a screened Coulomb potential" [J. Chem. Phys. 118, 8207 (2003)]. *J. Chem. Phys.*, 124(21):219906, 2006.

[65] J. Paier, M. Marsman, K. Hummer, G. Kresse, I. C. Gerber, and J. G. Angyan. Screened hybrid density functionals applied to solids. *J. Chem. Phys.*, 124(15):154709, 2006.

[66] J. Paier, M. Marsman, K. Hummer, G. Kresse, I. C. Gerber, and J. G. Angyan. Erratum: "Screened hybrid density functionals applied to solids" [J. Chem. Phys. 124, 154709 (2006)]. *J. Chem. Phys.*, 125(24):249901, 2006.

[67] M. K. Y. Chan and G. Ceder. Efficient band gap prediction for solids. *Phys. Rev. Lett.*, 105(19):196403, Nov 2010.

[68] V. I. Anisimov, F. Aryasetiawan, and A. I. Lichtenstein. First-principles calculations of the electronic structure and spectra of strongly correlated systems: the lda + u method. *J. Phys.: Condens. Matter*, 9(4):767, 1997.

[69] Y. Sun, S. E. Thompson, and T. Nishida. Physics of strain effects in semiconductors and metal-oxide-semiconductor field-effect transistors. *J. Appl. Phys.*, 101(10):104503, 2007.

[70] W. Jaegermann and H. Tributsch. Photoelectrochemical reactions of FeS_2 (pyrite) with H_2O and reducing agents. *J. Appl. Electrochem.*, 13(6):743–750, 1983.

[71] K. Ellmer and C. Höpfner. On the stoichiometry of the semiconductor pyrite (FeS_2). *Phil. Mag. A*, 75(4):1129–1152, 1997.

[72] S. Bausch, B. Sailer, H. Keppner, G. Willeke, E. Bucher, and G. Frommeyer. Preparation of pyrite films by plasma-assisted sulfurization of thin iron films. *Appl. Phys. Lett.*, 57(1):25–27, 1990.

[73] G. Smestad, A. Ennaoui, S. Fiechter, H. Tributsch, W. K. Hofmann, M. Birkholz, and W. Kautek. Photoactive thin film semiconducting iron pyrite prepared by sulfurization of iron oxides. *Sol. Energy Mater.*, 20(3):149–165, 1990.

[74] Sokrates T. Pantelides. The electronic structure of impurities and other point defects in semiconductors. *Rev. Mod. Phys.*, 50(4):797–858, Oct 1978.

[75] András Stirling, Marco Bernasconi, and Michele Parrinello. Defective pyrite (100) surface: An ab initio study. *Phys. Rev. B*, 75(16):165406, Apr 2007.

[76] K. Andersson, M. Nyberg, H. Ogasawara, D. Nordlund, T. Kendelewicz, C. S. Doyle, G. E. Brown, L. G. M. Pettersson, and A. Nilsson. Experimental and theoretical characterization of the structure of defects at the pyrite FeS_2(100) surface. *Phys. Rev. B*, 70(19):195404, Nov 2004.

[77] Clas Persson, Yu-Jun Zhao, Stephan Lany, and Alex Zunger. n-type doping of $CuInSe_2$ and $CuGaSe_2$. *Phys. Rev. B*, 72(3):035211, Jul 2005.

[78] Chris G. Van de Walle and Jorg Neugebauer. First-principles calculations for defects and impurities: Applications to III-nitrides. *J. Appl. Phys.*, 95(8):3851–3879, 2004.

[79] G. Makov and M. C. Payne. Periodic boundary conditions in ab initio calculations. *Phys. Rev. B*, 51(7):4014–4022, Feb 1995.

[80] M. Gajdoš, K. Hummer, G. Kresse, J. Furthmüller, and F. Bechstedt. Linear optical properties in the projector-augmented wave methodology. *Phys. Rev. B*, 73(4):045112, Jan 2006.

[81] Stephan Lany and Alex Zunger. Assessment of correction methods for the band-gap problem and for finite-size effects in supercell defect calculations: Case studies for zno and gaas. *Phys. Rev. B*, 78(23):235104, Dec 2008.

[82] P. Torres, J. Meier, R. Fluckiger, U. Kroll, J. A. Anna Selvan, H. Keppner, A. Shah, S. D. Littelwood, I. E. Kelly, and P. Giannoules. Device grade microcrystalline silicon owing to reduced oxygen contamination. *Appl. Phys. Lett.*, 69(10):1373–1375, 1996.

[83] J. C. Phillips and J. A. Van Vechten. Macroscopic model of formation of vacancies in semiconductors. *Phys. Rev. Lett.*, 30(6):220–223, Feb 1973.

[84] Chris G. Van de Walle. DX-center formation in wurtzite and zinc-blende $Al_xGa_{1-x}N$. *Phys. Rev. B*, 57(4):R2033–R2036, Jan 1998.

[85] SW Lehner, KS Savage, and JC Ayers. Vapor growth and characterization of pyrite (FeS_2) doped with Co, Ni, and As: Variations in semiconducting properties. *J. Cryst. Growth*, 286(2):306–317, 2006.

[86] O. Blenk, E. Bucher, and G. Willeke. p-type conduction in pyrite single crystals prepared by chemical vapor transport. *Appl. Phys. Lett.*, 62(17):2093–2095, 1993.

[87] Su-Huai Wei and Alex Zunger. Band offsets and optical bowings of chalcopyrites and Zn-based II-VI alloys. *J. Appl. Phys.*, 78(6):3846–3856, 1995.

[88] I. Vurgaftman, J. R. Meyer, and L. R. Ram-Mohan. Band parameters for III-V compound semiconductors and their alloys. *J. Appl. Phys.*, 89(11):5815–5875, 2001.

[89] Pietro P. Altermatt, Tobias Kiesewetter, Klaus Ellmer, and Helmut Tributsch. Specifying targets of future research in photovoltaic devices containing pyrite (FeS_2) by numerical modelling. *Sol. Energy Mater. Sol. Cells*, 71(2):181 – 195, 2002.

[90] A. Fujimori, K. Mamiya, T. Mizokawa, T. Miyadai, T. Sekiguchi, H. Takahashi, N. Môri, and S. Suga. Resonant photoemission study of pyrite-type NiS_2, CoS_2 and FeS_2. *Phys. Rev. B*, 54:16329–16332, Dec 1996.

[91] R. J. Bouchard. The preparation of pyrite solid solutions of the type $Fe_xCo_{1-x}S_2$, $Co_xNi_{1-x}S_2$, and $Cu_xNi_{1-x}S_2$. *Mater. Res. Bull.*, 3(7):563 – 570, 1968.

[92] T. A. Bither, P. C. Donohue, W. H. Cloud, P. E. Bierstedt, and H. S. Young. Mixed-cation transition metal pyrite dichalcogenides—High pressure synthesis and properties. *J. Solid State Chem.*, 1(3-4):526 – 533, 1970.

[93] F. D. Murnaghan. The compressibility of media under extreme pressures. *P. Natl. Acad. Sci. USA*, 30(9):244, 1944.

[94] I. P. Ipatova, V. G. Malyshkin, and V. A. Shchukin. On spinodal decomposition in elastically anisotropic epitaxial films of III-V semiconductor alloys. *J. Appl. Phys.*, 74(12):7198–7210, 1993.

[95] M. J. Mehl. Pressure dependence of the elastic moduli in aluminum-rich Al-Li compounds. *Phys. Rev. B*, 47(5):2493–2500, Feb 1993.

[96] H. D. Lutz, B. Muller, T. Schmidt, and T. Stingl. Structure refinement of pyrite-type ruthenium disulfide, RuS_2, and ruthenium diselenide, $RuSe_2$. *Acta Crystallogr. C*, 46(11):2003–2005, 1990.

[97] T. Stingl, B. Mueller, and HD Lutz. Crystal structure refinement of osmium (II) disulfide, OsS_2. *Z. Kristallogr.*, 202(1-2):161–162, 1992.

[98] R. D. Shannon. Revised effective ionic radii and systematic studies of interatomic distances in halides and chalcogenides. *Acta Crystallogr. A*, 32(5):751–767, Sep 1976.

[99] A. L. Allred. Electronegativity values from thermochemical data. *J. Inorg. Nucl. Chem.*, 17(3-4):215 – 221, 1961.

[100] Shiyou Chen, X. G. Gong, and Su-Huai Wei. Band-structure anomalies of the chalcopyrite semiconductors $CuGaX_2$ versus $AgGaX_2$ (X = S and Se) and their alloys. *Phys. Rev. B*, 75:205209, May 2007.

[101] Alex Zunger, S.-H. Wei, L. G. Ferreira, and James E. Bernard. Special quasirandom structures. *Phys. Rev. Lett.*, 65:353–356, Jul 1990.

[102] Johann von Pezold, Alexey Dick, Martin Friák, and Jörg Neugebauer. Generation and performance of special quasirandom structures for studying the elastic properties of random alloys: Application to Al-Ti. *Phys. Rev. B*, 81:094203, Mar 2010.

[103] A. van de Walle, M. Asta, and G. Ceder. The alloy theoretic automated toolkit: A user guide. *Calphad*, 26(4):539 – 553, 2002.

[104] Takashi Harada. Transport Properties of Iron Dichalcogenides FeX_2 (X=S, Se and Te). *J. Phys. Soc. Jpn.*, 67(4):1352–1358, 1998.

[105] Han Kwon, S. Thanikaikarasan, Thaiyan Mahalingam, Kyung Park, C. Sanjeeviraja, and Yong Kim. Characterization of electrosynthesized iron diselenide thin films. *J. Mater. Sci.-Mater. El.*, 19:1086–1091, 2008.

[106] G. Ceder, G. D. Garbulsky, and P. D. Tepesch. Convergent real-space cluster expansion for configurational disorder in ionic systems. *Phys. Rev. B*, 51:11257–11261, May 1995.

[107] Meng-Ju Sher, Mark T. Winkler, and Eric Mazur. Pulsed-laser hyperdoping and surface texturing for photovoltaics. *MRS Bull.*, 36(06):439–445, 2011.

[108] Michael P. Finnegan, Hengzhong Zhang, and Jillian F. Banfield. Phase stability and transformation in titania nanoparticles in aqueous solutions dominated by surface energy. *J. Phys. Chem. C*, 111(5):1962–1968, 2007.

[109] A. S. Barnard and L. A. Curtiss. Prediction of TiO_2 nanoparticle phase and shape transitions controlled by surface chemistry. *Nano Letters*, 5(7):1261–1266, 2005.

[110] L. Wang. *First-principles modeling of thermal stability and morphology control of cathode materials in Li-ion batteries*. PhD thesis, Massachusetts Institute of Technology, Feb 2010.

[111] Kristin A. Persson, Bryn Waldwick, Predrag Lazic, and Gerbrand Ceder. Prediction of solid-aqueous equilibria: Scheme to combine first-principles calculations of solids with experimental aqueous states. *Phys. Rev. B*, 85:235438, Jun 2012.

[112] S. A. Petrosyan, A. A. Rigos, and T. A. Arias. Joint density-functional theory: Ab initio study of Cr_2O_3 surface chemistry in solution. *J. Phys. Chem. B*, 109(32):15436–15444, 2005.

[113] Kendra Letchworth-Weaver and T. A. Arias. Joint density functional theory of the electrode-electrolyte interface: Application to fixed electrode potentials, interfacial capacitances, and potentials of zero charge. *Phys. Rev. B*, 86:075140, Aug 2012.

[114] T. A. Arias, M. C. Payne, and J. D. Joannopoulos. *Ab initio* molecular dynamics: Analytically continued energy functionals and insights into iterative solutions. *Phys. Rev. Lett.*, 69:1077–1080, Aug 1992.

[115] Sohrab Ismail-Beigi and T.A. Arias. New algebraic formulation of density functional calculation. *Comput. Phys. Comm.*, 128(1-2):1 – 45, 2000.

[116] R. Sundararaman, K. Letchworth-Weaver, and T.A. Arias. JDFTx, available from http://jdftx.sourceforge.net, 2012.

[117] A.J. Bard and L.R. Faulkner. *Electrochemical Methods: Fundamentals and Applications*. John Wiley & Sons, New Jersey, second edition, 2001.

[118] Nicéphore Bonnet and Nicola Marzari. First-principles prediction of the equilibrium shape of nanoparticles under realistic electrochemical conditions. *Phys. Rev. Lett.*, 110:086104, Feb 2013.

[119] Deniz Gunceler, Kendra Letchworth-Weaver, Ravishankar Sundararaman, Kathleen A Schwarz, and TA Arias. The importance of nonlinear fluid response in joint density-functional theory studies of battery systems. *arXiv preprint arXiv:1301.6189*, 2013.

[120] Martin Fuchs and Matthias Scheffler. Ab initio pseudopotentials for electronic structure calculations of poly-atomic systems using density-functional theory. *Comput. Phys. Commun.*, 119(1):67 – 98, 1999.

[121] Ruoshi Sun, M. K. Y. Chan, and G. Ceder. First-principles electronic structure and relative stability of pyrite and marcasite: Implications for photovoltaic performance. *Phys. Rev. B*, 83:235311, Jun 2011.

[122] Sean Seefeld, Moritz Limpinsel, Yu Liu, Nima Farhi, Amanda Weber, Yanning Zhang, Nicholas Berry, Yon Joo Kwon, Craig L. Perkins, John C. Hemminger, Ruqian Wu, and Matt Law. Iron pyrite thin films synthesized from an $Fe(acac)_3$ ink. *J. Amer. Chem. Soc.*, 135(11):4412–4424, 2013.

[123] Liping Yu, Stephan Lany, Robert Kykyneshi, Vorranutch Jieratum, Ram Ravichandran, Brian Pelatt, Emmeline Altschul, Heather A. S. Platt, John F. Wager, Douglas A. Keszler, and Alex Zunger. Iron chalcogenide photovoltaic absorbers. *Adv. Energy Mater.*, 1(5):748–753, 2011.

[124] Y. N. Zhang, J. Hu, M. Law, and R. Q. Wu. Effect of surface stoichiometry on the band gap of the pyrite $FeS_2(100)$ surface. *Phys. Rev. B*, 85:085314, Feb 2012.

[125] Ruoshi Sun, M. K. Y. Chan, S. Y. Kang, and G. Ceder. Intrinsic stoichiometry and oxygen-induced *p*-type conductivity of pyrite FeS_2. *Phys. Rev. B*, 84:035212, Jul 2011.

[126] Nicholas Berry, Ming Cheng, Craig L. Perkins, Moritz Limpinsel, John C. Hemminger, and Matt Law. Atmospheric-pressure chemical vapor deposition of iron pyrite thin films. *Adv. Energy Mater.*, 2(9):1124–1135, 2012.

[127] Ruoshi Sun and Gerbrand Ceder. Feasibility of band gap engineering of pyrite FeS_2. *Phys. Rev. B*, 84:245211, Dec 2011.

[128] Jun Hu, Yanning Zhang, Matt Law, and Ruqian Wu. Increasing the band gap of iron pyrite by alloying with oxygen. *J. Amer. Chem. Soc.*, 134(32):13216–13219, 2012.

Epilogue

On August 27, 2012, our group went for a boat ride. Netted trampolines were extended beyond the boat. I sat at the very front.

"You're gonna get wet," my advisor warned. He was right, as usual. I spent the rest of the day drying myself.

But that was what made the trip memorable to me.